論文の内容の要旨

Suppression of Decoherence in Open Quantum Systems: Resonance and Topological Effects

(開放量子系におけるデコヒーレンスの抑制: 共鳴とトポロジカル効果)

尚　程

In experiments, quantum objects are inevitably open systems influenced by their surrounding environment. Contemporary physics has significantly emphasized the shift from closed to open systems in integrating quantum theory into real-world applications. However, the introduction of the environment causes quantum systems to be affected by quantum noise and dissipation, leading to decoherence. Protecting quantum systems from decoherence is crucial in open quantum systems. In this thesis, we investigate how resonance and topological effects can be utilized to suppress decoherence in open quantum systems. We focus on tackling two key challenges in advancing quantum information processing: protecting continuous-variable entanglement and reducing energy loss in photon transmission.

With the aid of quantum resources, quantum systems often investigate potential advantages in information processing compared to their classical counterparts. Entanglement is a crucial resource in quantum information processing. Unfortunately, it is fragile due to decoherence. First, motivated by entanglement protection, we propose a resonant filtering mechanism to protect optomechanical entanglement. We demonstrate that our filtering model enhances

the robustness of the stationary maximum optomechanical entanglement to thermal fluctuation noise and mechanical damping.

On the other hand, long-distance transmission of photons is essential for building large-scale quantum networks. However, photons typically disperse throughout the photonic waveguide and are depleted due to environment-induced decoherence. Second, inspired by the development of topological waveguides, we demonstrate how to utilize topological waveguides to achieve near-perfect photon transfer in the topologically nontrivial phase. We also find that when two-level systems are coupled at the same sublattice within a unit cell, the ergotropy becomes immune to dissipation at that location, facilitated by a dark state and a topologically robust dressed bound state. The results of this Thesis are highly relevant to the development of state-of-the-art miniaturized devices and serve as fundamental paradigms for further studies on decoherence suppression in open quantum systems.

In Chapter 2, motivated by the imperative need for optomechanical entanglement protection in open quantum systems, our study delves into using resonance effects to protect thermal entanglement between photon and phonon. The essential innovation lies in our proposed filtering model, designed to selectively filter significant detuning components between a thermal-mechanical mode and its surrounding heat baths, thereby resilience against decoherence.

Our study emphasizes the crucial role of protecting continuous-variable entanglement by filtering the degrees of freedom associated with significant detuning elements. We develop a comprehensive nonlinear Langevin equation for the filtering model. Through numerical analysis, we demonstrate that the resonance effect effectively doubles the robustness of stationary maximum optomechanical entanglement to thermal fluctuation noise and mechanical damping with our approach. Moreover, we extend the scope of our results to an optical cavity array with an oscillating end-mirror, investigating the potential for long-distance optimal optomechanical entanglement transfer. Our study breaks new ground in applying the resonance effect to protect optomechanical

entanglement from decoherence, providing valuable insights that advance the possibilities of large-scale quantum information processing and quantum network construction.

In Chapter 3, advancements in nanotechnology have driven miniaturization, leading to the rise of quantum devices where quantum effects become prominent. As a novel energy storage device at the atomic scale, the concept of quantum batteries was formally introduced by Alicki and Fannes in 2013. Quantum batteries exploit unique quantum properties, such as entanglement and coherence, for energy storage and release, potentially outperforming classical counterparts by optimizing the charging and discharging processes. Fundamentally distinct from traditional chemical batteries, quantum batteries are renewable, eco-friendly, and have a longer lifespan, offering a promising solution to the global energy and environmental crisis. From an engineering perspective, quantum batteries provide a practical platform to incorporate quantum effects into thermodynamics, sparking a significant interest in theoretical and experimental research over the past decade, with enthusiasm continuing to grow. In particular, a minimal yet widely favored quantum battery model based on a two-level system has been extensively studied.

Recently, the setup of coupling emitters (two-level systems) with a specific waveguide, such as a rectangular hollow metal waveguide, for efficient remote charging has gained significant attention. However, conventional photonic waveguide transport inevitably causes photon dispersion throughout the waveguide, leading to low energy storage and diminished ergotropy in quantum batteries. Motivated by this, a related challenge is whether a structured reservoir exists that can effectively enhance the stored energy and the ergotropy of quantum batteries. Additionally, a significant obstacle to implementing quantum batteries in practical applications is environmental-induced decoherence caused by dissipation, noise, and disorder, which typically degrades quantum battery performance. This raises a natural question: whether a configuration exists that makes quantum batteries more robust against decoherence. Our study provides a

comprehensive solution to substantially address these critical issues, paving the way for the practical application of quantum batteries.

Inspired by the advantages of topological baths and building on recent experimental advancements, we propose a minimal topological quantum battery to optimize the thermodynamic performance of quantum batteries comprehensively. We develop a general framework for analyzing the atomic dynamics of two-level systems coupled to a topological photonic waveguide. First, we demonstrate that in the long-time limit, only bound states significantly contribute to the stored energy of quantum batteries. We point out that topological properties determine the charging process, and near-perfect energy transfer can occur in the topologically nontrivial phase. Moreover, the maximum stored energy exhibits singular behavior at the phase boundaries, where the number of bound states undergoes a transition. Second, we observe that when a quantum battery and a quantum charger are placed within the same sublattice of a unit cell, the performance of the quantum battery, for instance, ergotropy becomes immune to dissipation and against disorder at that location, even with an extremely weak coupling between the quantum battery and the quantum charger, facilitated by a dark state and a topologically robust dressed bound state. Third, we show that as dissipation intensifies along with the emergence of the quantum Zeno effect, the charging power of quantum batteries experiences a temporary boost. Our findings offer valuable guidance and insight for improving quantum battery performance through structured reservoirs, facilitating the development of remote-charging and dissipation-immune engineering for quantum batteries.

Finally, we provide a summary and outlook in Chapter 4. Overall, controlling and suppressing decoherence in open quantum systems is fundamental to unlocking the potential of quantum technologies. While exploring the theoretical mechanisms of decoherence suppression may have a limited immediate impact on society and industry, the long-term implications are significant. Continued research and development in this area will pave the way for more reliable and efficient quantum devices, bringing us closer to realizing the transformative benefits of quantum computing, communication, and sensing.

Doctoral Dissertation

博士論文

Suppression of Decoherence in Open Quantum Systems: Resonance and Topological Effects

(開放量子系におけるデコヒーレンスの抑制: 共鳴とトポロジカル効果)

A Dissertation Submitted for the Degree of Doctor of Philosophy

July 2024

令和 6 年 7 月博士（理学）申請

Department of Physics, Graduate School of Science,

The University of Tokyo

東京大学大学院理学系研究科物理学専攻

Shang Cheng

尚　程

Abstract

In experiments, quantum objects are inevitably open systems influenced by their surrounding environment. Contemporary physics has significantly emphasized the shift from closed to open systems in integrating quantum theory into real-world applications. However, the introduction of the environment causes quantum systems to be affected by quantum noise and dissipation, leading to decoherence. Protecting quantum systems away from decoherence is crucial in open quantum systems. In this Thesis, we investigate how resonance and topological effects can be utilized to suppress decoherence in open quantum systems. We focus on tackling two key challenges in advancing quantum information processing: protecting continuous-variable entanglement and reducing energy-loss in photon transmission.

With the aid of quantum resources, quantum systems often investigate potential advantages in information processing compared to their classical counterparts. Entanglement is a crucial resource in quantum information processing. Unfortunately, it is fragile due to decoherence. First, motivated by entanglement protection, we propose a resonant filtering mechanism to protect optomechanical entanglement. We demonstrate that our filtering model enhances the robustness of the stationary maximum optomechanical entanglement to thermal fluctuation noise and mechanical damping. On the other hand, long-distance transmission of photons is essential for building large-scale quantum networks. However, photons typically disperse throughout the photonic waveguide and are depleted due to environment-induced decoherence. Second, inspired by the development of topological waveguides, we demonstrate how to utilize topological waveguides to achieve near-perfect photon transfer in the topologically nontrivial phase. We also find that when two-level systems are coupled at the same sublattice within a unit cell, the ergotropy becomes immune to dissipation at that location, facilitated by a dark state and a topologically robust dressed bound state. The results of this Thesis are highly relevant to the development of state-of-the-art miniaturized devices and serve as fundamental paradigms for further studies on decoherence suppression in open quantum systems.

List of Publications

The present Thesis is based on the following two works.

- **Cheng Shang** and Hongchao Li, Resonance-dominant optomechanical entanglement in open quantum systems, Phys. Rev. Applied **21**, 044048 (2024).
  (Contains results presented in Chapter 2.)

- Zhi-Guang Lu, Guoqing Tian, Xin-You Lü, and **Cheng Shang** (Corresponding author), Topological Quantum Batteries, arXiv: 2405.03675 (2024).
  (Includes findings presented in Chapter 3.)

The following are related but beyond the scope of this Thesis.

- **Cheng Shang**, Hayato Kinkawa, and Tomotaka Kuwahara, Equivalence between Operator Spreading and Information Propagation, in preparation (2024).

- Bo-Wang Zhang, **Cheng Shang** (Co-first author), Zhuo-cheng Gu, and X. X. Yi, Manipulating spectral transitions and photonic transmission in a non-Hermitian optical system through multi-nanoparticle perturbations, in preparation (2024).

- Zhi-Guang Lu, **Cheng Shang**, Ying Wu, Xin-You Lü, Analytical approach to higher-order correlation functions in U(1) symmetric systems, Physical Review A **108**, 053703 (2023).

- **Cheng Shang**, Coupling enhancement and symmetrization of single-photon optomechanics in open quantum systems, arXiv: 2302.04897 (2023).

- **Cheng Shang**, H. Z. Shen, and X. X. Yi, Nonreciprocity in a strongly coupled three-mode optomechanical circulatory system, Optics Express **27** (18), 25882-25901 (2019).

- H. Y. Sun, **Cheng Shang**, X. X. Luo, Y. H. Zhou, and H. Z. Shen, Optical-assisted Photon Blockade in a Cavity System via Parametric Interactions, International Journal of Theoretical Physics **58**, 3640-3650 (2019).

- H. Z Shen, **Cheng Shang**, Y. H. Zhou, and X. X. Yi, Unconventional single-photon blockade in non-Markovian systems, Phys. Rev. A **98**, 023856 (2018).

Contents

Chapter 1

Overview

A significant trend in contemporary physics is expanding quantum theory from closed to open systems for advanced quantum technology. A quantum system influenced by external factors is considered open. The external influences are often called an environment or a bath. Open quantum systems are microscopic quantum systems that interact with macroscopic materials. In experiments, macroscopic measurement probes interact with experimental objects, leading to quantum systems being unavoidably open. An open system may undergo phase loss, energy, and particle exchange with the surroundings; thus, being open drastically impacts its dynamics [1]. Quantum coherence is a fundamental characteristic of quantum mechanics that accounts for the distinction between the classical and quantum worlds [2, 3]. If a quantum system is perfectly isolated, it will maintain coherence indefinitely. However, manipulating or investigating it would be impossible. For open quantum systems, introducing quantum noise and dissipation leads to environment-induced decoherence, thereby causing the system to lose its quantum nature [4]. Since quantum sources are fragile, even slight external influences can cause them to undergo inevitable decoherence. The theory of decoherence suppression in open quantum systems plays a crucial role in understanding fundamental quantum theory and advancing practical quantum applications [5].

This thesis is devoted to unveiling new mechanisms and establishing innovative frameworks for suppressing decoherence in open quantum systems. We explore how resonance and topological effects can be employed to mitigate decoherence in open quantum systems. We focus on two specific scenarios to protect optomechanical entanglement and enhance quantum

battery performance by utilizing resonant filtering and topological waveguides, respectively. The finding and structure of this thesis is outlined as follows.

In Chapter 2, motivated by entanglement protection, we leverage a resonance effect to enhance optomechanical entanglement in the coherent-state representation. We propose a filtering model to filter out the significant detuning components between a thermal-mechanical mode and its surrounding heat baths in the weak coupling limit. We reveal that protecting continuous-variable entanglement involves the elimination of degrees of freedom associated with significant detuning components, thereby resisting decoherence. We construct a nonlinear Langevin equation of the filtering model and numerically show that the filtering model doubles the robustness of the stationary maximum optomechanical entanglement to the thermal fluctuation noise and mechanical damping. Furthermore, we generalize these results to an optical cavity array with one oscillating end-mirror to investigate the long-distance optimal optomechanical entanglement transfer. Our study breaks new ground by applying the resonance effect to protect quantum systems from decoherence and advance the possibilities of large-scale quantum information processing and quantum network construction.

In Chapter 3, We propose an innovative design for topological quantum batteries that involves coupling two atoms to a one-dimensional lattice with topological features. First, we demonstrate that only coherent bound states significantly contribute to the stored energy of quantum batteries. We observe near-perfect energy transfer from the quantum charger to the quantum battery in the topologically nontrivial phase. Conversely, in the topologically trivial phase, we reveal that under the Markov limit, the charging process of the quantum battery is almost completely prohibited due to the emergence of degenerate zero-energy bound states. Moreover, we discover that the maximum energy storage exhibits singular behavior at the phase boundaries. Second, we find that direct coupling between the quantum battery and quantum charger renders the ergotropy immune to sublattice dissipation, facilitated by the presence of a dark state and a vacancy-like dressed bound state. Further, we show that as dissipation intensifies along with the emergence of the quantum Zeno effect, the charging power of quantum batteries is transiently enhanced. Our findings provide insightful guidelines for practically improving the performance of quantum batteries through structured reservoir engineering.

In Chapter 4, I summarize the thesis and discuss possible advancements in future studies.

In the remainder of this chapter, to analyze the dynamic behavior of open quantum systems, I introduce two powerful techniques central to my thesis for studying dissipative dynamics and spectral properties of interest. By prioritizing a simple setup, I establish a solid foundation in core derivation before progressing to more intricate applications and consequences in subsequent Chapter 2 and Chapter 3.

• *Heisenberg-Langevin equation:* The quantum master equation is a crucial tool for studying the non-equilibrium dynamics of open quantum systems. To describe the dissipative dynamics of open quantum systems, Gorini, Kossakowski, Sudarshan, and Lindblad proposed the GKSL master equation in 1976, which characterizes the evolution of quantum states [6, 7]. The Heisenberg-Langevin equation, which describes stochastic motion, is derived from the perspective of operator evolution by combining the Heisenberg equation and the Langevin equation [8–12]. The Heisenberg-Langevin equations offer exact solutions for the system and bath parameters, enabling direct calculation of correlation functions at different times and all temperatures in terms of the spectral density of the bath. For example, an Ohmic bath with a Drude spectral density enables an exact analytical solution [13].

To lay the technical groundwork for Chapter 2, my goal here is to provide a detailed derivation of the Heisenberg-Langevin equations. Here, I consider a paradigmatic model of open quantum systems called quantum Brownian motion [14]. In this model, the system is considered a harmonic oscillator with linear coupling to a large number of harmonic oscillators that form a bath with a continuous density of states. The spectral density determines the properties of the bath. This simple model has significantly advanced our understanding of how an environmental bath affects the decoherence and dissipation of quantum mechanical degrees of freedom. It sheds light on fundamental decoherence issues and plays a crucial experimental role in designing nanomechanical resonators that operate at the quantum limit [15, 16]. After applying the rotating wave approximation, the total Hamiltonian of the system reads

$$H_{\text{tot}} = H_{\text{sys}} + H_{\text{bath}} + H_{\text{int}} = \omega_0 a^\dagger a + \sum_j \varpi_j \Gamma_j^\dagger \Gamma_j + \sum_j \left(\kappa_j a^\dagger \Gamma_j + \kappa_j^* a \Gamma_j^\dagger\right), \tag{1.1}$$

where $a^\dagger$ (a) and $\Gamma_j^\dagger$ (Γ_j) are the creation (annihilation) operators of the system and the jth mode of the reservoir, respectively, with $(\hbar = 1)$ here and hereafter. The characteristic frequency of the system is ω_0, while the reservoir consists of many harmonic oscillators with closely spaced

frequencies ϖ_j. The coupling strength between the jth mode of the reservoir and the system is represented by the complex parameter κ_j.

The Heisenberg equations of motion for the system operator a and its corresponding reservoir operators Γ_j are given by

$$\frac{da}{dt} = -i\omega_0 a - i\sum_j \kappa_j \Gamma_j, \quad \frac{d\Gamma_j}{dt} = -i\varpi_j \Gamma_j - i\kappa_j^* a. \tag{1.2}$$

I am interested in a closed equation for the system operator a. The reservoir operator Γ_j can be formally integrated to yield

$$\Gamma_j(t) = \Gamma_j(t_0)\, e^{-i\varpi_j(t-t_0)} - i\kappa_j^* \int_{t_0}^{t} d\tau a(\tau)\, e^{-i\varpi_j(t-\tau)}. \tag{1.3}$$

Here, the first term describes the free evolution of the reservoir modes, while the second term arises from their interaction with the system. I eliminate the reservoir operators Γ_j by substituting Eq. (1.2) into Eq. (1.3), obtaining

$$\frac{da}{dt} = -i\omega_0 a - i\sum_j \kappa_j \Gamma_j(t_0)\, e^{-i\varpi_j(t-t_0)} - \sum_j |\kappa_j|^2 \int_{t_0}^{t} d\tau a(\tau)\, e^{-i\varpi_j(t-\tau)}. \tag{1.4}$$

I observe that the evolution of the system operator depends on the fluctuations from the reservoir, as described in Eq. (1.4). Next, I make some approximations. Following the Weisskopf-Wigner approximation [17], I assume that the spectrum is defined by the normal modes of a large scale, with these modes being very close in frequency. I then approximate this spectrum as a continuous one. Consequently, the summation in Eq. (1.4) can be rewritten as

$$\frac{da}{dt} = -i\omega_0 a + \mathcal{F}(t) - \int_{t_0}^{t}\int_{0}^{+\infty} \kappa^2(\omega)\mathcal{D}(\omega)\, a(\tau)\, e^{-i\omega(t-\tau)} d\omega d\tau, \tag{1.5}$$

where $\mathcal{D}(\omega)$ is the mode density of the reservoir, and the Langevin noise operator is

$$\mathcal{F}(t) = -i\int_{0}^{+\infty} \kappa(\omega)\mathcal{D}(\omega)\,\Gamma(\omega, t_0)\, e^{-i\omega(t-t_0)} d\omega. \tag{1.6}$$

Under the Born-Markov approximation [18], I assume for simplicity that $\kappa^2(\omega)\mathcal{D}(\omega) =$

$\gamma/2\pi > 0$ is constant, so that Eq. (1.5) is reduced to a first-order differential equation

$$\frac{da}{dt} = -i\omega_0 a + \mathcal{F}(t) - \frac{\gamma}{2\pi}\int_{t_0}^{t}\int_{0}^{+\infty} a(\tau)\, e^{-i\omega(t-\tau)} d\omega d\tau. \tag{1.7}$$

Using the relation $\int_0^{+\infty} d\omega e^{-i\omega(t-\tau)} = \pi\delta(t-\tau)$, I derive the Heisenberg-Langevin equation, which satisfies the fluctuation-dissipation theorem, as follows

$$\frac{da}{dt} = -\left(i\omega_0 + \frac{\gamma}{2}\right) a + \mathcal{F}(t). \tag{1.8}$$

Here, the noise operators in $\langle \mathcal{F}(t)\, \mathcal{F}^{\dagger}(t')\rangle = \gamma(\bar{n}+1)\,\delta(t-t')/2$, also $\langle \mathcal{F}^{\dagger}(t)\, \mathcal{F}(t')\rangle = \gamma\bar{n}\delta(t-t')/2$ satisfy the correlation function form of Markovian white noise, where $\bar{n}$ represents the average number of bosons in the reservoirs, and γ denotes the decay rate that depends on the coupling strength κ_j. Note that white noise implies frequency resonance between the environment and the system. Moreover, the Markov approximation generally applies when there is weak coupling between the system and the environment. When the system and the environment are strongly coupled, the spectral density typically shows a generalized Lorentzian type, which indicates non-Markovian behavior [1, 19, 20].

• *Resolvent formalism:* The concept of resolvent formalism is vital for analyzing the spectrum of operators on Banach and other general spaces. This method is well-supported within the context of holomorphic functional calculus. Ivar Fredholm was the first to use the resolvent operator as a series, notably the Liouville-Neumann series, in his influential 1903 work [21]. Today, this approach is widely used in the spectral analysis of open quantum systems, encompassing fields such as quantum chemistry and quantum thermodynamics [22]. Here, we present a paradigmatic model of a quantum battery to lay the groundwork for Chapter 3, offering the exact dynamical expression for two-level systems coupled with a structured bosonic bath. The Hamiltonian of the system under the rotating-wave approximation reads $H_{\text{tot}} = H_{\text{sys}} + H_{\text{bath}} + H_{\text{int}}$, where

$$H_{\text{sys}} = \frac{\omega_e}{2}\left(\sigma_z^{\text{B}} + \sigma_z^{\text{C}}\right) + \Omega_{12}^{\alpha\beta}(\sigma_+^{\text{B}}\sigma_-^{\text{C}} + \sigma_+^{\text{C}}\sigma_-^{\text{B}}), H_{\text{int}} = \text{g}(\sigma_-^{\text{B}} o_{x_{1,\alpha}}^{\dagger} + \sigma_-^{\text{C}} o_{x_{2,\beta}}^{\dagger} + \text{H.c.}), \tag{1.9}$$

and $\Omega_{12}^{\alpha\beta} = \Omega\delta_{x_1,x_2}\delta_{\alpha,\beta}$ with $\Omega \in \mathbb{R}$. Here, H_{sys} represents the Hamiltonian of the quantum battery and the quantum charger, while H_{bath} is the Hamiltonian of the structured bosonic bath.

The interaction Hamiltonian between the system and the bath is represented by H_{int}, where σ_{+}^{B} (σ_{+}^{C}) and σ_{-}^{B} (σ_{-}^{C}) represent the raising and lowering Pauli operators of quantum battery (quantum charger), respectively, while $o_{x_{j,\alpha}}$ and $o_{x_{j,\alpha}}^{\dagger}$ denote the annihilation and creation operators at the position $x_{j,\alpha}$ of bath, respectively. I assume that the spectrum of H_{bath} possesses an energy-band structure. The second subscript $\alpha \in \{A, B\}$ of $o_{x_{j,\alpha}}$ is used to emphasize different sublattices, i.e., $o_{x_{j,A}} \equiv a_j$ and $o_{x_{j,B}} \equiv b_j$.

To analytically solve the dynamics of the two-level system, I assume that the bath is in the thermodynamic limit in the following derivations. Consequently, the time-evolution operator of the system can be obtained by the inverse Fourier transform of the Green's function

$$U(t) = e^{-iH_{\text{tot}}t} = \frac{1}{2\pi i}\int_{\mathcal{C}} G_{\text{tot}}(z) e^{-izt} dz = \frac{1}{2\pi i}\int_{\mathcal{C}} \frac{1}{z - H_{\text{tot}}} e^{-izt} dz, \tag{1.10}$$

where the integration path $\mathcal{C}$ lies just above the real axis in the complex plane, extending infinitely from right to left. In the single-excitation subspace, in order to explore the dynamics of quantum battery, I need to project the evolution operator $U(t)$ onto the subspace of the system involving quantum battery and quantum charger. Thus, I define

$$P \equiv (|e,g\rangle\langle e,g| + |g,e\rangle\langle g,e|) \otimes |\text{vac}\rangle\langle\text{vac}|\,,\ Q \equiv |g,g\rangle\langle g,g| \otimes \sum_{j,\alpha} o_{j,\alpha}^{\dagger} |\text{vac}\rangle\langle\text{vac}|\, o_{j,\alpha}, \tag{1.11}$$

which satisfy $P + Q = \mathbb{I}_1$, where $\mathbb{I}_1$ is the identity operator in the single-excitation subspace. For the sake of simplicity, we define $|e_1\rangle \equiv |e,g\rangle$ and $|e_2\rangle \equiv |g,e\rangle$. As a result, the evolution operator projected onto the subspace of the system can be written as

$$PU(t)\,P = \frac{1}{2\pi i}\int_{\mathcal{C}} PG_{\text{tot}}(z) P e^{-izt} dz, \tag{1.12}$$

where

$$PG_{\text{tot}}(z)\,P = \frac{P}{z - PH_{\text{sys}}P - P\Sigma(z)\,P}. \tag{1.13}$$

Since $PH_{\text{int}}P = QH_{\text{int}}Q = QH_{\text{sys}}Q = 0$, the term $P\Sigma(z)\,P$ in Eq. (1.13) reads

$$P\Sigma(z)\,P = PH_{\text{int}}\frac{Q}{z - H_{\text{bath}}}H_{\text{int}}P = PH_{\text{int}}G_{\text{bath}}(z)\,H_{\text{int}}P \tag{1.14}$$

with $G_{\text{bath}}(z) = Q(z - H_{\text{bath}})^{-1}Q$. In the basis $\{|e_1; \text{vac}\rangle, |e_2; \text{vac}\rangle\}$, Eq. (1.13) can be written in a matrix form as

$$\begin{bmatrix} G_{11}(z) & G_{12}(z) \\ G_{21}(z) & G_{22}(z) \end{bmatrix} = \begin{bmatrix} z - \omega_e - \Sigma_{11}(z) & -\Omega_{12}^{\alpha\beta} - \Sigma_{12}(z) \\ -\Omega_{12}^{\alpha\beta} - \Sigma_{21}(z) & z - \omega_e - \Sigma_{22}(z) \end{bmatrix}^{-1}, \tag{1.15}$$

where $G_{mn}(z) = \langle e_m; \text{vac}| PG_{\text{tot}}(z) P |e_n, ; \text{vac}\rangle$, and $\Sigma_{mn}(z) = \langle e_m; \text{vac}|P\Sigma(z) P |e_n; \text{vac}\rangle$ refers to the self-energy of the two-level systems. According to Eq. (1.14), by inserting H_{int} into $\Sigma_{mn}(z)$, I have

$$\begin{aligned}
\Sigma_{11}^{\alpha\alpha}(z) &= \Sigma_{11}(z) = \text{g}^2 \langle \text{vac}|o_{x_{1,\alpha}}(z - H_{\text{bath}})^{-1}o_{x_{1,\alpha}}^{\dagger}|\text{vac}\rangle \equiv \text{g}^2 G(x_{1,\alpha}, x_{1,\alpha}; z), \\
\Sigma_{12}^{\alpha\beta}(z) &= \Sigma_{12}(z) = \text{g}^2 \langle \text{vac}|o_{x_{1,\alpha}}(z - H_{\text{bath}})^{-1}o_{x_{2,\beta}}^{\dagger}|\text{vac}\rangle \equiv \text{g}^2 G(x_{1,\alpha}, x_{2,\beta}; z), \\
\Sigma_{21}^{\beta\alpha}(z) &= \Sigma_{21}(z) = \text{g}^2 \langle \text{vac}|o_{x_{2,\beta}}(z - H_{\text{bath}})^{-1}o_{x_{1,\alpha}}^{\dagger}|\text{vac}\rangle \equiv \text{g}^2 G(x_{2,\beta}, x_{1,\alpha}; z), \\
\Sigma_{22}^{\beta\beta}(z) &= \Sigma_{22}(z) = \text{g}^2 \langle \text{vac}|o_{x_{2,\beta}}(z - H_{\text{bath}})^{-1}o_{x_{2,\beta}}^{\dagger}|\text{vac}\rangle \equiv \text{g}^2 G(x_{2,\beta}, x_{2,\beta}; z),
\end{aligned} \tag{1.16}$$

where G represents the single-particle Green's function of the bath. As a result, according to Eq. (1.15), the projected evolution operator in Eq. (1.12) is given by $PU(t) P$:

$$\frac{1}{2\pi i}\int_{\mathcal{C}} \text{d}z \, \frac{e^{-izt}}{\mathscr{D}(z)} \begin{bmatrix} |e_1; \text{vac}\rangle \\ |e_2; \text{vac}\rangle \end{bmatrix}^T \begin{bmatrix} z - \omega_e - \Sigma_{22}^{\beta\beta}(z) & \Omega_{12}^{\alpha\beta} + \Sigma_{21}^{\beta\alpha}(z) \\ \Omega_{12}^{\alpha\beta} + \Sigma_{12}^{\alpha\beta}(z) & z - \omega_e - \Sigma_{11}^{\alpha\alpha}(z) \end{bmatrix} \begin{bmatrix} \langle e_1; \text{vac}| \\ \langle e_2; \text{vac}| \end{bmatrix}, \tag{1.17}$$

where

$$\mathscr{D}(z) = [z - \omega_e - \Sigma_{11}^{\alpha\alpha}(z)][z - \omega_e - \Sigma_{22}^{\beta\beta}(z)] - [\Omega_{12}^{\alpha\beta} + \Sigma_{12}^{\alpha\beta}(z)][\Omega_{12}^{\alpha\beta} + \Sigma_{21}^{\beta\alpha}(z)]. \tag{1.18}$$

Now let us assume that the total system is prepared in the initial state, $|\psi(0)\rangle = |e_1; \text{vac}\rangle$, i.e., the quantum charger is in the excited state, the quantum battery is in the ground state, and the environment is in the vacuum state. According to Eq. (1.17), the probability amplitude for the quantum battery to be excited at t time is given by

$$c_{\text{B}}(t) = \langle e_2; \text{vac}|PU(t)P |e_1; \text{vac}\rangle = \frac{1}{2\pi i}\int_C \frac{\Sigma_{12}^{\alpha\beta} + \Omega_{12}^{\alpha\beta}}{\mathscr{D}(z)} e^{-izt} dz. \tag{1.19}$$

The reduced density matrix of the quantum battery is $\rho_{\text{B}}(t) = \text{Tr}_{\text{charger}\otimes\text{bath}}[|\psi(t)\rangle\langle\psi(t)|] = |c_{\text{B}}(t)|^2 |e\rangle\langle e| + [1 - |c_{\text{B}}(t)|^2] |g\rangle\langle g|$.

Chapter 2

Resonance-dominant optomechanical entanglement in open quantum systems

2.1 Introduction

Entanglement is an essential feature of quantum systems and one of the most striking phenomena of quantum theory [23], allowing for inseparable quantum correlations shared by distant parties [24]. Entanglement is crucial in quantum information processing and network building [25–27]. Studying entanglement properties from the perspectives of discrete and continuous variables is significant for further understanding the quantum-classical correspondence [28,29]. So far, the bipartite entanglement for a microscopic system of discrete variables with a few degrees of freedom has been studied in detail [30]. A primary example of this is a two-qubit system. To quantify entanglement, the concurrence [31], the negativity [32], and the von Neumann entropy [33] are frequently used in previous studies.

Nevertheless, exploring bipartite entanglement in a macroscopic system of continuous variables with a large number of degrees of freedom has remained elusive [34–37]. Unfortunately, entanglement is fragile due to decoherence from inevitable dissipative couplings between an entangled system and its surrounding environment. Therefore, generating, measuring, and protecting entanglement in open quantum systems have raised widespread interest in various branches of physics and have been expected to be demonstrated to date [38].

Cavity optomechanical systems are based on couplings due to radiation pressure between electromagnetic and mechanical degrees of freedom [39]. They provide a desirable mesoscopic platform for studying continuous-variable entanglement between optical cavity fields and macroscopic mechanical oscillators with vast degrees of freedom in open quantum systems [40, 41]. Thanks to the rapidly developing field of microfabrication, quantum effects are becoming more significant as the size of the device shrinks [42, 43]. Remarkable progress has been made in generating entanglement by manipulating macroscopic nanomechanical oscillators with high precision [44, 45]. Some landmark contributions have been achieved for an optomechanical entanglement measure [46, 47], such as using logarithmic negativity to calculate an upper bound of distillable optomechanical entanglement [48].

Protecting the maximum optomechanical entanglement in open quantum systems has recently become a research focus. Many schemes have been proposed, such as protecting entanglement via synthetic magnetism in loop-coupled cavity optomechanical systems from thermal noise and the dark mode [49], realizing phase-controlled asymmetric entanglement in cavity optomechanical systems of the whispering-gallery mode [50], achieving and preserving the optimal quality of nonreciprocal optomechanical entanglement via the Sagnac effect in a spinning cavity optomechanical systems evanescently coupled with a tapered fiber [51, 52], as well as via general dark-mode control to accomplish thermal-noise-resistant entanglement [53].

However, the auxiliary protection of optomechanical entanglement in these schemes all work in hybrid cavity optomechanical systems, which inevitably brings about trilateral and even multilateral entanglement problems [54], such as photon-phonon-atom entanglement [55]. In this sense, it is essential to develop methods of protecting the intrinsic bilateral optomechanical entanglement in hybrid cavity optomechanical systems from potential interference caused by additional types of degrees of freedom [56]. With this motivation, we aim to protect a prototypical optomechanical entanglement in cavity optomechanical systems.

Currently, intriguing schemes have been proposed to achieve the frequency resonance of the system by using laser driving, thereby protecting bilateral mechanical entanglement in doubly resonant cavity optomechanical systems [57, 58] and photon-atom entanglement in the Rabi model [59]. Inspired by this, we propose to utilize the high-frequency resonance effect in a Fabry-Pérot cavity to protect the maximal value of optomechanical entanglement.

In the weak-coupling limit, a clear-cut physical mechanism is employed to reduce Brownian noise and dissipation, which involves filtering out components with significant mismatched coupling frequencies between a mechanical mode and its thermal reservoir by leveraging the high-frequency resonance effect. The present theoretical conjecture can be materialized in an experiment by laser-driving the optical cavity field to resonate with a high-frequency and high-quality-factor mechanical resonator coupled to a Markovian structured environment. We can observe resonance-dominant optomechanical entanglement using a homodyne detection scheme [60, 61] or a cavity-assisted measurement scheme [62, 63].

To attain our goal, we start by constructing the Hamiltonian of the cavity optomechanical system under the coherent-state representation. We then derive its associated nonlinear Langevin equations, which are consistent with the results in Ref. [46] but originate from the coherent-state representation. We finally propose a theory of resonance-dominant optomechanical entanglement in continuous-variable systems. When the mechanical mode and surrounding heat baths satisfy the conditions of a weak coupling and a high-frequency resonance, we point out that the filtering model protects the stationary maximum optomechanical entanglement. In particular, we quantitatively observe that a resonance effect doubles the robustness of the mechanical damping and thermal fluctuation noise from the environment and reveals its physical reason. This result first unveils a hitherto overlooked aspect of applying a resonance effect to entanglement protection. We further extend these results to an array of optical cavities with one oscillating end-mirror and investigate the remote optomechanical entanglement, which helps achieve optimal optomechanical entanglement transmission for quantum information processing.

The remainder of this chapter is organized as follows. In Sec. 2.2, we construct the Hamiltonian of the physical system and reproduce the results of nonlinear Langevin equations in Ref. [46] in the coherent-state representation. In Sec. 2.3, we propose a theory of resonance-dominant optomechanical entanglement in continuous-variable systems and show the results for maximum optomechanical entanglement protection. In addition, we present a potential experimental implementation of this scheme. In Sec. 2.4, we extend these findings to an array of optical cavities with one oscillating end-mirror, investigating the remote optimal optomechanical entanglement transmission for application purposes. Finally, in Sec. 2.5, we summarize our findings and discuss the outlook for future research.

2.2 Dynamics in coherent state representation

2.2.1 Construction of Hamiltonian

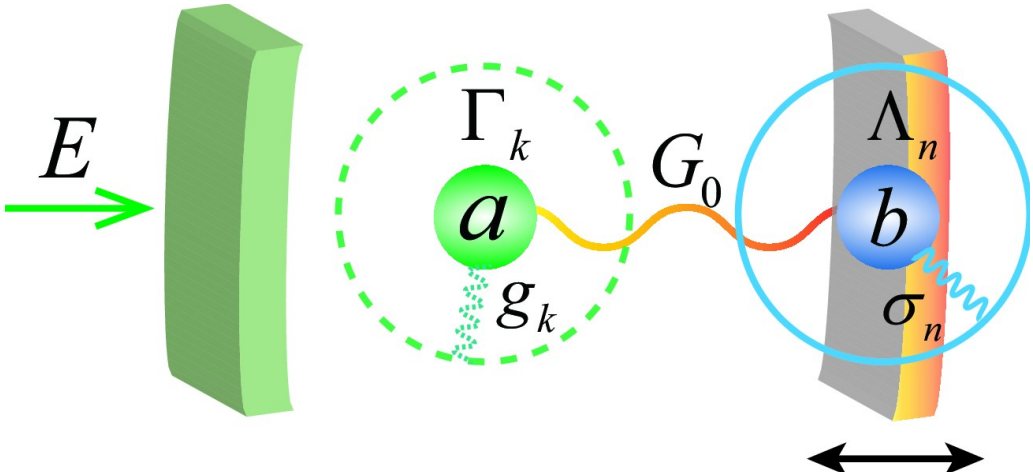

Figure 2.1: A cavity optomechanical system driven by a monochromatic laser. The optical and mechanical modes are coupled via radiation pressure while independently coupled to their respective reservoirs.

We first construct an open-quantum-system description of a cavity optomechanical system in the coherent-state representation as shown in Fig. 2.1. The Fabry-Pérot cavity, known as the simplest optical resonator structure, is additionally driven by a monochromatic laser, described by the radiation-pressure interaction between an optical cavity field and a vibrating end mirror, which applies to a wide variety of optomechanical devices, including microwave resonators [64], optomechanical crystals [65], and setups with the membrane inside a cavity [66].

Meanwhile, we assume that a cavity optomechanical system is coupled to two reservoirs. The optical mode is coupled to a reservoir characterized by zero-temperature electromagnetic modes, while the mechanical mode is coupled to another reservoir consisting of harmonic oscillators at thermal equilibrium [17]. In the Heisenberg picture, the system and environment evolve in time under the influence of the total Hamiltonian, which reads [67]

$$H_{\mathrm{T}} = H_{\mathrm{S}} + H_{\mathrm{B}}, \tag{2.1}$$

where

$$H_{\mathrm{S}} = +\hbar\Delta_0 a^\dagger a + \hbar\omega_{\mathrm{m}} b^\dagger b - \hbar\frac{G_0}{\sqrt{2}} a^\dagger a\left(b^\dagger + b\right) + i\hbar\left(Ea^\dagger - E^* a\right), \tag{2.2}$$

$$\begin{aligned} H_{\mathrm{E}} = &+\hbar\sum_k \omega_k \Gamma_k^\dagger \Gamma_k + \hbar\sum_k g_k\left(\Gamma_k^\dagger a + a^\dagger \Gamma_k\right) \\ &+\hbar\sum_n \omega_n \Lambda_n^\dagger \Lambda_n - i\hbar\sum_n \frac{\ell_n}{2}\left(\Lambda_n^\dagger - \Lambda_n\right)\left(b^\dagger + b\right), \end{aligned} \tag{2.3}$$

with $a^\dagger$ (a) denoting $b^\dagger$ (b) are the creation (annihilation) operators of the optical mode and the mechanical mode, respectively. Laser detuning from the cavity resonance is $\Delta_0 = \omega_{\mathrm{c}} - \omega_L$, where ω_{c} is the cavity characteristic frequency and ω_L the is driving laser frequency. The characteristic frequency and effective mass of the mechanical oscillator are ω_{m} and m, respectively. The optomechanical coupling coefficient is $G_0 = (\omega_{\mathrm{c}}/L)\sqrt{\hbar/m\omega_{\mathrm{m}}}$, with L being the cavity length. The complex amplitude of the driving laser is E. In addition, $\Gamma_k^\dagger$ (Γ_k) and $\Lambda_n^\dagger$ (Λ_n) for $k \in \{1, 2, 3\cdots, +\infty\}$ and $n \in \{1, 2, 3\cdots, +\infty\}$ are, respectively, the creation (annihilation) operators of the reservoirs for the optical mode and the mechanical mode. The harmonic-oscillator reservoirs have closely spaced frequencies corresponding to photons and phonons, denoted by ω_k and ω_n, respectively. The real numbers g_k and ℓ_n represent the coupling strengths between the subsystem and the nth reservoir mode, respectively. Details of the derivations of the total Hamiltonian (2.1) are given in Appendix A.1 [8, 64].

2.2.2 Nonlinear Langevin equations

A reasonable description of the dynamics in an open quantum system should include photon losses in the optical cavity field and the Brownian noise acting on the vibrating end mirror. By substituting the total Hamiltonian (2.1) into the Heisenberg equation and taking into account the dissipation and noise terms, we obtain a set of closed integrodifferential equations (see Appendix A.2 for the derivation [8, 17, 18, 68]) for the operators of the optical mode and

mechanical mode as follows:

$$\dot{q} = \omega_{\mathrm{m}} p, \tag{2.4}$$

$$\dot{p} = -\omega_{\mathrm{m}} q - \gamma_{\mathrm{m}} p + G_0 a^{\dagger} a + \xi, \tag{2.5}$$

$$\dot{a} = -\left(\kappa + i\Delta_0\right) a + i G_0 a q + E + \sqrt{2\kappa} a_{\mathrm{in}}, \tag{2.6}$$

where $q = \left(b^{\dagger} + b\right)/\sqrt{2}$ and $p = i\left(b^{\dagger} - b\right)/\sqrt{2}$ are the dimensionless position and momentum operators of the vibrating end mirror. We assume that the decay rate of the optical cavity is κ and set the mechanical damping rate as $\gamma_{\mathrm{m}} = \omega_{\mathrm{m}}\gamma$. The dissipative terms κ and γ are proportional to the square of the coupling strength between the subsystem and the reservoir g_k and ℓ_n, respectively. The optical Langevin force a_{in} represents the field incident to the cavity and is assumed to be in the vacuum state. Its specific expression and the correlation function [69] are

$$a_{\mathrm{in}}(t) = \frac{-i}{\sqrt{2\pi}} \sum_k g_k \Gamma(t_0)\, e^{-i\omega_k (t - t_0)}, \quad \left\langle a_{\mathrm{in}}(t)\, a_{\mathrm{in}}^{\dagger}(t') \right\rangle = \delta(t - t'), \tag{2.7}$$

where t_0 represents the initial time. This correlation function is true for optical fields at room temperature or microwaves at a cryostat.

In contrast, the Brownian noise operator is given by

$$\xi(t) = \sum_n \frac{i\ell_n}{\sqrt{2}} \left[\Lambda_n^{\dagger}(t_0)\, e^{i\omega_n (t - t_0)} - \Lambda_n(t_0)\, e^{-i\omega_n (t - t_0)}\right], \tag{2.8}$$

The mechanical damping force ξ is non-Markovian in general [70], but it can be treated as Markovian if the following two conditions are met: the thermal bath occupation number satisfies $\bar{n} \gg 1$; the mechanical quality factor satisfies $Q = \omega_{\mathrm{m}}/\gamma_{\mathrm{m}} = 1/\gamma \gg 1$. These conditions are well satisfied in the majority of contemporary experimental setups, which validates the use of the standard Markovian delta-correlation [68, 71]:

$$\frac{\langle \xi(t)\, \xi(t') + \xi(t')\, \xi(t) \rangle}{2} \approx \gamma_{\mathrm{m}} \left(2\bar{n} + 1\right) \delta(t - t'), \tag{2.9}$$

where $\bar{n} = \left[\exp\left(\hbar\omega_{\mathrm{m}}/k_{\mathrm{B}}T\right) - 1\right]^{-1}$ is the mean thermal excitation number with the Boltzmann constant k_{B} and the end-mirror temperature T.

So far, we have constructed the total Hamiltonian of the optomechanical system under the coherent-state representation and completely reproduced the results of the nonlinear Langevin equations in Ref. [46], which provides solid support for the filtering model dominated by the resonance effect discussed later. We stress that deriving the Langevin equation from the total Hamiltonian provides a clear picture in explicitly revealing the specific form of the interaction between the system and the environment and the physical origin of each term in nonlinear Langevin equations, in comparison to the implicit treatment of such interactions in the Lindblad master equation.

2.3 Resonance-dominant optomechanical entanglement

2.3.1 Filtering model

In the preceding section, the total Hamiltonian (2.1) describes an original interaction between an optomechanical system and its surrounding environment. This section proposes a resonant filtering model in the weak-coupling limit between the system and the heat bath. It uses a high-frequency resonance between the mechanical mode and its thermal reservoirs to filter out nonresonant degrees of freedom and achieve quantum coherence protection.

To discuss the frequency relation between the mechanical mode and its thermal reservoirs, we introduce the frequency transformation $\tilde{b}\left(t\right)=b\left(t\right)\exp\left(i\omega_{\mathrm{m}}t\right)$ and $\tilde{\Lambda}_{n}\left(t\right)=\Lambda_{n}\left(t\right)\exp\left(i\omega_{n}t\right)$ for $b\left(t\right)$ and $\Lambda_{n}\left(t\right)$ [17] in the interaction picture. After that, the Hamiltonian (2.1) reads

$$\begin{aligned}H_{\mathrm{T}}=&+\hbar\Delta_{0}a^{\dagger}a+\hbar\omega_{\mathrm{m}}b^{\dagger}b+i\hbar\left(Ea^{\dagger}-E^{*}a\right)-\hbar\frac{G_{0}}{\sqrt{2}}a^{\dagger}a\left(\tilde{b}^{\dagger}e^{i\omega_{\mathrm{m}}t}+\tilde{b}e^{-i\omega_{\mathrm{m}}t}\right)\\&+\hbar\sum_{k}\omega_{k}\Gamma_{k}^{\dagger}\Gamma_{k}+\hbar\sum_{k}g_{k}\left(\Gamma_{k}^{\dagger}a+a^{\dagger}\Gamma_{k}\right)+\hbar\sum_{n}\omega_{n}\Lambda_{n}^{\dagger}\Lambda_{n}\\&-i\hbar\sum_{n}\frac{\ell_{n}}{2}\left[\tilde{\Lambda}_{n}^{\dagger}\tilde{b}e^{i(\omega_{n}-\omega_{\mathrm{m}})t}-\tilde{b}^{\dagger}\tilde{\Lambda}_{n}e^{-i(\omega_{n}-\omega_{\mathrm{m}})t}\right]\\&-i\hbar\sum_{n}\frac{\ell_{n}}{2}\left[\tilde{\Lambda}_{n}^{\dagger}\tilde{b}^{\dagger}e^{i(\omega_{n}+\omega_{\mathrm{m}})t}-\tilde{b}\tilde{\Lambda}_{n}e^{-i(\omega_{n}+\omega_{\mathrm{m}})t}\right].\end{aligned}\tag{2.10}$$

As mentioned above, our physical model describes a Markovian process in the weak-coupling limit $\gamma\ll1$, which corresponds to Eq. (2.10) satisfying the weak-coupling limit $\ell_{n}\ll1$ for

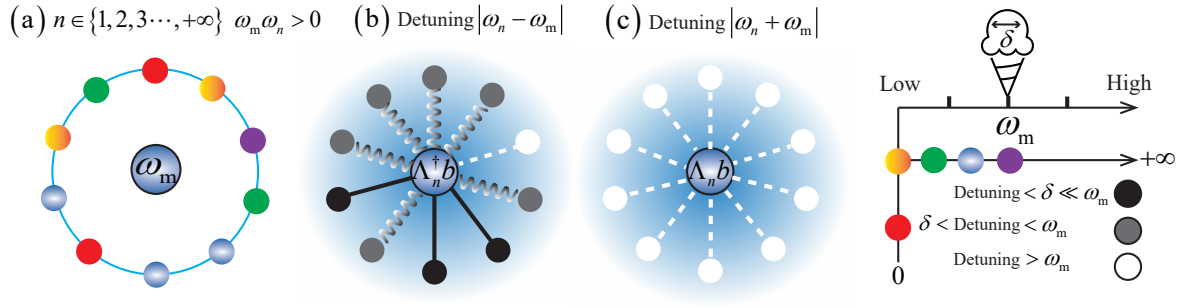

Figure 2.2: Schematic diagram of the filtering model. (a) The coupling between a high-frequency mechanical oscillator and codirectional thermal reservoirs. The frequency of the thermal reservoirs sequentially transits from zero to positive infinity in rainbow color order. (b) The terms of $\tilde{\Lambda}_n^\dagger \tilde{b}$ and $\tilde{b}^\dagger \tilde{\Lambda}_n$ show the high-frequency resonance effect. (c) The terms of $\tilde{\Lambda}_n^\dagger \tilde{b}^\dagger$ and $\tilde{b}\tilde{\Lambda}_n$ exhibit large detuning effects. The black, gray, and white colors correspond to the high-frequency resonance, moderately detuned, and highly detuned modes of the heat bath compared to the frequency of the single-mode mechanical oscillator ω_{m}. The parameters δ and ω_{m} can be modulated by coherent laser driving [72, 73].

$n \in \{1, 2, 3 \cdot \cdot\cdot, +\infty\}$ [74]. See Fig. 2.2 for a schematic diagram of the filtering model. We eliminate the relatively fast-oscillating terms from Eq. (2.10) and then perform the inverse frequency transformation as $b\,(t) = \tilde{b}\,(t)\, e^{-i\omega_{\mathrm{m}} t}$ and $\Lambda_n\,(t) = \tilde{\Lambda}_n\,(t)\, e^{-i\omega_n t}$. Through this process, we classify the filtering model reduced from Eq. (2.10) into the following two cases.

The high-frequency resonance region commonly exists in the coupling between the mechanical mode and a heat bath composed of positive energy modes denoted as $\omega_{\mathrm{m}}\omega_n > 0$ and $\omega_n \in (0, +\infty)$. The high-frequency resonance results in level repulsion between ω_{m} and ω_n [75]. We here propose to filter out the strongly non-resonant contributions $\tilde{\Lambda}_n^\dagger \tilde{b}^\dagger$ and $\tilde{b}\tilde{\Lambda}_n$ mechanically; see Sec. 2.3.4 for possible experimental realizations. Keeping only the resonant terms $\tilde{\Lambda}_n^\dagger \tilde{b}$ and $\tilde{b}^\dagger \tilde{\Lambda}_n$, the filtering model is $H_{\mathrm{F}} = H_{\mathrm{T}} + i\hbar \sum_n \ell_n \left(\Lambda_n^\dagger b^\dagger - \Lambda_n b\right)/2$. The resonance terms $\tilde{\Lambda}_n^\dagger \tilde{b}$ and $\tilde{b}^\dagger \tilde{\Lambda}_n$ in this region describe the exchange of quanta between the mechanical mode and its nth thermal reservoir mode [42].

In contrast, the high-frequency inverse-resonance region occurs in the coupling between the mechanical mode and an unstable heat bath composed of negative energy modes, denoted as $\omega_{\mathrm{m}}\omega_n < 0$ and $\omega_n \in (-\infty, 0)$. The high-frequency inverse resonance results in level attraction between ω_{m} and ω_n, details can be found in Appendix A.3 [52, 76–84]. Keeping only the terms

of $\tilde{\Lambda}_n^\dagger \tilde{b}^\dagger$ and $\tilde{b}\tilde{\Lambda}_n$, the inverse-filtering model reads $H_{\mathrm{F}}^{\mathrm{I}} = H_{\mathrm{T}} + i\hbar \sum_n \ell_n \left(\Lambda_n^\dagger b - b^\dagger \Lambda_n\right)/2$. The inverse-resonance terms $\tilde{\Lambda}_n^\dagger \tilde{b}^\dagger$ and $\tilde{b}\tilde{\Lambda}_n$ in this region represent a two-mode squeezing interaction between the mechanical mode and its nth thermal reservoir mode, and the parametric amplification relies on the two-mode squeezing interaction [85]. In the following, we focus on discussing the high-frequency resonance range since its physical significance is clear and universal.

2.3.2 The Lyapunov equation for the steady-state correlation matrix

In order to comprehend the impact of resonance effects between a mechanical mode and its thermal reservoirs on the strength of an optomechanical system, it is crucial to gain insight into the structure of optomechanical correlation in open quantum systems. For this purpose, we use the Lyapunov equation to compute the steady-state correlation matrix between subsystems and obtain the optomechanical entanglement strength [86]. Without loss of generality, we take the high-frequency resonance regime as an example of deriving the Lyapunov equation in terms of the steady-state correlation matrix.

By deriving the Heisenberg equation of motion of the resonant Hamiltonian H_{F}, we obtain nonlinear Langevin equations that govern the dynamical behavior of the optomechanical system in the high-frequency resonance regime. The nonlinear Langevin equations are written as (see Appendix A.4 for details)

$$\dot{q} = \omega_{\mathrm{m}} p + \frac{\gamma}{4}\dot{p} + \frac{1}{2}\xi', \tag{2.11}$$

$$\dot{p} = -\omega_{\mathrm{m}} q - \frac{\gamma}{4}\dot{q} + G_0 a^\dagger a + \frac{1}{2}\xi, \tag{2.12}$$

$$\dot{a} = -\left(\kappa + i\Delta_0\right) a + iG_0 aq + E + \sqrt{2\kappa}a_{\mathrm{in}}, \tag{2.13}$$

where the Brownian noise operator reads

$$\xi'(t) = \sum_n \frac{\ell_n}{\sqrt{2}} \left[\Lambda_n^\dagger(t_0)\, e^{i\omega_n (t-t_0)} + \Lambda_n(t_0)\, e^{-i\omega_n (t-t_0)}\right], \tag{2.14}$$

which has the same delta-correlated form as $\xi(t)$ under the weak-coupling limit $\gamma \ll 1$. The nonlinear Langevin equations (2.11)-(2.13) are inherently nonlinear as they contain a product

of the photon operator and dimensionless position operator of the mechanical phonon, aq, as well as a quadratic term in photon operators, $a^\dagger a$. Using the standard mean-field method [87] to solve Eqs. (2.11)-(2.13), we start by splitting each Heisenberg operator into the classical mean values and quantum fluctuation operators, i.e., $a = \alpha_\mathrm{s} + \delta a$ as in $a^\dagger = \alpha_\mathrm{s}^* + \delta a^\dagger$, $q = q_\mathrm{s} + \delta q$, and $p = p_\mathrm{s} + \delta p$, thereby linearizing these equations. Adopting the above approach and inserting these expressions into nonlinear Langevin equations (2.11)-(2.13), we find the solution of the mean values for the classical steady state given by $p_\mathrm{s} = 0$, $q_\mathrm{s} = G_0\alpha_\mathrm{s}^*\alpha_\mathrm{s}/\omega_\mathrm{m}$, and $\alpha_\mathrm{s} = E/(\kappa + i\Delta)$, where we set normalization of the detuning frequency of the optical field as $\Delta = \Delta_0 - G_0^2\alpha_\mathrm{s}^*\alpha_\mathrm{s}/\omega_\mathrm{m}$.

The parameter regime for generating optomechanical entanglement is the one with a large amplitude of the driving laser E, i.e., $\alpha_\mathrm{s} \gg \delta a$ and $\alpha_\mathrm{s}^* \gg \delta a^\dagger$. By dropping the contribution from the second-order small terms, as described in Appendix A.5, we obtain the linearized Langevin equations

$$\delta\dot{q} = \omega_\mathrm{m}\delta p - \frac{\gamma_\mathrm{m}}{4}\delta q + \frac{1}{2}\xi', \tag{2.15}$$

$$\delta\dot{p} = -\omega_\mathrm{m}\delta q - \frac{\gamma_\mathrm{m}}{4}\delta p + G_0\left(\alpha_\mathrm{s}^*\delta a + \alpha_\mathrm{s}\delta a^\dagger\right) + \frac{1}{2}\xi, \tag{2.16}$$

$$\delta\dot{a} = -\left(\kappa + i\Delta\right)\delta a + iG_0\alpha_\mathrm{s}\delta q + \sqrt{2\kappa}a_\mathrm{in}. \tag{2.17}$$

By assuming the driving laser amplitude $E = |E|\exp(i\varphi)$, where $|E|$ is related to the input laser power P by $|E| = \sqrt{2P\kappa/\hbar\omega_L}$ and φ denotes the phase of the laser field coupling to the optical cavity field, we choose φ to satisfy $\tan(\varphi) = \Delta/\kappa$ so that α_s may be real.

The quadratures play an essential role in studying entanglement because they are used to quantify the correlations between different modes. We define the cavity field quadratures $\delta X = \left(\delta a + \delta a^\dagger\right)/\sqrt{2}$ and $\delta Y = i\left(\delta a^\dagger - \delta a\right)/\sqrt{2}$ as two observables that describe the quantum state of a cavity field mode, which can be measured using homodyne detection techniques.

Accordingly, we define the orthogonal input noise operators $X_\mathrm{in} = (\delta a_\mathrm{in}^\dagger + \delta a_\mathrm{in})/\sqrt{2}$ and $Y_\mathrm{in} = i(\delta a_\mathrm{in}^\dagger - \delta a_\mathrm{in})/\sqrt{2}$, and thereby Eqs. (2.15)-(2.17) can be written as a matrix form as

$$\dot{\mu}(t) = A\mu(t) + n(t). \tag{2.18}$$

Here the components of each matrix are as follows: the transposes of the column vector of con-

tinuous variables fluctuation operators are written as $\mu^T(t) = [\delta q(t), \delta p(t), \delta X(t), \delta Y(t)]$; the transposes of the column vector of noise operators are denoted by

$$n^T(t) = \left[0.5\xi'(t), 0.5\xi(t), \sqrt{2\kappa}X_{\text{in}}(t), \sqrt{2\kappa}Y_{\text{in}}(t)\right]; \tag{2.19}$$

and the coefficient matrix A in terms of system parameters takes the form

$$A = \begin{pmatrix} -0.25\gamma_{\text{m}} & \omega_{\text{m}} & 0 & 0 \\ -\omega_{\text{m}} & -0.25\gamma_{\text{m}} & G & 0 \\ 0 & 0 & -\kappa & \Delta \\ G & 0 & -\Delta & -\kappa \end{pmatrix}, \tag{2.20}$$

where the effective optomechanical coupling is given by $G = \sqrt{2}\alpha_{\text{s}}G_0$.

The solution of Eq. (2.18) can be expressed as

$$\mu(t) = M(t)\mu(t_0) + \int_{t_0}^{t} M(\tau)n(t-\tau)\,d\tau, \tag{2.21}$$

where M is the matrix exponential $M(t) = \exp(\text{A}t)$ and we assume the initial time as $t_0 = 0$. The system is stable if and only if the real parts of all the eigenvalues of the matrix A are negative. The eigenvalue equation $\det|A - \lambda \text{I}_4| = [(0.25\gamma_{\text{m}} + \lambda)^2 + \omega_{\text{m}}^2][(\kappa + \lambda)^2 + \Delta^2] - \omega_{\text{m}}G^2\Delta = 0$, where I_4 denotes the four-dimensional identity matrix, can be reduced to the fourth-order equation $C_0\lambda^4 + C_1\lambda^3 + C_2\lambda^2 + C_3\lambda + C_4$=0. The stability conditions can be derived by applying the Routh-Hurwitz criterion [88] as follows: $C_0 > 0,\ C_1 > 0,\ C_1C_2 - C_0C_3 > 0,\ (C_1C_2 - C_0C_3)C_3 - C_1^2C_4 > 0,\ C_4 > 0$, yielding the following two nontrivial conditions: $(\omega_{\text{m}}^2 + \gamma_{\text{m}}^2/16)(\Delta^2 + \kappa^2) - \omega_{\text{m}}G^2\Delta > 0$ and

$$\begin{aligned} &+ \gamma_{\text{m}}\kappa\left\{\Delta^4 + \Delta^2\left(\frac{\gamma_{\text{m}}^2}{8} + \gamma_{\text{m}}\kappa + 2\kappa^2 - 2\omega_{\text{m}}^2\right) + \frac{1}{256}\left[16\omega_{\text{m}}^2 + (\gamma_{\text{m}} + 4\kappa)^2\right]^2\right\} \\ &+ \omega_{\text{m}}G^2\Delta\left(\frac{\gamma_{\text{m}}}{2} + 2\kappa\right)^2 > 0. \end{aligned} \tag{2.22}$$

The following numerical simulation shows that realistic experimental parameter configurations always meet these stability conditions. When the system is stable, it reaches a unique steady state in the long-time limit $t \to +\infty$ independently of the initial condition.

We set the initial state to a Gaussian one, and the linear dynamics preserve the noise operators ξ', ξ, and a_{in}. Thus, the correlation properties of the system can be completely characterized by its two first moments, of which we are interested in the second one, namely the covariance matrix with elements defined as

$$\begin{aligned} V_{ij} &= \frac{1}{2}\left\langle \mu_i\left(+\infty\right)\mu_j\left(+\infty\right)+\mu_j\left(+\infty\right)\mu_i\left(+\infty\right)\right\rangle \\ &= \sum_{k,l}\int_{t_0}^{+\infty}d\tau\int_{t_0}^{+\infty}d\tau' M_{ik}\left(\tau\right)M_{jl}\left(\tau'\right)\Phi_{kl}\left(\tau-\tau'\right), \end{aligned} \tag{2.23}$$

where $\Phi_{kl}\left(\tau-\tau'\right)=\left\langle n_k\left(\tau\right)n_l\left(\tau'\right)+n_l\left(\tau'\right)n_k\left(\tau\right)\right\rangle/2$ is the matrix of the stationary noise correlation functions. Because the matrix elements are independent of $n\left(t\right)$, we find $\Phi_{kl}\left(\tau-\tau'\right)$ $=D_{kl}\delta\left(\tau-\tau'\right)$, where $D=\text{Diag}\left[\gamma_{\text{m}}\left(2\bar{n}+1\right)/4,\gamma_{\text{m}}\left(2\bar{n}+1\right)/4,\kappa,\kappa\right]$ is a diagonal matrix. According to Eq. (2.23) and the form of $\Phi_{kl}\left(\tau-\tau'\right)$, we find that the expression of the matrix V is equivalent to

$$V=\int_{t_0}^{+\infty}M\left(\tau\right)DM(\tau)^T d\tau, \tag{2.24}$$

which leads to a linear Lyapunov equation with respect to V, i.e., $AV+VA^T=-D$. See Appendix A.6 for a detailed derivation of the Lyapunov equation.

In addition, we can derive a Lyapunov equation satisfied by the high-frequency inverse-resonance Hamiltonian H_{F}^{I} similarly to the form of the high-frequency resonance Hamiltonian H_{F}. Moreover, we show that the analysis and results concerning optomechanical entanglement in the high-frequency inverse-resonance regime are equivalent to those in the high-frequency resonance regime. Therefore, we do not elaborate on it further here.

2.3.3 Optomechanical entanglement

Cavity optomechanical systems naturally exhibit complex entanglement structures and always involve mixed states and continuous variable entanglement, which are affected by dissipation and noise. In this sense, the logarithmic negativity is a powerful tool that can provide valuable insights into the nature of optomechanical entanglement [89], which can be experimentally measured using homodyne detection. Thus, we use the logarithmic negativity E_{N}

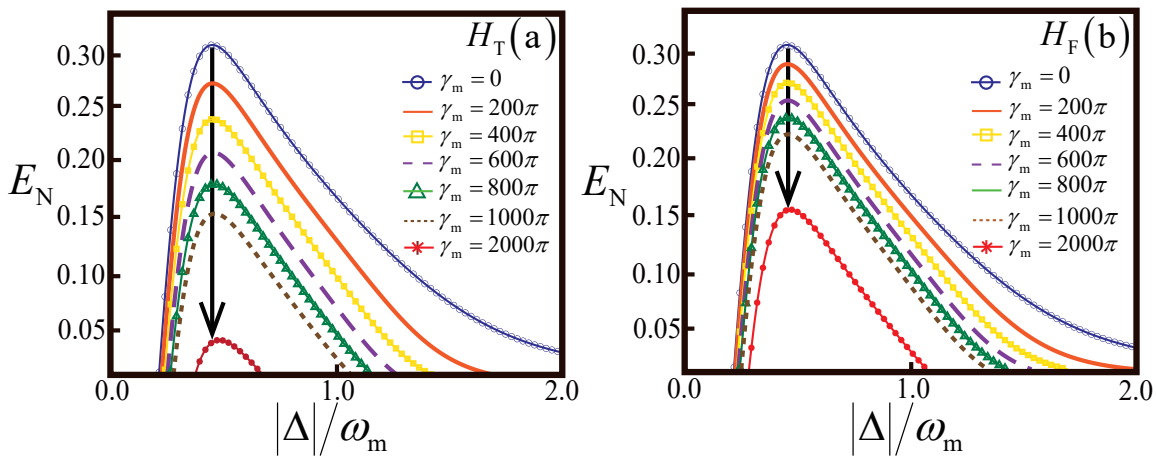

Figure 2.3: Plot of the logarithmic negativity E_{N} as a function of the normalized detuning frequency of the optical field $|\Delta|$ (in units of ω_{m}) for seven values of the mechanical damping rate: $\gamma_{\mathrm{m}} = 0$ (blue circular line), $\gamma_{\mathrm{m}} = 200\pi$Hz (orange solid line), $\gamma_{\mathrm{m}} = 400\pi$Hz (yellow square line), $\gamma_{\mathrm{m}} = 600\pi$Hz (purple dashed line), $\gamma_{\mathrm{m}} = 800\pi$Hz (green triangle line), $\gamma_{\mathrm{m}} = 1000\pi$Hz (brown dotted line), and $\gamma_{\mathrm{m}} = 2000\pi$Hz (red cross line), where (a) and (b) correspond to the original model H_{T} and the filtering model H_{F}, respectively. The length of the black downward-pointing arrows indicates how sensitive optomechanical entanglement is to γ_{m}. The other parameters for (a) and (b) are chosen as follows: the optical cavity of length $L = 1$mm and the drives laser with wavelength $\lambda = 810$nm and power $P = 50$mW. The decay rate of the optical cavity is chosen to be $\kappa = 8.8\pi \times 10^6$Hz, the optical finesse $F = \pi c/L\kappa \approx 3.4 \times 10^4$ with $c = 3\times10^8$m/s, and the driving laser frequency is resonant with the characteristic frequency of the cavity field, $\omega_L = \omega_{\mathrm{c}} = 2\pi c/\lambda$. The mechanical oscillator has the characteristic frequency $\omega_{\mathrm{m}} = 20\pi$MHz, the effective mass $m = 50$ng, and its temperature is $T = 400$mK [46].

to measure optomechanical entanglement between the optical cavity field and the mechanical oscillator. It provides an obvious easy way to compute an upper bound for the distillable optomechanical entanglement [48].

As mentioned in the continuous-variable scenario, the bipartite optomechanical entanglement can be quantified as [86]

$$E_{\mathrm{N}} = \max\left[0, -\ln\left(2\Xi\right)\right], \tag{2.25}$$

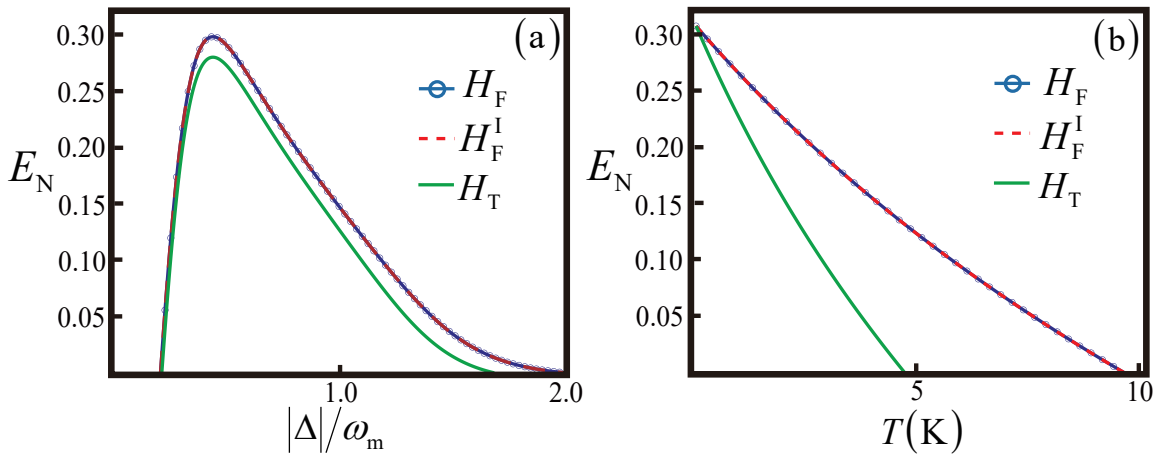

Figure 2.4: Comparing the optomechanical entanglement properties under different mechanisms, the high-frequency resonance of the filtering model $H_{\rm F}$ (blue circular line), the high-frequency inverse-resonance of the filtering model $H_{\rm F}^{\rm I}$ (red dashed line), and the original model $H_{\rm T}$ (green solid line). (a) Plot of the logarithmic negativity $E_{\rm N}$ as a function of the normalized detuning frequency of the optical field $|\Delta|$ (in units of $\omega_{\rm m}$). We set $\gamma_{\rm m} = 200\pi$Hz and $T = 400$mK. (b) Plot of the logarithmic negativity $E_{\rm N}$ versus the mirror temperature T. We set $\gamma_{\rm m} = 200\pi$Hz and $\Delta = 0.5\omega_{\rm m} = 10\pi$MHz. In both panels, the other parameter values are the same as in Fig. 2.3.

where

$$\Xi = \frac{1}{\sqrt{2}}\left\{\Sigma\left(V\right) - \sqrt{\left[\Sigma\left(V\right)\right]^2 - 4\det\left(V\right)}\right\}^{\frac{1}{2}} \tag{2.26}$$

is the lowest symplectic eigenvalue of the partial transpose of the 4×4 steady-state correlation matrix [90]. For simplicity, we denote the 4×4 steady-state correlation matrix in a 2×2 block-matrix form as $V = \left[\left(\Theta,\beta\right),\left(\beta^T,\eta\right)\right]$, and $\Sigma\left(V\right) = \det\left(\Theta\right)+\det\left(\eta\right)-2\det\left(\beta\right)$. We note that a Gaussian state is entangled if and only if $\Xi < 1/2$. This is equivalent to Simon's entanglement criteria for all bipartite Gaussian states [91], which can be written as $4\det\left(V\right) < \Sigma(V) - 1/4$.

We numerically calculated the negativity for cavity optomechanical systems as shown in Figs. 2.3 and 2.4. In our numerical simulation, we utilized the parameter values identical to those outlined in Ref. [46], which agree with the current optomechanical experiments configurations [92–95] and satisfy the stability conditions (2.22). To begin with, we set the initial closed-optomechanical system in the maximum optomechanical entangled state. For simplicity, we assumed that the driving laser frequency ω_L is resonant with the characteristic frequency

ω_c of the cavity field, that is, the laser detuning from the cavity resonance satisfies $\Delta_0 = 0$.

In Fig. 2.3, we compare the sensitivity of the optomechanical entanglement E_N to the mechanical damping rate γ_m for the two optomechanical systems, H_T and H_F. We show a significant enhancement of the robustness of optomechanical entanglement for H_F against γ_m. Specifically, we observe the decrease of E_N due to $\gamma_m = 2000\pi$Hz in Fig. 2.3(b) is approximately half of that in Fig. 2.3(a), which implies that the optomechanical entanglement of the filtering model H_F is almost twice as robust to γ_m as the original model H_T. Additionally, it is worth noting that the presence of optomechanical entanglement is only within a limited range of $|\Delta|$ around $|\Delta| \approx \omega_m$, which means that the frequency resonance between the normalization of the detuning frequency of the optical field $|\Delta|$ and the frequency of the mechanical oscillator ω_m plays a dominant role in the generation of optomechanical entanglement.

We further examine the impact of the resonance effect between the mechanical mode and its thermal reservoir on the properties of optomechanical entanglement. For this purpose, we set $\gamma_m = 200\pi$Hz according to the actual laboratory conditions.

Figure 2.4(a) shows the logarithmic negativity E_N versus the normalized detuning frequency of the optical field $|\Delta|$ (in units of ω_m) for cases models, the high-frequency resonance of the filtering model H_F, the high-frequency inverse-resonance of the filtering model H_F^I, and the original system H_T. It shows that the maximum optomechanical entanglements for H_F and H_F^I are equal to each other while that for H_T is less than it. The results indicate that the resonance effect can safeguard the maximum optomechanical entanglement by filtering out the contributions from a largely detuned part of the degree of freedom, ultimately reducing both the Brownian noise ξ (ξ') and the mechanical dissipation γ_m.

The robustness of the entanglement E_N with respect to the environmental temperature T of the mirror is shown in Fig. 2.4(b). We find that the optomechanical entanglement of the filtering model H_F remains even at temperatures around 10K and is twice the magnitude of the persistent temperature in the original model H_T. In addition, we observe that the high-frequency resonance and the high-frequency inverse-resonance regimes have completely equivalent effects on optomechanical entanglement.

In summary, we have discussed the impact of the high-frequency resonance effect between

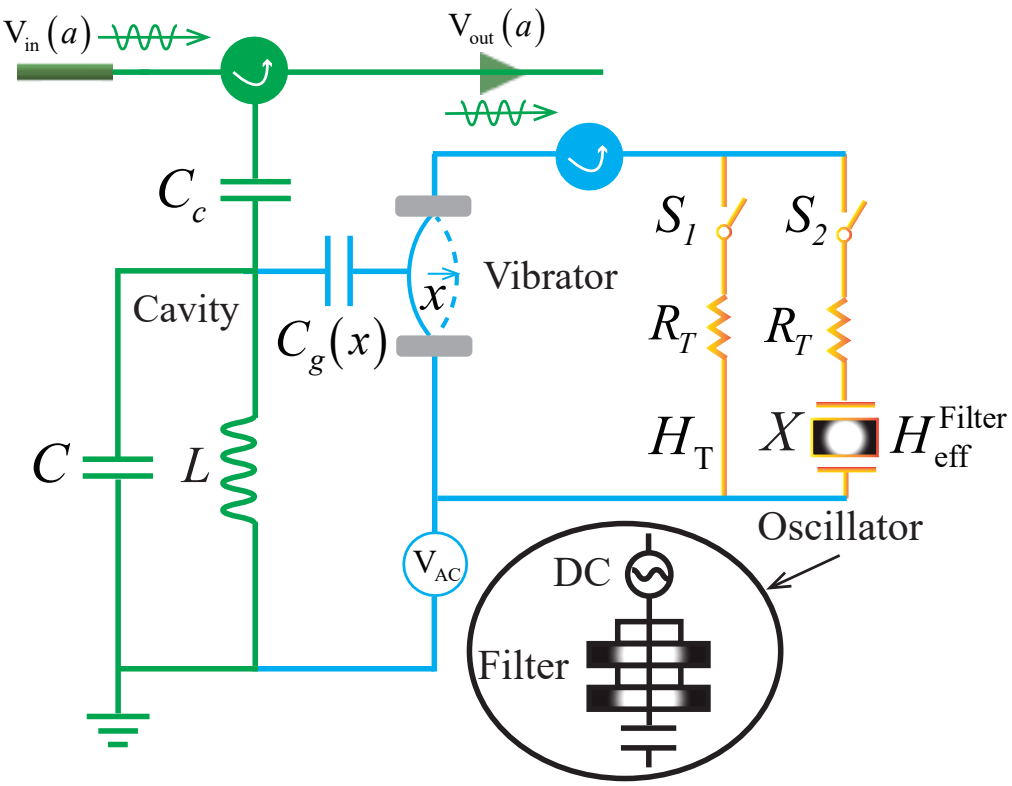

Figure 2.5: A circuit consisting of a resistor, inductor, and capacitor can be used to build an oscillatory filtering model for high-frequency resonance. This experimental setup comprises an on-chip optical cavity (green) coupled with a high-quality-factor nano-mechanical resonator. By turning on the switch S_1 and turning off the switch S_2, the thermistor (orange) will provide a thermal environment that couples with the resonator, corresponding to the original model H_{T}. Conversely, the thermistor and the oscillator (black) will generate a thermal environment with high-frequency oscillation that couples with the resonator, corresponding to the filtering model H_{F}. Direct current, abbreviated as DC, is used for signal frequency readout.

the mechanical oscillator and its thermal reservoir on optomechanical entanglement. We have found that the resonance effect doubles the robustness of optomechanical entanglement to the mechanical dissipation and the mirror temperature. We have achieved the maximum protection of optomechanical entanglement by constructing a filtering model using resonance effects. We have observed numerically that both the high-frequency resonance and the high-frequency inverse-resonance regimes have equivalent effects on optomechanical entanglement.

2.3.4 Experimental implementation

We propose materializing the present theoretical filtering model in a resistor-inductor-capacitor circuit [64,96,97] or superconducting quantum interference device experiments [98]. Here, we focus on the high-frequency resonance region. As shown in Fig. 2.5, we build an oscillatory circuit consisting of a capacitor C, an inductor L, a thermistor R_T, and an oscillator X. We set the normalized detuning frequency of the optical field of the LC circuit to satisfy $|\Delta| = 1/(2\pi\sqrt{LC}) = 20\pi$MHz.

First, the mechanical resonator (blue) and the optical cavity (green) are connected via an inductor. Second, an extensive AC voltage bias $\mathrm{V_{AC}}$ is applied in order to excite the mechanical resonator, represented as a movable capacitance $C_g(x)$. To obtain the maximum optomechanical entanglement, the frequency of the applied voltage should be close to $|\Delta|$, namely $|\Delta| \approx \omega_{\mathrm{m}}$. Next, as the LC circuit oscillates, a current is induced in the thermistor, generating a temperature change due to the Joule heating effect. Therefore, by turning on the switch S_1 and turning off the switch S_2 simultaneously, the mechanical resonator is coupled to a full-frequency thermal reservoir, corresponding to the original model H_{T}. In contrast, the largely detuned part of the degree of freedom can be filtered by applying the oscillator X if we turn off the switch S_1 while turning on the switch S_2. The oscillator X is an electronic circuit component capable of generating a specific frequency signal and can be utilized as a filter to filter out unwanted frequency components selectively. Specifically, when the input signal matches the resonant frequency of the oscillator, it amplifies the input signal and outputs a near-resonant signal, thereby achieving high-frequency oscillatory wave filtering. Thus, the resistor-inductor-capacitor oscillatory circuit can be described by the filtering model H_{F}.

In addition, we need to choose a mechanical resonator with a giant mechanical quality factor to ensure that significant quantum effects are achievable, that is, $Q = \omega_{\mathrm{m}}/\gamma_{\mathrm{m}} = 1/\gamma \gg 1$ corresponding to the weak-coupling limit $\gamma \ll 1$. The remaining parameter values for the simulation of the circuit experiment are the same as in Fig. 2.4(a). Furthermore, we note that with optical interferometry techniques [99, 100], we can observe the resonance response of a mechanical resonator to its thermal environment. The homodyne detection techniques [101, 102] can be used to measure an optomechanical entanglement.

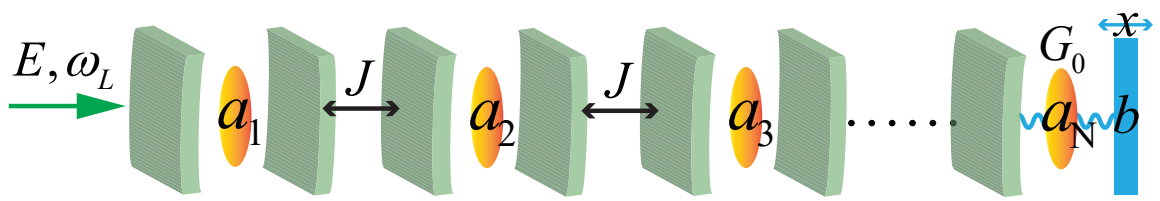

Figure 2.6: Schematic diagram depicting a one-dimensional array of optical cavities coupled via linear hopping between each cavity, with an oscillating end mirror.

It is important to note that experimental studies on open-system dynamics with linear optical setups often use approximated simulations of quantum channels, such as amplitude decay or phase-damping channels [103–106] These simulations rely on the rotating-wave approximation for system-bath interactions and the weak-coupling approximation. Recently, we noted that a study aims to test the difference between channels with and without the rotating-wave approximation by studying the varying dynamics of quantum temporal steering was demonstrated experimentally [107, 108].

2.4 Generalized extension and application

We are now extending the theory of resonance-dominant entanglement to a multi-mode optomechanical system. Specifically, we discuss an optical-cavity array with one oscillating end mirror and investigate optimal optomechanical-entanglement transmission.

As schematically shown in Fig. 2.6, the system comprises an oscillating end mirror coupled to an array of optical cavities. The adjacent optical cavities are linearly coupled with an interaction strength of J [109]. A laser field drives the left end of the optical cavity, while the right end is connected to a vibrating end mirror.

If we consider this system to be in the high-frequency resonance regime, the total Hamiltonian of this open quantum system can be expressed as

$$
\begin{aligned}
H =& + \hbar\Delta_0 a_1^\dagger a_1 + \sum_{j=2}^{N} \omega_{\mathrm{c}_j} a_j^\dagger a_j + \hbar\omega_{\mathrm{m}} b^\dagger b + i\hbar\left(E a_1^\dagger - E^* a_1\right) + \hbar\sum_{j=1}^{N-1} J\left(a_j^\dagger a_{j+1} + a_{j+1}^\dagger a_j\right) \\
&- \hbar\frac{G_0}{\sqrt{2}} a_N^\dagger a_N\left(b^\dagger + b\right) + \hbar\sum_{j=1}^{N}\sum_{k} \omega_{jk}\Gamma_{jk}^\dagger\Gamma_{jk} + \hbar\sum_{j=1}^{N}\sum_{k} g_{jk}\left(\Gamma_{jk}^\dagger a_j + a_j^\dagger\Gamma_{jk}\right) \\
&+ \hbar\sum_{n} \omega_n \Lambda_n^\dagger\Lambda_n - i\hbar\sum_{n}\frac{\ell_n}{2}\left(\Lambda_n^\dagger b - b^\dagger\Lambda_n\right), \qquad (2.27)
\end{aligned}
$$

where $a_j^\dagger$ (a_j) and $\Gamma_{jk}^\dagger$ (Γ_{jk}) are the corresponding creation (annihilation) operators for the jth optical cavity mode and its thermal reservoir modes with frequencies ω_{c_j} and ω_{jk}, respectively, and the coupling strength between them is g_{jk}.

Similarly, nonlinear Langevin equations for the operators of the mechanical and optical modes are given as follows:

$$
\begin{aligned}
\dot{q} &= \omega_{\mathrm{m}} p - \frac{\gamma_{\mathrm{m}}}{4} q + \frac{1}{2}\xi', \\
\dot{p} &= -\omega_{\mathrm{m}} q - \frac{\gamma_{\mathrm{m}}}{4} p + G_0 a_{\mathrm{N}}^\dagger a_{\mathrm{N}} + \frac{1}{2}\xi, \qquad (2.28) \\
\dot{a}_1 &= -\left(\kappa + i\Delta_0\right) a_1 - iJ a_2 + E + \sqrt{2\kappa} a_1^{\mathrm{in}}, \cdots, \\
\dot{a}_j &= -\left(\kappa + i\omega_{\mathrm{c}_j}\right) a_j - iJ\left(a_{j-1} + a_{j+1}\right) + \sqrt{2\kappa} a_j^{\mathrm{in}}, \cdots, \\
\dot{a}_N &= -\left(\kappa + i\omega_{\mathrm{c}_N}\right) a_N - iJ a_{N-1} + iG_0 q a_N + \sqrt{2\kappa} a_N^{\mathrm{in}},
\end{aligned}
$$

where we assume that all optical-cavity fields share the same coupling strength: $g_{jk} = g_k$, i.e., $\kappa_j = \kappa$. As the simplest case, we consider $N = 2$ to study the optomechanical entanglement properties of this system. Similarly, we use the logarithmic negativity to measure the entanglement between two arbitrary bosonic modes in the system. Now, we focus on the numerical evaluation of the bipartite entanglement $E_{\mathrm{N}}^{\mathrm{mc\cdot 1}}$ to show the optimal remote optomechanical entanglement transfer.

In the two-cavity case, we let $E_{\mathrm{N}}^{\mathrm{mc\cdot 1}}$, $E_{\mathrm{N}}^{\mathrm{mc\cdot 2}}$, and $E_{\mathrm{N}}^{\mathrm{cc\cdot 12}}$ denote the logarithmic negativity between the mirror and the cavity 1, the mirror and the cavity 2, and the cavity 1 and the cavity 2, respectively. In Fig. 2.7(a), we plot $E_{\mathrm{N}}^{\mathrm{mc\cdot 1}}$, $E_{\mathrm{N}}^{\mathrm{mc\cdot 2}}$, and $E_{\mathrm{N}}^{\mathrm{cc\cdot 12}}$ as functions of the normalized detuning $|\varpi|$ (in units of ω_{m}) with the other parameters set to $\Delta_0 = 0$, $J = 0.7\omega_{\mathrm{m}}$, and $T = 400\mathrm{mK}$. The normalized detuning $\varpi = \omega_{\mathrm{c}_2} - G_0 Q_{\mathrm{s}}$ depends on the steady-state mean values $Q_{\mathrm{s}} = G_0\alpha_{2\mathrm{s}}^*\alpha_{2\mathrm{s}}/\omega_{\mathrm{m}}$, and $\alpha_{2\mathrm{s}} = -iJ\alpha_{1\mathrm{s}}/\left(\kappa + i\varpi\right)$ with $\alpha_{1\mathrm{s}} = E/\left[\kappa + i\Delta_0 + J^2/\left(\kappa + i\varpi\right)\right]$,

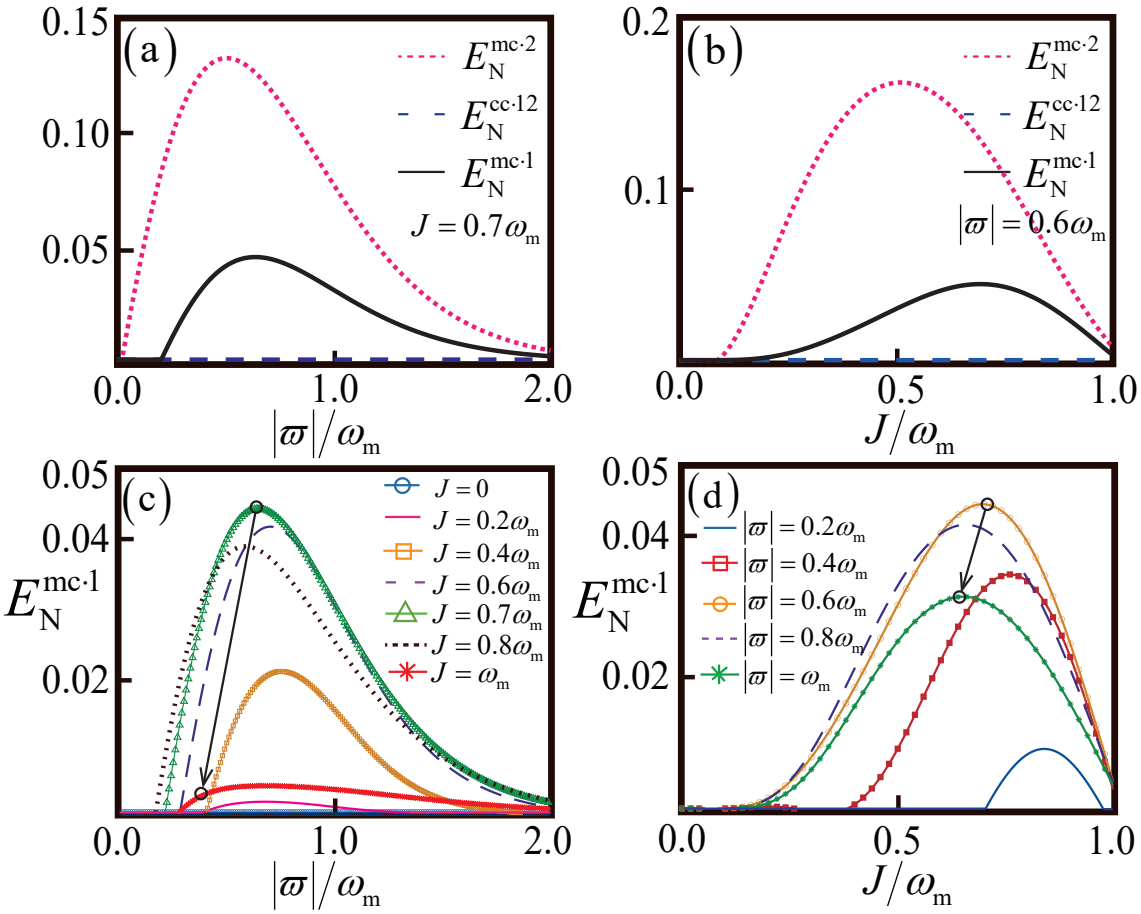

Figure 2.7: The optimal remote optomechanical-entanglement transmission. (a) The negativity entanglements $E_{\rm N}^{\rm mc\cdot 1}$ (pink dotted line), $E_{\rm N}^{\rm mc\cdot 2}$ (black solid line), and $E_{\rm N}^{\rm cc\cdot 12}$ (blue dashed line) as a function of the normalized detuning $|\varpi|$ (in units of $\omega_{\rm m}$) with the other parameters set to $\Delta_0 = 0$ and $J = 0.7\omega_{\rm m}$. (b) The negativity entanglements $E_{\rm N}^{\rm mc\cdot 1}$, $E_{\rm N}^{\rm mc\cdot 2}$, and $E_{\rm N}^{\rm cc\cdot 12}$ versus the linear hopping strength J (in units of $\omega_{\rm m}$) with the other parameters set to $\Delta_0 = 0$ and $|\varpi| = 0.6\omega_{\rm m}$. (c) The negativity entanglements $E_{\rm N}^{\rm mc\cdot 1}$ as a function of $|\varpi|$ (in units of $\omega_{\rm m}$) for different values of the linear hopping rate: $J = 0$ (blue circular line), $J = 0.2\omega_{\rm m}$ (pink solid line), $J = 0.4\omega_{\rm m}$ (orange square line), $J = 0.6\omega_{\rm m}$ (purple dashed line), $J = 0.7\omega_{\rm m}$ (green triangle line), $J = 0.8\omega_{\rm m}$ (brown dotted line), and $J = \omega_{\rm m}$ (red cross line). (d) The negativity entanglements $E_{\rm N}^{\rm mc\cdot 1}$ as a function of J (in units of $\omega_{\rm m}$) for different values of the normalized detuning: $|\varpi| = 0.2\omega_{\rm m}$ (blue solid line), $|\varpi| = 0.4\omega_{\rm m}$ (red square line), $|\varpi| = 0.6\omega_{\rm m}$ (orange circular line), $|\varpi| = 0.8\omega_{\rm m}$ (purple dashed line), and $|\varpi| = \omega_{\rm m}$ (green cross line). The remaining parameter values for all panels are set to be the same as those in Fig. 2.4.

which can be obtained by setting the time derivation to zero in the nonlinear Langevin equation (2.28) for $N = 2$. Our numerical findings show that by tuning the magnitude of ϖ, we are able to achieve long-distance optomechanical-entanglement transfer. As $|\varpi|$ increases approximately from $0.50\omega_{\rm m}$ to $0.65\omega_{\rm m}$, the distant optomechanical entanglement $E_{\rm N}^{\rm mc\cdot 1}$ correspondingly increases at the expense of the decrease of the neighboring optomechanical entanglement $E_{\rm N}^{\rm mc\cdot 2}$, due to the adjacent cavities acting as entanglement transmitters.

In Fig. 2.7(b), we plot $E_{\rm N}^{\rm mc\cdot 1}$, $E_{\rm N}^{\rm mc\cdot 2}$, and $E_{\rm N}^{\rm cc\cdot 12}$ as functions of the linear hopping strength J (in units of $\omega_{\rm m}$) with the other parameters set to $\Delta_0 = 0$, $|\varpi| = 0.6\omega_{\rm m}$, and $T = 400$mK. In a similar analysis, we can also implement distant optomechanical entanglement transfer by adjusting the strength of J approximately from $0.5\omega_{\rm m}$ to $0.75\omega_{\rm m}$. In particular, when $T = 400$mK, we find that the optimal remote optomechanical entanglement transfer occurs around $|\varpi| = 0.6$ and $J = 0.7$ (in units of $\omega_{\rm m}$), and the maximum value of remote entanglement $E_{\rm N}^{\rm mc\cdot 1}$ is approximately evaluated at 0.045; see Fig. 2.7(c)-(d).

2.5 Summary and prospect

In summary, we have demonstrated that resonance effects between a mechanical mode and its thermal environment can protect optomechanical entanglement. Specifically, we have shown that resonance effects nearly double the robustness of the optomechanical entanglement against mechanical dissipation and its environmental temperature. The mechanism of optomechanical-entanglement protection involves the elimination of degrees of freedom associated with significant detuning between the mechanical mode and its thermal reservoirs, thereby counteracting the decoherence. We have revealed that this approach is particularly effective when both near-resonant and weak-coupling conditions are simultaneously satisfied between a mechanical mode and its environment. We have also proposed a feasible experimental implementation for the filtering model to observe these phenomena. Furthermore, we extended this theory to an optical cavity array with one oscillating end mirror and investigated optimal optomechanical entanglement transfer. This study represents a significant advancement in the application of resonance effects for protecting quantum systems against decoherence, thereby opening up new possibilities for large-scale quantum information processing and the construction of quantum networks.

In addition, extending the resonance-dominant entanglement theory to non-Markovian and non-Hermitian optomechanical systems is also challenging and expected to be impactful. Specifically, we ensure that studying non-Markovian effects [110–114], exceptional points [115], parity-time symmetry [116], and anti-parity-time symmetry [117] on optomechanical entanglement is exciting. In particular, we are interested in future investigations of the optomechanical entanglement properties between resonance states [118, 119] in non-Hermitian systems. This work aims to develop an innovative approach for protecting continuous variable entanglement.

Appendix A

Appendix for Chapter 2

A.1 Derivation of the Hamiltonian (2.1)

Here, we show the origin of the total Hamiltonian (2.1) [8,64]. The total Hamiltonian (2.1) of this field reservoir consists of two parts, the system (2.2) and the environment (2.3). Therefore, to obtain Eq. (2.1), we need to demonstrate the specific origins of Eqs. (2.2) and (2.3) separately.

To begin with, we show the origin of the system Hamiltonian (2.2). As usual, for an optomechanical system driven by an optical laser, the Hamiltonian of the composite system can be written as

$$H_{\mathrm{S}}^{0}=\hbar\omega_{\mathrm{c}}a^{\dagger}a+\frac{p'^{2}}{2m}+\frac{1}{2}m(\omega_{\mathrm{m}}q')^{2}-\hbar Ga^{\dagger}aq'+i\hbar\left(Ee^{-i\omega_{0}t}a^{\dagger}-E^{*}e^{i\omega_{0}t}a\right), \qquad \text{(A-1)}$$

where a monochromatic field drives the optical mode with the driving frequency ω_0, and the complex amplitude of the driving laser is denoted by E. The optical frequency shift per displacement is given by $G=-\partial\omega_{\mathrm{c}}\left(x\right)/\partial x=\omega_{\mathrm{c}}/L$. To make the Hamiltonian independent of time, we then move to the rotating frame of the frequency, which changes Eq. (A-1) to the

following:

$$
\begin{aligned}
H_{\mathrm{S}}' &= U\left(t\right) H_{\mathrm{S}}^{0}\left(t\right) U^{\dagger}\left(t\right) - iU\left(t\right)\dot{U}^{\dagger}\left(t\right) \\
&= \hbar\Delta_0 a^{\dagger}a + \frac{p'^2}{2m} + \frac{1}{2}m(\omega_{\mathrm{m}}q')^2 - \hbar G a^{\dagger}aq' + i\hbar\left(Ea^{\dagger} - E^{*}a\right), \qquad \text{(A-2)}
\end{aligned}
$$

where we used the unitary transformation of the form $U\left(t\right) = \exp\left(i\omega_0 a^{\dagger}at\right)$ and $\Delta_0 = \omega_{\mathrm{c}} - \omega_0$ denotes the detuning of the cavity characteristic frequency ω_{c} of the optical cavity from the driving laser frequency ω_0.

We make the position and momentum operators dimensionless by defining the zero-point fluctuation amplitude of the mechanical oscillator as $X_{\mathrm{ZPF}} = \sqrt{\hbar/2m\omega_{\mathrm{m}}}$. Then, we define the dimensionless position operator q and momentum operator p as follows:

$$
q = \frac{q'}{\sqrt{2}X_{\mathrm{ZPF}}} = \frac{1}{\sqrt{2}}\left(b^{\dagger} + b\right), \quad p = \frac{p'}{\sqrt{2}m\omega_{\mathrm{m}}X_{\mathrm{ZPF}}} = \frac{i}{\sqrt{2}}\left(b^{\dagger} - b\right). \qquad \text{(A-3)}
$$

Substituting Eq. (A-3) into Eq. (A-2), we arrive at

$$
\begin{aligned}
H_{\mathrm{S}} &= \hbar\Delta_0 a^{\dagger}a + \frac{\hbar}{2}\omega_{\mathrm{m}}\left(p^2 + q^2\right) - \hbar G_0 a^{\dagger}aq + i\hbar\left(Ea^{\dagger} - E^{*}a\right) \\
&= \hbar\Delta_0 a^{\dagger}a + \hbar\omega_{\mathrm{m}}b^{\dagger}b - \hbar G_0 a^{\dagger}a\frac{\left(b^{\dagger} + b\right)}{\sqrt{2}} + i\hbar\left(Ea^{\dagger} - E^{*}a\right), \qquad \text{(A-4)}
\end{aligned}
$$

where $G_0 = \sqrt{2}GX_{\mathrm{ZPF}} = \omega_{\mathrm{c}}\sqrt{\hbar/m\omega_{\mathrm{m}}}/L$ is the vacuum optomechanical coupling strength, expressed as a frequency. It quantifies the interaction between a single phonon and a single photon. This produces Eq. (2.2) in the main text.

Next, we give the origin of the environment Hamiltonian (2.3) for the first time. As is well known from the Bose-Einstein statistics, a heat bath associated with a boson system can be considered as an assembly of harmonic oscillators. This type of heat bath can serve as a model for various physical systems, such as elastic solids (mechanical reservoirs) and electromagnetic fields (optical reservoirs).

Firstly, since in the optomechanical system, both the photons in the optical cavity and the phonons in the mechanical oscillator obey the Bose-Einstein statistics, the free part of the en-

vironment can be written in the simple form

$$H_{\mathrm{E}}^{0}=\frac{1}{2}\sum_{k}\left[\frac{1}{m_{k}^{\mathrm{c}}}(\tilde{p}_{k}^{\mathrm{c}})^{2}+\Theta_{k}^{\mathrm{c}}(\tilde{q}_{k}^{\mathrm{c}})^{2}\right]+\frac{1}{2}\sum_{n}\left[\frac{1}{m_{n}^{\mathrm{m}}}(\tilde{p}_{n}^{\mathrm{m}})^{2}+\Theta_{n}^{\mathrm{m}}(\tilde{q}_{n}^{\mathrm{m}})^{2}\right], \tag{A-5}$$

where m_k^{c} and m_n^{m} correspond to the effective mass of the kth optical reservoir and nth mechanical reservoir, respectively. The momentum and position operators corresponding to the kth optical reservoir and the nth mechanical reservoir are denoted by $\tilde{p}_k^{\mathrm{c}}$ $\tilde{p}_n^{\mathrm{m}}$ and $\tilde{q}_k^{\mathrm{c}}$ $\tilde{q}_n^{\mathrm{m}}$, respectively. We set $\Theta_k^{\mathrm{c}}=m_k^{\mathrm{c}}(\omega_k)^2$ and $\Theta_n^{\mathrm{m}}=m_n^{\mathrm{m}}(\omega_n)^2$ as the optical and mechanical potential-force constants. The harmonic-oscillator reservoirs have closely spaced frequencies corresponding to photons and phonons, denoted by ω_k and ω_n, respectively. Through the process of removing the dimensions from the operators, we define the dimensionless momentum operators p_k^{c} and p_n^{m} as well as position operators q_k^{c} and q_n^{m} as follows:

$$p_{k}^{\mathrm{c}}=\sqrt{\frac{\omega_{k}}{\Theta_{k}^{\mathrm{c}}\hbar}}\tilde{p}_{k}^{\mathrm{c}}=\sqrt{\frac{1}{m_{k}^{\mathrm{c}}\omega_{k}\hbar}}\tilde{p}_{k}^{\mathrm{c}},\qquad q_{k}^{\mathrm{c}}=\sqrt{\frac{\Theta_{k}^{\mathrm{c}}}{\omega_{k}\hbar}}\tilde{q}_{k}^{\mathrm{c}}=\sqrt{\frac{\omega_{k}}{\hbar}}\tilde{p}_{k}^{\mathrm{c}}, \tag{A-6}$$

$$p_{n}^{\mathrm{m}}=\sqrt{\frac{\omega_{n}}{\Theta_{n}^{\mathrm{m}}\hbar}}\tilde{p}_{n}^{\mathrm{m}}=\sqrt{\frac{1}{m_{n}^{\mathrm{m}}\omega_{n}\hbar}}\tilde{p}_{n}^{\mathrm{m}},\quad q_{n}^{\mathrm{m}}=\sqrt{\frac{\Theta_{n}^{\mathrm{m}}}{\omega_{n}\hbar}}\tilde{q}_{n}^{\mathrm{m}}=\sqrt{\frac{\omega_{n}}{\hbar}}\tilde{p}_{n}^{\mathrm{m}}. \tag{A-7}$$

Substituting Eqs. (A-6) and (A-7) into Eq. (A-5), we have

$$H_{\mathrm{E}}^{\prime}=\frac{\hbar}{2}\sum_{k}\omega_{k}\left[(p_{k}^{\mathrm{c}})^{2}+(q_{k}^{\mathrm{c}})^{2}\right]+\frac{\hbar}{2}\sum_{n}\omega_{n}\left[(p_{n}^{\mathrm{m}})^{2}+(q_{n}^{\mathrm{m}})^{2}\right], \tag{A-8}$$

Secondly, we consider the coupling between the system and the environment. The Hamiltonian of a system can be left arbitrary, such as an atom, as in quantum optics, or a macroscopic LC-circuit. In our case, we treat the optomechanical system as a perturbation to the baths, by writing

$$\begin{aligned}H_{\mathrm{E}}^{\prime\prime}&=+\frac{\hbar}{2}\sum_{k}\omega_{k}\left[(p_{k}^{\mathrm{c}})^{2}+(q_{k}^{\mathrm{c}}+\varepsilon_{k}^{\mathrm{c}}q_{\mathrm{c}})^{2}\right]+\frac{\hbar}{2}\sum_{n}\omega_{n}\left[(p_{n}^{\mathrm{m}}-\chi_{n}^{\mathrm{m}}q_{\mathrm{m}})^{2}+(q_{n}^{\mathrm{m}})^{2}\right]\\&=+\frac{\hbar}{2}\sum_{k}\omega_{k}\left[(p_{k}^{\mathrm{c}})^{2}+(q_{k}^{\mathrm{c}})^{2}\right]+\frac{\hbar}{2}\sum_{k}\omega_{k}(\varepsilon_{k}^{\mathrm{c}}q_{\mathrm{c}})^{2}+\hbar\sum_{k}\omega_{k}\varepsilon_{k}^{\mathrm{c}}q_{k}^{\mathrm{c}}q_{\mathrm{c}}\\&\quad+\frac{\hbar}{2}\sum_{n}\omega_{n}\left[(p_{n}^{\mathrm{m}})^{2}+(q_{n}^{\mathrm{m}})^{2}\right]+\frac{\hbar}{2}\sum_{n}\omega_{n}(\chi_{n}^{\mathrm{m}}q_{\mathrm{m}})^{2}-\hbar\sum_{n}\omega_{n}\chi_{n}^{\mathrm{m}}p_{n}^{\mathrm{m}}q_{\mathrm{m}},\end{aligned} \tag{A-9}$$

or

$$\begin{aligned}\tilde{H}''_{\mathrm{E}} &= +\frac{\hbar}{2}\sum_{k}\omega_k\left[(p_k^{\mathrm{c}}+\varepsilon_k^{\mathrm{c}}p_{\mathrm{c}})^2+(q_k^{\mathrm{c}})^2\right]+\frac{\hbar}{2}\sum_{\mathrm{n}}\omega_n\left[(p_n^{\mathrm{m}}-\chi_n^{\mathrm{m}}q_{\mathrm{m}})^2+(q_n^{\mathrm{m}})^2\right]\\ &= +\frac{\hbar}{2}\sum_{\mathrm{k}}\omega_k\left[(p_k^{\mathrm{c}})^2+(q_k^{\mathrm{c}})^2\right]+\frac{\hbar}{2}\sum_{k}\omega_k(\varepsilon_k^{\mathrm{c}}p_{\mathrm{c}})^2+\hbar\sum_{k}\omega_k\varepsilon_k^{\mathrm{c}}p_k^{\mathrm{c}}p_{\mathrm{c}}\\ &\quad+\frac{\hbar}{2}\sum_{n}\omega_n\left[(p_n^{\mathrm{m}})^2+(q_n^{\mathrm{m}})^2\right]+\frac{\hbar}{2}\sum_{n}\omega_n(\chi_n^{\mathrm{m}}q_{\mathrm{m}})^2-\hbar\sum_{n}\omega_n\chi_n^{\mathrm{m}}p_n^{\mathrm{m}}q_{\mathrm{m}}.\end{aligned}\tag{A-10}$$

The orthogonal relationship for the dimensionless position and momentum operators of the system and the environment read:

$$q_{\mathrm{c}}=\frac{1}{\sqrt{2}}\left(a^\dagger+a\right),p_{\mathrm{c}}=\frac{i}{\sqrt{2}}\left(a^\dagger-a\right);q_k^{\mathrm{c}}=\frac{1}{\sqrt{2}}\left(\Gamma_k^\dagger+\Gamma_k\right),p_k^{\mathrm{c}}=\frac{i}{\sqrt{2}}\left(\Gamma_k^\dagger-\Gamma_k\right);\tag{A-11}$$

$$q_{\mathrm{m}}=\frac{1}{\sqrt{2}}\left(b^\dagger+b\right),p_{\mathrm{c}}=\frac{i}{\sqrt{2}}\left(b^\dagger-b\right);q_n^{\mathrm{m}}=\frac{1}{\sqrt{2}}\left(\Lambda_n^\dagger+\Lambda_n\right),p_n^{\mathrm{m}}=\frac{i}{\sqrt{2}}\left(\Lambda_n^\dagger-\Lambda_n\right).\tag{A-12}$$

By substituting Eqs. (A-11) and (A-12) into the Eqs. (A-9) and (A-10), absorbing terms only of the system operators $\hbar\sum_{\mathrm{k}}\omega_k(\varepsilon_k^{\mathrm{c}}p_{\mathrm{c}})^2/2$, $\hbar\sum_k\omega_k(\varepsilon_k^{\mathrm{c}}q_{\mathrm{c}})^2/2$, and $\hbar\sum_n\omega_n(\chi_n^{\mathrm{m}}q_{\mathrm{m}})^2/2$ into the system Hamiltonian, and further neglecting these higher-order perturbations quantities containing $(\varepsilon_k^{\mathrm{c}})^2$ and $(\chi_n^{\mathrm{m}})^2$, we obtain

$$\begin{aligned}\tilde{H}''_{\mathrm{E}}\mapsto H_{\mathrm{E}}^{q_{\mathrm{c}}} &= +\hbar\sum_k\omega_k\Gamma_k^\dagger\Gamma_k+\hbar\sum_k g_k\left(\Gamma_k^\dagger a^\dagger+\Gamma_k a\right)+\hbar\sum_k g_k\left(\Gamma_k^\dagger a+\Gamma_k a^\dagger\right)\\ &\quad+\hbar\sum_n\omega_n\Lambda_n^\dagger\Lambda_n-i\hbar\sum_n\frac{\ell_n}{2}\left(\Lambda_n^\dagger-\Lambda_n\right)\left(b^\dagger+b\right),\end{aligned}\tag{A-13}$$

$$\begin{aligned}\tilde{H}''_{\mathrm{E}}\mapsto H_{\mathrm{E}}^{p_{\mathrm{c}}} &= +\hbar\sum_k\omega_k\Gamma_k^\dagger\Gamma_k-\hbar\sum_k g_k\left(\Gamma_k^\dagger a^\dagger+\Gamma_k a\right)+\hbar\sum_k g_k\left(\Gamma_k^\dagger a+\Gamma_k a^\dagger\right)\\ &\quad+\hbar\sum_n\omega_n\Lambda_n^\dagger\Lambda_n-i\hbar\sum_n\frac{\ell_n}{2}\left(\Lambda_n^\dagger-\Lambda_n\right)\left(b^\dagger+b\right),\end{aligned}\tag{A-14}$$

where we set $g_k=\varepsilon_k^{\mathrm{c}}\omega_k/2$ and $\ell_n=\chi_n^m\omega_n$. The real numbers g_k and ℓ_n represent the coupling strengths between the subsystem and the nth reservoir mode, respectively. Finally, we apply the rotating-wave approximation and neglect the counter-rotating terms $\Gamma_k^\dagger a^\dagger$ and $\Gamma_k a$ in Eqs. (A-13) and (A-14), yielding $H_{\mathrm{E}}^{q_{\mathrm{c}}}\approx\tilde{H}_{\mathrm{E}}^{q_{\mathrm{c}}}=H_{\mathrm{E}}=\tilde{H}_{\mathrm{E}}^{p_{\mathrm{c}}}\approx H_{\mathrm{E}}^{p_{\mathrm{c}}}$, where $\tilde{H}_{\mathrm{E}}^{q_{\mathrm{c}}}$ and $\tilde{H}_{\mathrm{E}}^{q_{\mathrm{c}}}$ represent the Hamiltonian after the rotating-wave approximation. This process produces Eq. (2.3) in the Chapter 2.

In conclusion, we have physically revealed that photon and phonon perturbations interact

with the reservoirs differently. The coupling between photons and the bosonic reservoirs results in the potential energy of the bath depending on the deviation of $q_{\rm c}$ from all the $q_k^{\rm c}$, while the kinetic energy of the bath depends on the derivation of $p_{\rm c}$ with respect to all $p_k^{\rm c}$ as well. In other words, it is as if each coordinate $q_k^{\rm c}$ or $p_k^{\rm c}$ is harmonically bound to $q_{\rm c}$ or $p_{\rm c}$, respectively. In contrast, the coupling between phonons and the bosonic reservoirs makes the potential energy of the bath depending on the deviation of $q_{\rm m}$ from all the $p_n^{\rm m}$. The kinetic energy of the bath depends on the derivation of $p_{\rm m}$ with respect to all $q_n^{\rm m}$ as well. In other words, it is as if each coordinate $q_n^{\rm m}$ or $p_n^{\rm m}$ is harmonically bound to $p_{\rm m}$ or $q_{\rm m}$, respectively. In addition, we point out that this difference between perturbations of photons and phonons on the bosonic reservoirs also results in the fact that in the rotating-wave approximation, neglecting the rotating-wave terms $\Gamma_k^\dagger a^\dagger$ and $\Gamma_k a$ in the coupling between photons and the electromagnetic field leads to the simplification of $\sum_k \omega_k[(p_k^{\rm c}+\varepsilon_k^{\rm c}p_{\rm c})^2+(q_k^{\rm c})^2] \approx \sum_k \omega_k[(p_k^{\rm c})^2+(q_k^{\rm c}+\varepsilon_k^{\rm c}q_{\rm c})^2]$, while neglecting the counter-rotating terms $\Lambda_n^\dagger b$ and $\Lambda_n b^\dagger$ in the coupling between phonons and elastic solid simplifies $\sum_n \omega_n[(p_n^{\rm m}-\chi_n^{\rm m}q_{\rm m})^2+(q_n^{\rm m})^2] \approx \sum_n \omega_n[(p_n^{\rm m})^2+(q_n^{\rm m}-\chi_n^{\rm m}p_{\rm m})^2]$.

A.2 Details of the derivation of Eqs. (2.4)-(2.6)

In this Appendix, we derive the nonlinear Langevin equations that the total Hamiltonian $H_{\rm T}$ in Eq. (2.1) satisfies. To begin with, let us derive the nonlinear Langevin equations satisfied by the optical cavity field. The Heisenberg equations of motion for the operator a of the optical cavity field and its corresponding reservoir operators Γ_k are given by

$$\dot{a}=\frac{1}{i\hbar}\left[a,H_{\rm T}\right]=-i\Delta_0 a+iG_0 a\frac{\left(b^\dagger+b\right)}{\sqrt{2}}+E-i\sum_k g_k\Gamma_k, \tag{A-15}$$

$$\dot{\Gamma}_k=\frac{1}{i\hbar}\left[\Gamma_k,H_{\rm T}\right]=-i\omega_k\Gamma_k-ig_k a. \tag{A-16}$$

We are interested in a closed equation for a. Equation (A-16) for Γ_k can be formally integrated to yield

$$\Gamma_k\left(t\right)=\Gamma_k\left(t_0\right)e^{-i\omega_k(t-t_0)}-ig_k\int_{t_0}^{t}a\left(\tau\right)e^{-i\omega_k(t-\tau)}d\tau. \tag{A-17}$$

Here the first term describes the free evolution of the reservoir modes, whereas the second term arises from their interaction with the optical cavity field. We eliminate Γ_k by substituting Eq. (A-17) into Eq. (A-15), finding

$$\dot{a} = -i\Delta_0 a + iG_0 a\frac{\left(b^\dagger + b\right)}{\sqrt{2}} + E - \sum_k \left(g_k\right)^2 \int_{t_0}^{t} a\left(\tau\right) e^{-i\omega_k(t-\tau)} d\tau + f_a\left(t\right) \tag{A-18}$$

with $f_a\left(t\right) = -i\sum_k g_k \Gamma_k\left(t_0\right)\exp\left[-i\omega_k\left(t-t_0\right)\right]$. In Eq. (A-18), we see that the evolution of the system operator depends on the fluctuations in the reservoir.

To proceed, we introduce approximations. Following the Weisskopf-Wigner approximation [17], we replace the summation over k in Eq. (A-18) with an integral term, thereby transitioning from a discrete distribution of modes to a continuous one, $\sum_k \mapsto \left(L/2\pi\right)^3 \int d^3k$, where L is the length of the sides of the assumed cubic cavity with no specific boundaries, and $\vec{\mathrm{k}} \equiv \left(k_x, k_y, k_z\right)$ is the wave vector. The density of modes between the frequencies ω and $\omega + d\omega$ can be obtained by transferring from the Cartesian coordinate to the polar coordinate as in $\vec{\mathrm{k}} \equiv \left(k_x, k_y, k_z\right) \mapsto \left[k\sin\left(\theta\right)\cos\left(\phi\right), k\sin\left(\theta\right)\sin\left(\phi\right), k\cos\left(\theta\right)\right]$. The corresponding volume element in the $\vec{\mathrm{k}}$ space is $d^3k = k^2\sin\left(\theta\right)dkd\theta d\phi = \left(\omega^2/c^3\right)\sin\left(\theta\right)d\omega d\theta d\phi$. The total number of modes N_a in the range between ω and $\omega + d\omega$ is given by $dN_a = \left(L/2\pi c\right)^3\omega^2 d\omega\int_0^\pi \sin\left(\theta\right)d\theta\int_0^{2\pi} d\phi = \left(L^3\omega^2/2\pi^2c^3\right)d\omega$. A mode density parameter at frequency ω is therefore given by $D_a\left(\omega\right) = dN_a\left(\omega\right)/d\omega = L^3\omega^2/2\pi^2c^3$. We then approximate this spectrum by a continuous spectrum. Thus, the summation in Eq. (A-18) can be written as

$$\dot{a} = -i\Delta_0 a + iG_0 a\frac{\left(b^\dagger + b\right)}{\sqrt{2}} + E - \int_{t_0}^{t}\int_0^{+\infty} g^2\left(\omega\right)D_a\left(\omega\right)e^{-i\omega(t-\tau)}a\left(\tau\right)d\omega d\tau + f_a\left(t\right), \tag{A-19}$$

where $g\left(\omega\right) = g_k = g\left[\mathrm{k}\left(\omega\right)\right]$ is the coupling constant evaluated at $\mathrm{k} = \omega/c$. Considering an ideal situation, we assume for simplicity that $\left[g\left(\omega\right)\right]^2 D_a\left(\omega\right) = \kappa/\pi > 0$ is constant, so that Eq. (A-19) is reduced to a simple first-order differential equation [8]:

$$\dot{a} = -i\Delta_0 a + iG_0 a\frac{\left(b^\dagger + b\right)}{\sqrt{2}} + E - \frac{\kappa}{\pi}\int_{t_0}^{t+0^+}\int_0^{+\infty} e^{-i\omega(t-\tau)}a\left(\tau\right)d\omega d\tau + f_a\left(t\right). \tag{A-20}$$

Using the relations

$$\int_0^{+\infty} e^{-i\omega(t-\tau)}d\omega = \pi\delta\left(t-\tau\right), \tag{A-21}$$

we arrive at Eq. (2.6) in the main text:

$$\dot{a} = -\left(\kappa + i\Delta_0\right) a + iG_0 a \frac{\left(b^\dagger + b\right)}{\sqrt{2}} + E + \sqrt{2\kappa} a_{\text{in}} \tag{A-22}$$

with

$$a_{\text{in}}\left(t\right) = \frac{f_a\left(t\right)}{\sqrt{2\kappa}} = \frac{-i}{\sqrt{2\pi}} \sum_k g_k \Gamma\left(t_0\right) e^{-i\omega_k\left(t-t_0\right)}, \tag{A-23}$$

where $a_{\text{in}}\left(t\right)$ is a noise operator which depends upon the environment operators $\Gamma\left(t_0\right)$ at the initial time and κ is the decay rate of the optical cavity field, which depends on the coupling strength g_k of the optical cavity field and its corresponding reservoirs. We have $q = \left(b^\dagger + b\right)/\sqrt{2}$ (quadrature definition), and thus we obtain

$$\dot{a} = -\left(\kappa + i\Delta_0\right) a + iG_0 a q + E + \sqrt{2\kappa} a_{\text{in}}. \tag{A-24}$$

Similarly, the Heisenberg equations of motion for the mechanical operator b and it is corresponding reservoir operators Λ_n are given by

$$\dot{b} = \frac{1}{i\hbar}\left[b, H_{\text{T}}\right] = -i\omega_{\text{m}} b + i\frac{G_0}{\sqrt{2}} a^\dagger a - \frac{1}{2}\sum_n \ell_n \left(\Lambda_n^\dagger - \Lambda_n\right) \tag{A-25}$$

$$\dot{b}^\dagger = \frac{1}{i\hbar}\left[b^\dagger, H_{\text{T}}\right] = i\omega_{\text{m}} b^\dagger - i\frac{G_0}{\sqrt{2}} a^\dagger a + \frac{1}{2}\sum_n \ell_n \left(\Lambda_n^\dagger - \Lambda_n\right) \tag{A-26}$$

$$\dot{\Lambda}_n = \frac{1}{i\hbar}\left[\Lambda_n, H_{\text{T}}\right] = -i\omega_n \Lambda_n - \ell_n \frac{\left(b^\dagger + b\right)}{2} \tag{A-27}$$

$$\dot{\Lambda}_n^\dagger = \frac{1}{i\hbar}\left[\Lambda_n^\dagger, H_{\text{T}}\right] = i\omega_n \Lambda_n - \ell_n \frac{\left(b^\dagger + b\right)}{2}. \tag{A-28}$$

Since we have the orthogonal relationship $q = \left(b^\dagger + b\right)/\sqrt{2}$ and $p = i\left(b^\dagger - b\right)/\sqrt{2}$, where p and q are the dimensionless position and momentum operators of the mirror that satisfy the commutation relation $[q, p] = i$. The derivatives of q and p with respect to time read

$$\dot{q} = \frac{1}{\sqrt{2}}\left(\dot{b}^\dagger + \dot{b}\right) = \omega_{\text{m}} p, \tag{A-1}$$

$$\dot{p} = \frac{i}{\sqrt{2}}\left(\dot{b}^\dagger - \dot{b}\right) = -\omega_{\text{m}} q + G_0 a^\dagger a + i\sum_n \ell_n \frac{\left(\Lambda_n^\dagger - \Lambda_n\right)}{\sqrt{2}}. \tag{A-2}$$

Equation (A-1) corresponds to Eq. (2.4) in the main text.

We now focus on a closed equation for p. Equations (A-27) and (A-28) for Λ_{n} and $\Lambda_{\mathrm{n}}^{\dagger}$ can be formally integrated to yield

$$\Lambda_n(t) = \Lambda_n(t_0)\, e^{-i\omega_n(t-t_0)} - \frac{1}{2}\ell_n \int_{t_0}^{t} \left[b^{\dagger}(\tau) + b(\tau)\right] e^{-i\omega_{\mathrm{n}}(t-\tau)} d\tau, \tag{A-3}$$

$$\Lambda_n^{\dagger}(t) = \Lambda_n^{\dagger}(t_0)\, e^{i\omega_n(t-t_0)} - \frac{1}{2}\ell_n \int_{t_0}^{t} \left[b^{\dagger}(\tau) + b(\tau)\right] e^{i\omega_n(t-\tau)} d\tau. \tag{A-4}$$

We then eliminate the reservoir operators Λ_n and $\Lambda_n^{\dagger}$ by substituting Eqs. (A-3) and (A-4) into Eq. (A-2), and thereby obtain

$$\dot{p} = -\omega_{\mathrm{m}} q + G_0 a^{\dagger} a + \Theta + \xi, \tag{A-5}$$

where

$$\xi(t) = \frac{i}{\sqrt{2}} \sum_n \ell_n \left[\Lambda_n^{\dagger}(t_0)\, e^{i\omega_n(t-t_0)} - \Lambda_n(t_0)\, e^{-i\omega_n(t-t_0)}\right] \tag{A-6}$$

and

$$\Theta(t) = \sum_n (\ell_n)^2 \int_{t_0}^{t} q(\tau) \sin\left[\omega_n(t-\tau)\right] d\tau. \tag{A-7}$$

Equation (A-6) is the same as Eq. (2.8) in the main text [68].

We then integrate Eq. (A-7) by parts and obtain

$$\Theta(t) = \sum_n \frac{(\ell_n)^2}{\omega_n} \left\{q(t) \cos\left[\omega_n(t-t_0)\right]\right\}_{t_0}^{t} - \sum_n \frac{(\ell_n)^2}{\omega_n} \int_{t_0}^{t} \dot{q}(\tau) \cos\left[\omega_n(t-\tau)\right] d\tau. \tag{A-8}$$

The integrand function $\varsigma(t) = \sum_n \left[(\ell_n)^2 \cos(\omega_n t)\right]/\omega_n$ can be seen to have the form of a memory kernel since it makes the equation of motion at time t depend on the values of $\dot{q}(t)$ for the previous time. Within the Born-Markov approximation [18], we assume that $\varsigma(t)$ is a rapidly decaying function and that the system has a short memory. More precisely, if $\varsigma(t)$ goes to zero in a time scale that is much less than the time over which $\dot{q}(t)$ changes, then we can replace $\dot{q}(\tau)$ by $\dot{q}(t)$. For t not close to the initial time t_0, we can drop the first term in

Eq. (A-8). Thus, Eq. (A-8) reads

$$\Theta(t) \approx -\sum_n \frac{(\ell_n)^2}{\omega_n} \int_{t_0}^{t} \dot{q}(t) \cos\left[\omega_n (t-\tau)\right] d\tau. \tag{A-9}$$

Similarly to the optical cavity mode a, using the Weisskopf-Winger approximation, we consider the spectrum to be given by the normal modes of a large scale, $L \to +\infty$. The difference between phonons and photons is that $g_k = g\left[\mathrm{k}(\omega)\right] = g(\omega)$ is the coupling constant evaluated at $\omega \propto \mathrm{k}^2$ instead of $\mathrm{k} = \omega/c$. We then approximate this spectrum by a continuous spectrum. Thus, the summation in Eq. (A-9) can be written as

$$\Theta(t) \approx -\int_0^{+\infty} \int_{t_0}^{t} d\omega d\tau \frac{\left[\ell(\omega)\right]^2}{\omega} \dot{q}(t) \cos\left[\omega (t-\tau)\right] D_b(\omega). \tag{A-10}$$

Considering an ideal situation, by setting $\left[\ell(\omega)\right]^2 D_b(\omega)/\omega = \gamma/\pi$, we thereby obtain

$$\Theta(t) \approx -\frac{\gamma}{\pi} \int_0^{+\infty} \int_{t_0}^{t+0^+} d\omega d\tau \dot{q}(t) \cos\left[\omega (t-\tau)\right]. \tag{A-11}$$

Using the relations

$$\int_0^{+\infty} \cos\left[\omega (t-\tau)\right] d\omega = \pi \delta(t-\tau), \tag{A-12}$$

and by substituting Eq. (A-1) into $\Theta(t) \approx -\gamma \dot{q}(t)$, we arrive at Eq. (2.5) in the main text:

$$\dot{p} = -\omega_{\mathrm{m}} q - \gamma_{\mathrm{m}} p + G_0 a^\dagger a + \xi, \tag{A-13}$$

where the mechanical damping rate is $\gamma_{\mathrm{m}} = \omega_{\mathrm{m}} \gamma$, which depends on the coupling strength ℓ_n and the characteristic frequency of mechanical oscillator ω_{m}.

A.3 A detailed description of the inverse-resonance region

In our work, we mainly focus on discussing the high-frequency resonance range since its physical significance is clear and universal. However, the high-frequency inverse-resonance range does indeed exist and holds a specific physical meaning as explained below.

A high-frequency inverse-resonance range requires a heat bath consisting of harmonic oscillators with negative-energy modes. Such oscillators are equivalent to those with a negative mass, which have been studied in schemes to evade quantum measurement backaction [79, 80]. Such a scheme was experimentally demonstrated using an atomic spin ensemble initially in its maximal-energy spin state within a magnetic field. Spin flips decrease the energy and correspond to excitations of a harmonic oscillator with a negative mass [81]. Alternatively, a frame rotating faster than the mode itself can effectively realize the negative-energy mode, such as quantum back-action evading measurement of collective mechanical modes [82, 83]. In our setup, a heat bath with negative frequencies can be implemented through engineering dissipation in a multimode optomechanical circuit [52, 76, 77].

We consider a mechanical mode coherently coupled to a heat bath comprising negative-energy modes in the inverse-resonance region $\omega_{\mathrm{m}}(\lambda)\,\omega_n(\lambda) \leqslant 0$, which is described by the Hamiltonian

$$H = \hbar \sum_n \omega_n(\lambda)\,\Lambda_n^\dagger \Lambda_n + \hbar\omega_{\mathrm{m}}(\lambda)\,b^\dagger b - i\hbar \sum_n \frac{\ell_n}{2}\left(\Lambda_n^\dagger - \Lambda_n\right)\left(b^\dagger + b\right). \tag{A-14}$$

with the same symbols defined in the manuscript. Here the bare frequencies $\omega_n(\lambda) \leqslant 0$ and $\omega_{\mathrm{m}}(\lambda) \geqslant 0$ vary with respect to a parameter λ. To achieve a filter design, we introduce a frequency transformation

$$\tilde{\Lambda}_n(t) = \Lambda_n(t)\exp\left[-i\left|\omega_n(\lambda)\right| t\right] \quad \text{and} \quad \tilde{b}(t) = b(t)\exp\left[i\omega_{\mathrm{m}}(\lambda)\, t\right] \tag{A-15}$$

for $\Lambda_n(t)$ and $b(t)$ in the interaction picture [17]. After the transformation, it becomes clear that the mechanical mode has a positive phase (i.e., counterclockwise rotation), whereas its corresponding heat-bath mode exhibits a negative phase (i.e., clockwise rotation). In the presence of high-frequency inverse-resonance dominance, we effectively eliminate the terms $\tilde{\Lambda}_n\tilde{b}^\dagger$ and $\tilde{\Lambda}_n^\dagger\tilde{b}$ associated with high-frequency oscillations. After the filtering process, we keep only the terms of $\tilde{\Lambda}_n^\dagger\tilde{b}^\dagger$ and $\tilde{\Lambda}_n\tilde{b}$, and hence Eq. (A-14) becomes

$$H' = -\hbar \sum_n \left|\omega_n(\lambda)\right| \Lambda_n^\dagger \Lambda_n + \hbar\omega_{\mathrm{m}}(\lambda)\,b^\dagger b - i\hbar \sum_n \frac{\ell_n}{2}\left(\Lambda_n^\dagger b^\dagger - \Lambda_n b\right), \tag{A-16}$$

which satisfies a typical coupling between a positive-energy mode and negative-energy modes.

Despite the negative frequency of the heat bath mode implying a negative mean thermal phonon number, it does harbor intriguing physical features, namely level attraction [78]. Without loss of generality, let us now show it by two minimal models: one is for the usual level repulsion of two coherently coupled positive-energy modes in the high-frequency resonance region, namely a general red-detuned regime, where the dominant term is $-i\hbar\ell_1(\Lambda_1^\dagger b - \Lambda_1 b^\dagger)/2$, describing the exchange of quanta between them [40]; the other is for level attraction of a negative-energy mode coherently coupled to a positive-energy mode in the High-frequency inverse-resonance region, namely a general blue-detuned regime, where the dominant term is $-i\hbar\ell_1(\Lambda_1^\dagger b^\dagger - \Lambda_1 b)/2$, representing a two-mode squeezing interaction that lies at the heart of parametric amplification [85]. There is a symmetry relation linking the two cases, as they are images of each other.

First, we derive the level repulsion of two coupled positive-energy modes with an energy crossing, which has applications ranging from solid-state theory to quantum chemistry. Two modes of positive energy interact with each other, as described by the Hamiltonian [78]

$$H_{\mathrm{LR}} = \hbar\left|\omega_1(\lambda)\right|\Lambda_1^\dagger\Lambda_1 + \hbar\omega_{\mathrm{m}}(\lambda)\, b^\dagger b - i\hbar\frac{\ell_1}{2}\left(\Lambda_1^\dagger b - \Lambda_1 b^\dagger\right), \tag{A-17}$$

The equation of motion in the Heisenberg picture are given by

$$\frac{d}{dt}\begin{pmatrix}\Lambda_1\\ b\end{pmatrix} = -i\begin{pmatrix}|\omega_1| & \frac{1}{2}i\ell_1\\ -\frac{1}{2}i\ell_1 & \omega_{\mathrm{m}}\end{pmatrix}\begin{pmatrix}\Lambda_1\\ b\end{pmatrix}. \tag{A-18}$$

The hybridized eigenmodes $\tilde{\omega}_{\mathrm{LR}}$ of the system are obtained by diagonalizing the coefficient matrix in Eq. (A-18), and resulting in the eigenfrequencies

$$\omega_{\mathrm{LR}}^{\pm} = \frac{1}{2}\left\{|\omega_1| + \omega_{\mathrm{m}} \pm \sqrt{\left(|\omega_1| - \omega_{\mathrm{m}}\right)^2 + \ell_1^2}\right\}, \tag{A-19}$$

where we dropped the explicit λ dependence. We now consider level attraction. A negative-energy mode is coherently coupled to a positive-energy mode such that the system is described by the Hamiltonian

$$H_{\mathrm{LA}} = -\hbar\left|\omega_1(\lambda)\right|\Lambda_1^\dagger\Lambda_1 + \hbar\omega_{\mathrm{m}}(\lambda)\, b^\dagger b - i\hbar\frac{\ell_1}{2}\left(\Lambda_1^\dagger b^\dagger - \Lambda_1 b\right). \tag{A-20}$$

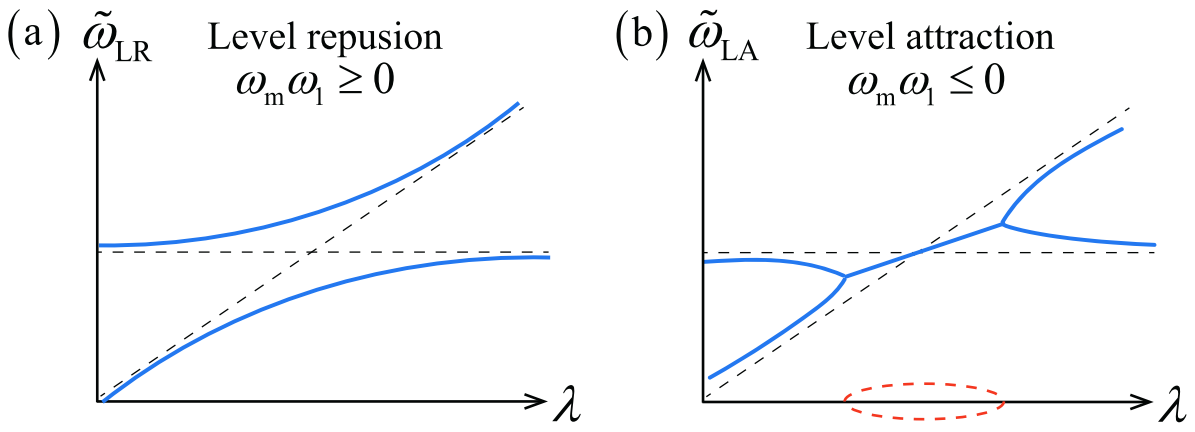

Figure A.1: Level repulsion and attraction are characterized by ω_1 [78]. Two modes, whose bare frequencies depend on a parameter λ, have a level crossing (dotted lines). When a coherent coupling is introduced, it generally lifts the degeneracy between these modes, leading to distinct behaviors. In the more common scenario of level repulsion (a), the coupling opens a gap between the frequencies of the hybridized eigenmodes $\tilde{\omega}_{\mathrm{LR}}$ (blue solid lines) and the eigenfrequencies $\omega_{\mathrm{LR}}^{\pm}$ bend away from each other. In contrast, in the case of level attraction (b), where one mode exhibits negative energy, level attraction occurs. The real components of the eigenfrequencies $\omega_{\mathrm{LA}}^{\pm}$ (blue solid lines) bend towards each other, converging at two exceptional points marked by kinks. Simultaneously, finite imaginary components of the frequencies emerge (orange dashed lines). Notably, the mode with a negative imaginary component becomes unstable, exhibiting exponential growth.

The equation of motion in the Heisenberg picture is given by

$$\frac{d}{dt}\begin{pmatrix}\Lambda_1\\ b^\dagger\end{pmatrix} = i\begin{pmatrix}|\omega_1| & \frac{1}{2}i\ell_1\\ \frac{1}{2}i\ell_1 & \omega_{\mathrm{m}}\end{pmatrix}\begin{pmatrix}\Lambda_1\\ b^\dagger\end{pmatrix} \tag{A-21}$$

with the eigenmodes $\tilde{\omega}_{\mathrm{LA}}$ and the corresponding eigenfrequencies

$$\omega_{\mathrm{LA}}^{\pm} = \frac{1}{2}\left\{|\omega_1| + \omega_{\mathrm{m}} \pm \sqrt{\left(|\omega_1| - \omega_{\mathrm{m}}\right)^2 - \ell_1^2}\right\}, \tag{A-22}$$

where we dropped the explicit λ dependence.

The only difference between Eqs. (A-19) and (A-22) is the sign in front of ℓ_1^2. However, it dramatically impacts physics. The Hermitian Hamitonian (A-20) can result in a complex eigenvalue and unstable dynamics, which the eigenoperators cannot be interpreted as Bogoli-

ubov modes [120]. We depict the repulsion and attraction of levels in Fig. A.1. In contrast to the level repulsion (A-17), the level attraction (A-20) has two prominent features. First, the eigenfrequencies are drawn towards each other instead of avoiding each other. Second, to satisfy condition $\left(\left|\omega_1\left(\lambda\right)\right|-\omega_{\mathrm{m}}\right)^2=\ell_1^2$, the frequencies acquire negative and positive imaginary parts, leading to exponential growth and decay. Thus, the heat bath consisting of a group of harmonic oscillators with negative modes in Hamitonian (A-16) exhibits instability. Furthermore, we observe that the level attraction arises when the coupling term includes a Pauli matrix with an imaginary coefficient.

In the case of the level attraction, the interaction term can be expressed as $i\ell_1\sigma_x/\,2$ by decomposing it in terms of Pauli matrices and omitting the term proportional to the identity; In contrast to the level repulsion, for which the interaction term would be $-\ell_1\sigma_y/\,2$. In addition, we decompose the coefficient matrix in Eq. (A-21) into $\left[\left(\left|\omega_1\right|-\omega_{\mathrm{m}}\right)\sigma_z+i\ell_1\sigma_x\right]/\,2$. If the first term has a larger amplitude, the eigenfrequencies are real, while they are complex if the second term dominates. It is worth noting that when the two Pauli matrices have coefficients of the same amplitude, the matrix is proportional to $\sigma_z+i\sigma_x$. At this point, the two eigenvectors coalesce, and a single eigenvector with a single eigenvalue subsists, marked by an exceptional point, which corresponds to the point of maximal non-reciprocity, leading to a possible non-reciprocal photon transmission and amplification via reservoir engineering [84]. More details are explained in Ref. [78].

To sum up, we have shown that the negative frequency of the heat bath holds a particular and significant physical meaning. First, the quantum back-action evading measurement of collective mechanical modes provides the possibility to prepare an ensemble of effective negative mass oscillators. Second, negative-energy modes coupled with a positive mode, having opposite phases between a mechanical mode and modes of heat bath, can lead to an intriguing level attraction of complex spectrums associated with exceptional points and unstable dynamics.

A.4 Details of the derivation of Eqs. (2.11) and (2.12)

In this Appendix, we focus on deriving the nonlinear Langevin equations (2.11) and (2.12) satisfied by the filtering model H_{F} under the dominance of resonance effects. Specifically, we

concentrate on the mechanical mode b, keeping the optical cavity mode a take the same form as the dynamical Eq. (2.6). By substituting filtering model H_{F} into the Heisenberg equation, we obtain

$$\dot{b} = \frac{1}{i\hbar}\left[b, H_{\mathrm{T}}\right] = -i\omega_{\mathrm{m}} b + i\frac{G_0}{\sqrt{2}} a^{\dagger} a + \frac{1}{2}\sum_n \ell_n \Lambda_n, \tag{A-23}$$

$$\dot{b}^{\dagger} = \frac{1}{i\hbar}\left[b^{\dagger}, H_{\mathrm{T}}\right] = i\omega_{\mathrm{m}} b^{\dagger} - i\frac{G_0}{\sqrt{2}} a^{\dagger} a + \frac{1}{2}\sum_n \ell_n \Lambda_n^{\dagger}, \tag{A-24}$$

$$\dot{\Lambda}_n = \frac{1}{i\hbar}\left[\Lambda_n, H_{\mathrm{F}}\right] = -i\omega_n \Lambda_n - \frac{\ell_n}{2} b, \tag{A-25}$$

$$\dot{\Lambda}_n^{\dagger} = \frac{1}{i\hbar}\left[\Lambda_n^{\dagger}, H_{\mathrm{F}}\right] = i\omega_n \Lambda_n^{\dagger} - \frac{\ell_n}{2} b^{\dagger}. \tag{A-26}$$

The derivatives of p and q with respect to time read

$$\dot{q} = \frac{1}{\sqrt{2}}\left(\dot{b}^{\dagger} + \dot{b}\right) = \omega_{\mathrm{m}} p + \frac{1}{2}\sum_n \ell_n q_n, \tag{A-27}$$

$$\dot{p} = \frac{i}{\sqrt{2}}\left(\dot{b}^{\dagger} - \dot{b}\right) = -\omega_{\mathrm{m}} q + G_0 a^{\dagger} a + \frac{1}{2}\sum_n \ell_n p_n. \tag{A-28}$$

We are interested in the system operators p and q. Equations (A-25) and (A-26) for Λ_n and $\Lambda_n^{\dagger}$ can be formally integrated to yield

$$\Lambda_n(t) = \Lambda_n(t_0)\, e^{-i\omega_n (t-t_0)} - \frac{\ell_n}{2}\int_{t_0}^{t} b(\tau) e^{-i\omega_n (t-\tau)} d\tau, \tag{A-29}$$

$$\Lambda_n^{\dagger}(t) = \Lambda_n^{\dagger}(t_0)\, e^{i\omega_n (t-t_0)} - \frac{\ell_n}{2}\int_{t_0}^{t} b^{\dagger}(\tau) e^{i\omega_n (t-\tau)} d\tau. \tag{A-30}$$

The parts of Eqs. (A-27) and (A-28) that contain environmental operators q_n and p_n can be written as

$$\begin{aligned}\frac{1}{2}\sum_n \ell_n q_n = \frac{1}{2}\sum_n \ell_n \frac{\Lambda_n^{\dagger} + \Lambda_n}{\sqrt{2}} &= \frac{1}{2}\sum_n \ell_n \frac{1}{\sqrt{2}}\left[\Lambda_n^{\dagger}(t_0)\, e^{i\omega_n (t-t_0)} + \Lambda_n(t_0)\, e^{-i\omega_n (t-t_0)}\right] \\ &- \sum_n \left(\frac{\ell_n}{2}\right)^2 \frac{1}{\sqrt{2}}\left[\int_{t_0}^{t} b^{\dagger}(\tau) e^{i\omega_n (t-\tau)} d\tau + \int_{t_0}^{t} b(\tau) e^{-i\omega_n (t-\tau)} d\tau\right],\end{aligned} \tag{A-31}$$

$$\begin{aligned}\frac{1}{2}\sum_n \ell_n p_n = \frac{1}{2}\sum_n \ell_n \frac{i\left(\Lambda_n^{\dagger} - \Lambda_n\right)}{\sqrt{2}} &= \frac{1}{2}\sum_n \ell_n \frac{i}{\sqrt{2}}\left[\Lambda_n^{\dagger}(t_0)\, e^{i\omega_n (t-t_0)} - \Lambda_n(t_0)\, e^{-i\omega_n (t-t_0)}\right] \\ &- \sum_n \left(\frac{\ell_n}{2}\right)^2 \frac{i}{\sqrt{2}}\left[\int_{t_0}^{t} b^{\dagger}(\tau) e^{i\omega_n (t-\tau)} d\tau - \int_{t_0}^{t} b(\tau) e^{-i\omega_n (t-\tau)} d\tau\right].\end{aligned} \tag{A-32}$$

For convenience, we concisely express Eqs. (A-31) and (A-32) as

$$\frac{1}{2}\sum_n \ell_n q_n = \frac{1}{2}\xi'(t) - \chi'(t), \quad \frac{1}{2}\sum_n \ell_n p_n = \frac{1}{2}\xi(t) - \chi(t), \tag{A-33}$$

where

$$\xi'(t) = \sum_n \ell_n \frac{1}{\sqrt{2}}\left[\Lambda_n^\dagger(t_0)\, e^{i\omega_n(t-t_0)} + \Lambda_n(t_0)\, e^{-i\omega_n(t-t_0)}\right], \tag{A-34}$$

$$\xi(t) = \sum_n \ell_n \frac{i}{\sqrt{2}}\left[\Lambda_n^\dagger(t_0)\, e^{i\omega_n(t-t_0)} - \Lambda_n(t_0)\, e^{-i\omega_n(t-t_0)}\right], \tag{A-35}$$

$$\chi'(t) = \sum_n \left(\frac{\ell_n}{2}\right)^2 \int_{t_0}^{t} \{q(\tau)\cos[\omega_n(t-\tau)] + p(\tau)\sin[\omega_n(t-\tau)]\} d\tau, \tag{A-36}$$

$$\chi(t) = \sum_n \left(\frac{\ell_n}{2}\right)^2 \int_{t_0}^{t} \{p(\tau)\cos[\omega_n(t-\tau)] - q(\tau)\sin[\omega_n(t-\tau)]\} d\tau. \tag{A-37}$$

Next, we make approximations. In a similar way to Appendix A.2, under the Born-Markov and Weisskopf-Wigner approximations, Eqs. (A-36) and (A-37) become

$$\chi'(t) = \frac{1}{4}\int_0^{+\infty}\int_{t_0}^{t+0^+} d\tau d\omega \{\dot{q}(t)\sin[\omega(t-\tau)] - \dot{p}(t)\cos[\omega(t-\tau)]\}\frac{[\ell(\omega)]^2 D_b(\omega)}{\omega}, \tag{A-38}$$

$$\chi(t) = \frac{1}{4}\int_0^{+\infty}\int_{t_0}^{t+0^+} d\tau d\omega \{\dot{p}(t)\sin[\omega(t-\tau)] + \dot{q}(t)\cos[\omega(t-\tau)]\}\frac{[\ell(\omega)]^2 D_b(\omega)}{\omega}. \tag{A-39}$$

Furthermore, we set $[\ell(\omega)]^2 D_b(\omega)/\omega = \gamma/\pi$. Then, by using the relation $\int_0^{+\infty}\cos[\omega(t-\tau)]\, d\omega = \pi\delta(t-\tau)$ and $\int_0^{+\infty}\sin[\omega(t-\tau)]\, d\omega = 0$, we find $\chi'(t) = -\gamma\dot{p}(t)/4$ and $\chi(t) = \gamma\dot{q}(t)/4$.

Finally, Eqs. (A-27) and (A-28) can be rewritten as

$$\dot{q} = \omega_{\mathrm{m}} p + \frac{\gamma}{4}\dot{p} + \frac{1}{2}\xi', \quad \dot{p} = -\omega_{\mathrm{m}} q - \frac{\gamma}{4}\dot{q} + G_0 a^\dagger a + \frac{1}{2}\xi(t). \tag{A-40}$$

We ultimately reproduce the same equations as Eqs. (2.11) and (2.12), which are presented in the main text.

A.5 Details of the derivation of the Eqs. (2.15)-(2.17)

We set the mechanical damping rate as $\gamma_m = \omega_m\gamma$. For the part of the quantum fluctuation

operators, we have

$$\delta\dot{q} = \omega_{\mathrm{m}}\delta p + \frac{\gamma}{4}\delta\dot{p} + \frac{1}{2}\xi', \tag{A-41}$$

$$\delta\dot{p} = -\omega_{\mathrm{m}}\delta q - \frac{\gamma}{4}\delta\dot{q} + G_0\left(\alpha_{\mathrm{s}}^{*}\delta a + \alpha_s\delta a^{\dagger} + \delta a\delta a^{\dagger}\right) + \frac{1}{2}\xi, \tag{A-42}$$

$$\delta\dot{a} = -\left(\kappa + i\Delta_0\right)\delta a + iG_0\left(\alpha_{\mathrm{s}}\delta q + q_{\mathrm{s}}\delta a + \delta a\delta q\right) + \sqrt{2\kappa}a_{\mathrm{in}}. \tag{A-43}$$

In order to decouple $\delta\dot{q}$ and $\delta\dot{p}$, by substituting Eqs. (A-41) and (A-42) into each other, we obtain

$$\begin{aligned}
\left(1+\frac{\gamma^2}{16}\right)\delta\dot{q} &= \omega_{\mathrm{m}}\delta p - \frac{\gamma_{\mathrm{m}}}{4}\delta q + \frac{1}{2}\xi' + \frac{\gamma G_0}{4}\left(\alpha_{\mathrm{s}}^{*}\delta a + \alpha_s\delta a^{\dagger} + \delta a\delta a^{\dagger}\right) + \frac{1}{8}\gamma\xi, \\
\left(1+\frac{\gamma^2}{16}\right)\delta\dot{p} &= -\omega_{\mathrm{m}}\delta q - \frac{\gamma_{\mathrm{m}}}{4}\delta p + G_0\left(\alpha_{\mathrm{s}}^{*}\delta a + \alpha_s\delta a^{\dagger}\right) + \frac{1}{2}\xi + G_0\delta a\delta a^{\dagger} - \frac{1}{8}\gamma\xi', \\
\delta\dot{a} &= -\left(\kappa + i\Delta\right)\delta a + iG_0\alpha_{\mathrm{s}}\delta q + \sqrt{2\kappa}a_{\mathrm{in}} + iG_0\delta a\delta q,
\end{aligned} \tag{A-44}$$

where $\gamma_{\mathrm{m}} = \gamma\omega_{\mathrm{m}}$. By dropping the second-order small terms, we obtain the linearized Langevin equations

$$\delta\dot{q} = \omega_{\mathrm{m}}\delta p - \frac{\gamma_{\mathrm{m}}}{4}\delta q + \frac{1}{2}\xi', \tag{A-45}$$

$$\delta\dot{p} = -\omega_{\mathrm{m}}\delta q - \frac{\gamma_{\mathrm{m}}}{4}\delta p + G_0\left(\alpha_{\mathrm{s}}^{*}\delta a + \alpha_{\mathrm{s}}\delta a^{\dagger}\right) + \frac{1}{2}\xi, \tag{A-46}$$

$$\delta\dot{a} = -\left(\kappa + i\Delta\right)\delta a + iG_0\alpha_{\mathrm{s}}\delta q + \sqrt{2\kappa}a_{\mathrm{in}}, \tag{A-47}$$

which are consistent with Eqs. (2.15)-(2.17) in the main text.

A.6 Details of the derivation of the Lyapunov equation

This Appendix derives the Lyapunov equation $AV + VA^T + D = 0$. We begin with the definition of the covariance matrix. According to the definition [121], any matrix element of the covariance matrix can be expressed as

$$V_{ij}\left(t\right) = \frac{1}{2}\left\langle \mu_i\left(t\right)\mu_j\left(t\right) + \mu_j\left(t\right)\mu_i\left(t\right)\right\rangle, \tag{A-48}$$

which satisfies the differential equation

$$\frac{dV_{ij}(t)}{dt} = \frac{1}{2}\left\langle \frac{d\mu_i(t)}{dt}\mu_j(t) + \mu_i(t)\frac{d\mu_j(t)}{dt} + \frac{d\mu_j(t)}{dt}\mu_i(t) + \mu_j(t)\frac{d\mu_i(t)}{dt} \right\rangle. \tag{A-49}$$

The matrix elements of the differential equation (A-49) read

$$\dot{\mu}_i(t) = \sum_o A_{io}\mu_i(t) + n_i(t). \tag{A-50}$$

Substituting Eq. (A-50) into Eq. (A-49), we obtain

$$\begin{aligned}
\frac{dV_{ij}(t)}{dt} =& + \frac{1}{2}\left\langle \left[\sum_o A_{io}\mu_o(t) + n_i(t)\right]\mu_j(t) + \mu_i(t)\left[\sum_o A_{jo}\mu_o(t) + n_j(t)\right]\right\rangle \\
&+ \frac{1}{2}\left\langle \left[\sum_o A_{jo}\mu_o(t) + n_j(t)\right]\mu_i(t) + \mu_j(t)\left[\sum_o A_{io}\mu_o(t) + n_i(t)\right]\right\rangle \\
=& + \sum_o A_{io}(t)V_{oj}(t) + \sum_o A_{jo}(t)V_{io}(t) + D_{ij}(t),
\end{aligned} \tag{A-51}$$

where

$$D_{ij}(t) = \frac{\langle n_i(t)\mu_j(t)\rangle + \langle \mu_i(t) n_j(t)\rangle + \langle n_j(t)\mu_i(t)\rangle + \langle \mu_j(t) n_i(t)\rangle}{2}. \tag{A-52}$$

We then calculate each term in D_{ij}. For example, we have

$$\begin{aligned}
\langle n_i(t)\mu_j(t)\rangle &= \sum_o M_{jo}(t,t_0)\langle n_i(t)\mu_o(t_0)\rangle + \sum_o \int_{t_0}^{t} M_{jo}(t,\tau)\langle n_i(t) n_j(\tau)\rangle d\tau \\
&= \sum_o \int_{t_0}^{t} M_{jo}(t,\tau)\langle n_i(t) n_j(\tau)\rangle d\tau,
\end{aligned} \tag{A-53}$$

where $M(t) = \exp(At)$. Similarly, we obtain the other terms in D_{ij} in the forms

$$\langle \mu_{\mathrm{i}}(t) n_{\mathrm{j}}(t)\rangle = \sum_{\mathrm{o}} \int_{t_0}^{t} \mathrm{M_{io}}(t,\tau)\langle n_{\mathrm{o}}(\tau) n_{\mathrm{j}}(t)\rangle d\tau, \tag{A-54}$$

$$\langle n_{\mathrm{j}}(t)\mu_{\mathrm{i}}(t)\rangle = \sum_{\mathrm{o}} \int_{t_0}^{t} \mathrm{M_{io}}(t,\tau)\langle n_{\mathrm{j}}(t) n_{\mathrm{o}}(\tau)\rangle d\tau, \tag{A-55}$$

$$\langle \mu_{\mathrm{j}}(t) n_{\mathrm{i}}(t)\rangle = \sum_{\mathrm{o}} \int_{t_0}^{t} \mathrm{M_{jo}}(t,\tau)\langle n_{\mathrm{o}}(\tau) n_{\mathrm{i}}(t)\rangle d\tau. \tag{A-56}$$

Hence, D_{ij} can be written as

$$D_{ij} = \sum_o \int_{t_0}^{t} M_{jo}(t,\tau)\,\Phi_{io}^{(1)}(t,\tau)\,d\tau + \sum_o \int_{t_0}^{t} M_{io}(t,\tau)\,\Phi_{oj}^{(2)}(t,\tau)\,d\tau, \tag{A-57}$$

where

$$\Phi_{io}^{(1)}(t,\tau) = \frac{1}{2}\left\langle n_i(t)\,n_o(\tau) + n_o(\tau)\,n_i(t)\right\rangle, \tag{A-58}$$

$$\Phi_{oj}^{(2)}(t,\tau) = \frac{1}{2}\left\langle n_o(\tau)\,n_j(t) + n_j(t)\,n_o(\tau)\right\rangle. \tag{A-59}$$

The transposes of the column vector of noise operators are given by Eq. (2.19). We note that the non-zero correlation functions satisfy the following relations:

$$2\left\langle X_{\text{in}}(t)\,Y_{\text{in}}(\tau)\right\rangle = -2\left\langle Y_{\text{in}}(t)\,X_{\text{in}}(\tau)\right\rangle = -i\delta(t-\tau), \tag{A-60}$$

$$2\left\langle X_{\text{in}}(t)\,X_{\text{in}}(\tau)\right\rangle = 2\left\langle Y_{\text{in}}(t)\,Y_{\text{in}}(\tau)\right\rangle = (2\bar{n}_a+1)\,\delta(t-\tau), \tag{A-61}$$

$$\left\langle \xi(t)\,\xi(\tau) + \xi(\tau)\,\xi(t)\right\rangle = \left\langle \xi'(t)\,\xi'(\tau) + \xi'(\tau)\,\xi'(t)\right\rangle = 2\gamma_{\text{m}}(2\bar{n}+1)\,\delta(t-\tau). \tag{A-62}$$

To be concise, we set $\bar{n}_a = 0$. Using the relation (A-60)-(A-62), we calculate each term of $\Phi_{io}^{(1)}(t,\tau)$ and $\Phi_{oj}^{(2)}(t,\tau)$. The result is given by

$$\Phi_{io}^{(1)} = \begin{pmatrix} \Phi_{11}^{(1)} & \Phi_{12}^{(1)} & \Phi_{13}^{(1)} & \Phi_{14}^{(1)} \\ \Phi_{21}^{(1)} & \Phi_{22}^{(1)} & \Phi_{23}^{(1)} & \Phi_{24}^{(1)} \\ \Phi_{31}^{(1)} & \Phi_{32}^{(1)} & \Phi_{33}^{(1)} & \Phi_{34}^{(1)} \\ \Phi_{41}^{(1)} & \Phi_{42}^{(1)} & \Phi_{43}^{(1)} & \Phi_{44}^{(1)} \end{pmatrix} = D_{io}\delta(t-\tau), \tag{A-63}$$

where D_{io}= diag $[\gamma_{\text{m}}(2\bar{n}+1)/4, \gamma_{\text{m}}(2\bar{n}+1)/4, \kappa, \kappa]$. Similarly, we obtain

$$\Phi_{oj}^{(2)} = D_{oj}\delta(t-\tau) = \text{diag}\left[\gamma_{\text{m}}(2\bar{n}+1)/4, \gamma_{\text{m}}(2\bar{n}+1)/4, \kappa, \kappa\right]\delta(t-\tau). \tag{A-64}$$

Therefore, Eq. (A-57) can be rewritten as

$$\begin{aligned} D_{ij} &= \sum_o \int_{t_0}^{t} M_{jo}\left(t,\tau\right) \Phi_{io}^{(1)}\left(t,\tau\right) d\tau + \sum_o \int_0^{t} M_{io}\left(t,\tau\right) \Phi_{oj}^{(2)}\left(t,\tau\right) d\tau \\ &= \sum_o \int_{t_0}^{t} M_{jo}\left(t,\tau\right) D_{io}\delta\left(t-\tau\right) d\tau + \sum_o \int_{t_0}^{t} M_{io}\left(t,\tau\right) D_{oj}\delta\left(t-\tau\right) d\tau \\ &= \frac{1}{2}\sum_o \mathrm{I}_{jo} D_{io} + \frac{1}{2}\sum_o \mathrm{I}_{io} D_{oj} = \frac{1}{2}\sum_o D_{io}\mathrm{I}_{oj}^{T} + \frac{1}{2}\sum_o \mathrm{I}_{io} D_{oj} \equiv D, \end{aligned} \tag{A-65}$$

where $D = \mathrm{diag}\left[\gamma_{\mathrm{m}}\left(2\bar{n}+1\right)/4, \gamma_{\mathrm{m}}\left(2\bar{n}+1\right)/4, \kappa, \kappa\right]$. Hence, we obtain

$$AV = \int_{t_0}^{\infty} AM(\tau) D M(\tau)^T d\tau = \int_{t_0}^{\infty} \frac{d}{d\tau} M(\tau) D M(\tau)^T d\tau, \tag{A-66}$$

$$VA^T = \int_{t_0}^{\infty} M(\tau) D (AM(\tau))^T d\tau = \int_{t_0}^{\infty} M(\tau) D \frac{d}{d\tau} M(\tau)^T d\tau. \tag{A-67}$$

The combination of Eqs. (A-66) and (A-67) becomes

$$\begin{aligned} AV + VA^T &= + \int_{t_0}^{\infty} \frac{d}{d\tau}[M(\tau) D M(\tau)^T] d\tau - \int_{t_0}^{\infty} M(\tau) \frac{d}{d\tau} D M(\tau)^T d\tau \\ &= + \left[M\left(\tau\right) D M(\tau)^T\right]\big|_{t_0}^{+\infty} = -D. \end{aligned} \tag{A-68}$$

When the stability conditions are satisfied, in the long-time limit, the derivative of the covariance matrix with respect to time approaches zero, $\dot{V} = 0$, and the solution $M\left(+\infty\right)$ converges to zero. This produces the Lyapunov equation in the main text, $AV + VA^T = -D$.

Chapter 3

Topological quantum batteries

3.1 Introduction

With the decline of fossil fuels and the worsening of the global energy crisis, conventional chemical batteries that charge and discharge through chemical reactions will gradually be phased out. Instead, driven by the potential power of quantum effects and the demands for nanotechnological miniaturization, the size of energy storage and conversion devices has shrunk to atomic scales. With this background, Alicki and Fannes first proposed the concept of quantum batteries in 2013 [122]. Fundamentally distinct from conventional batteries, quantum batteries exploit unique quantum features for energy storage and release, potentially outperforming classical counterparts with enhanced charging power [123–134], increased capacity [135–139], and superior work extraction [140–145]. Since then, a variety of possible quantum batteries have been constructed, including Dicke type, spin-chain type, central-spin type, *etc* [146–158]. In particular, a minimal yet favorite quantum battery model based on two-level systems has been extensively studied both in theory [159–164] and experimental implementation [165–168].

Like quantum heat engines, quantum batteries offer a practical platform for incorporating quantum effects into quantum thermodynamics [169–173]. Extensive studies have focused on the performance of quantum batteries in terms of their charging power and stored energy from the perspective of quantum thermodynamics. Notably, the concept of ergotropy—another

crucial performance indicator for quantum batteries that describes the maximum extractable energy—was introduced by Allahverdyan, Balian, and Nieuwenhuizen [174]. Very recent research indicates that coupling a quantum battery and a charger to a specific waveguide, such as a rectangular hollow metal waveguide, facilitates efficient remote charging of the quantum battery but inevitably results in low stored energy and diminished ergotropy [175–177]. A related challenge is whether a configuration exists that can effectively enhance the stored energy and the ergotropy of quantum batteries.

Towards implementing quantum batteries in practical applications, another natural obstacle is environment-induced decoherence caused by inevitable dissipation, which in general, decreases the performance of the quantum battery, such as the energy loss and aging of quantum battery [178–183]. Recently, the study of quantum battery dynamics in the presence of an environment has attracted a deal of attention, and several schemes have been proposed to mitigate the effects of decoherence, including feedback control [184], exploiting non-Markovian effects [185, 186], Floquet engineering [187], *etc*. However, does there exist a configuration that can completely isolate the quantum battery from the effects of dissipation? Our work offers substantial answers.

Topological concepts discovered in electronic systems [188, 189] have been translated and studied as photonic analogs in diverse microwave and optical systems [190, 191]. In particular, the Su-Schrieffer-Heeger model and its extensions have been used in photonics to investigate various optical phenomena [192–194]. On the other hand, using quantum emitters creates new opportunities to explore topological properties involving interacting photons, especially the topological protection exhibited by the Su-Schrieffer-Heeger model under single-excitation dynamics, which has been recently investigated [195]. Similarly, a topological photonic bath can be an effective substrate, imparting unique properties to quantum emitters. For instance, a photonic waveguide that localizes and transports electromagnetic waves over long distances can create a highly effective quantum light-matter interface [196–199], facilitating nontrivial interactions between quantum emitters [200–203]. Inspired by topological waveguide quantum electrodynamics advancements and advantages (QED) [204–207], we here propose a scheme in this work that enhances the stored energy and the ergotropy by coupling two-level systems with topological waveguide baths to overcome the above challenge fully. We also discover that directly coupling the quantum charger and quantum battery enables the performance of

the quantum battery to resist decoherence, stemming from the presence of a dark state and vacancy-like dressed bound state.

In the experiment, quantum emitters coupled to a topological waveguide, which acts as a photonic analog of the Su-Schrieffer-Heeger model, were realized by connecting superconducting transmon qubits to an engineered superconducting metamaterial waveguide [208–210]. This waveguide comprises an array of subwavelength microwave resonators with Su-Schrieffer-Heeger topology. By integrating principles from waveguide quantum electrodynamics and topological photonics [211, 212], researchers very recently observed qubit-photon bound states with directional photonic envelopes within a band gap and cooperative radiative emission from qubits within a passband, the findings demonstrate that coupling qubits to the waveguide allows quantum control over topological edge states, enabling quantum state transfer between distant qubits via a topological photonic waveguide [213]. Additionally, the charging and discharging process of the battery can be experimentally verified through the measurement layout inversion of a two-level atom [214].

In this Chapter, by leveraging topological properties, we develop a novel configuration named topological quantum batteries, which consists of two two-level systems coupled to the Su-Schrieffer-Heeger lattice. With the aid of this setting, we simultaneously address two major challenges related to quantum batteries. One involves achieving near-perfect charging for quantum batteries, while the other focuses on dissipation immunity engineering. Furthermore, we demonstrate that utilizing the quantum Zeno effect boosts both the charging power and ergotropy of quantum batteries in a short time.

3.2 Setup and dynamics

3.2.1 Setup

As shown in Fig. 3.1, we begin by considering a quantum charger and a quantum battery that are linearly coupled, each modeled as a two-level atom. These two-level systems are connected to a one-dimensional Su-Schrieffer-Heeger (SSH) [215, 216] photonic lattice designed with engineered photon loss [217, 218]. Under the Markovian and rotating-wave approxima-

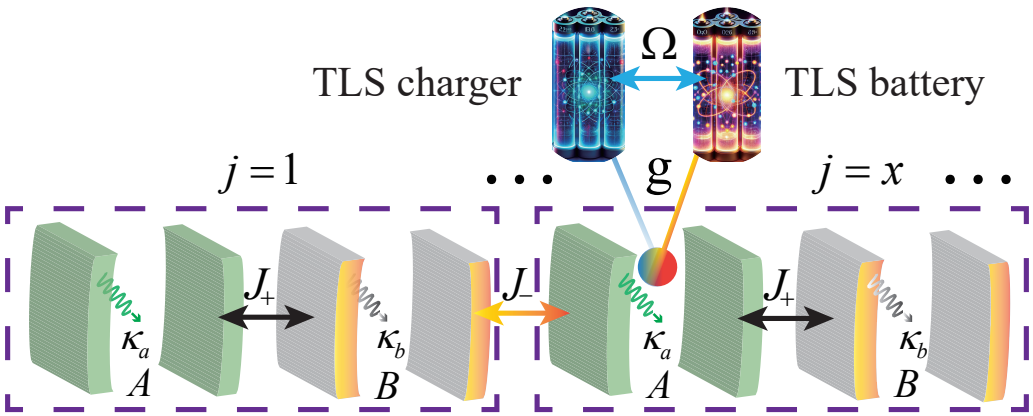

Figure 3.1: Configuration illustration of the topological quantum battery. The quantum charger and quantum battery, formed by linearly interacting two-level systems (TLSs), are coupled to a one-dimensional topological photonic waveguide.

tions [219], the equation of motion (in the rotating frame) reads

$$\dot{\rho}_t = -i\left[H_{\text{sys}} + H_{\text{ssh}} + H_{\text{int}}, \rho_t\right] + \mathcal{L}_a\rho_t + \mathcal{L}_b\rho_t, \tag{3-1}$$

where

$$H_{\text{sys}} = \Delta\left(\sigma_z^{\text{B}} + \sigma_z^{\text{C}}\right)/2 + \Omega_{12}^{\alpha\beta}\left(\sigma_+^{\text{B}}\sigma_-^{\text{C}} + \text{H.c.}\right), \tag{3-2}$$

$$H_{\text{ssh}} = \sum_{j=1}^{N}\left(J_+ a_j^\dagger b_j + J_- b_j^\dagger a_{j+1} + \text{H.c.}\right), \tag{3-3}$$

$$H_{\text{int}} = \text{g}\left(\sigma_-^{\text{B}} o_{x_{1,\alpha}}^\dagger + \sigma_-^{\text{C}} o_{x_{2,\beta}}^\dagger + \text{H.c.}\right), \tag{3-4}$$

with $\Omega_{12}^{\alpha\beta} = \Omega\delta_{x_1,x_2}\delta_{\alpha,\beta}$, which implies that two-level systems are placed in the same cavity and are directly coupled with strength Ω. The Hamiltonian (3-2) describes a linear coupling between two two-level systems, with detuning Δ between the resonance frequencies of the two-level systems and the cavity-free frequency, under the assumption that the frequency of each cavity is identical. The Hamiltonian (3-3) represents a structured bosonic bath with intracell hopping J_+ and intercell hopping J_-. Here, we assume periodic boundary conditions $a_{N+1} = a_1$. The Hamiltonian (3-4) gives the atom-bath interaction with coupling strength g, where σ_+^{B} (σ_+^{C}) and σ_-^{B} (σ_-^{C}) denote the raising and lowering Pauli operators of quantum battery (quantum charger), respectively. Here, $a_j^\dagger$ (a_j) or $b_j^\dagger$ (b_j) are the creation (annihilation) operators of the sites A or B at the jth unit cell, with $\hbar = 1$ here and hereafter. We note that for $o_{x_{j,\alpha(\beta)}}$ with

$\{\alpha, \beta\} \in \{A, B\}$, we set $o_{x_{j,A}} \equiv a_{x_j}$ and $o_{x_{j,B}} \equiv b_{x_j}$. In other words, the quantum charger and the quantum battery are placed at different sites. The photon dissipators of different sublattices are given by $\mathcal{L}_a = \kappa_a \sum_j \mathcal{D}[a_j]$ and $\mathcal{L}_b = \kappa_b \sum_j \mathcal{D}[b_j]$, where κ_a (κ_b) controls the photon loss rates of sublattice A (B), and $\mathcal{D}[L]\rho = L\rho L^\dagger - \{L^\dagger L, \rho\}/2$ is the Lindblad superoperator.

The effective non-Hermitian Hamiltonian we obtain from Eq. (3-1) is given by $H_{\text{eff}} = H_{\text{sys}} + H_{\text{ssh}}^{\text{eff}} + H_{\text{int}}$, where $H_{\text{ssh}}^{\text{eff}} = H_{\text{ssh}} - (i/2)\sum_j (\kappa_a a_j^\dagger a_j + \kappa_b b_j^\dagger b_j)$. We suppose that the initial state is in the single-excitation sector. To be specific, the charger is fully charged to the excited state, whereas the quantum battery is depleted to the ground state. Additionally, the bath is in the vacuum state $|\text{vac}\rangle$. Then, the solution to Eq. (3-1) reads $\rho_t = e^{-iH_{\text{eff}}t}\rho_0 e^{iH_{\text{eff}}^\dagger t} + p_t \left|g, g; \text{vac}\right\rangle \left\langle g, g; \text{vac}\right|$ with $p_t = 1 - \text{Tr}[e^{-iH_{\text{eff}}t}\rho_0 e^{iH_{\text{eff}}^\dagger t}]$ [220,221], in which the initial density matrix is written as $\rho_0 = |\psi(0)\rangle\langle\psi(0)|$ with $|\psi(0)\rangle = |e, g; \text{vac}\rangle$. Therefore, by limiting our analysis to the single-excitation sector, we can concentrate on studying the effective non-Hermitian Hamiltonian. Further, by defining $\mathbf{o}_k = [a_k, b_k]^T$ with $a_k^\dagger = \sum_{j=1}^N e^{ikj} a_j^\dagger/\sqrt{N}$ and $b_k^\dagger = \sum_{j=1}^N e^{ikj} b_j^\dagger/\sqrt{N}$, where $k = 2\pi n/N$ for $n \in (-N/2, N/2]$ within a lattice of cell size N, the effective Hamiltonian of the bath, $H_{\text{ssh}}^{\text{eff}}$, when moved to the momentum space, is expressed as $\sum_k \mathbf{o}_k^\dagger \tilde{\mathbf{h}}_k \mathbf{o}_k$ with

$$\tilde{\mathbf{h}}_k = \text{Re}\,[f_k]\,\sigma_x - \text{Im}\,[f_k]\,\sigma_y - i\kappa_-\sigma_z - i\kappa_+\sigma_0, \tag{3-5}$$

where $f_k = J_+ + J_- e^{-ik}$ is the coupling strength in the momentum space between the bosonic modes of a_k and b_k, and $\kappa_\pm = (\kappa_a \pm \kappa_b)/4$. In the subsequent discussions, we also set $\kappa_a = \kappa$ at odd sites (sublattice A) and $\kappa_b = 0$ at even (sublattice B). For H_{int}, by using the definitions of a_k and b_k, it is only necessary to transform $o_{x_{j,\alpha(\beta)}}(o_{x_{j,\alpha(\beta)}}^\dagger)$ into the momentum space. These operations yield a generalized non-Hermitian effective Hamiltonian in the momentum space. Appendix B.1 contains a full derivation of the setup. We emphasize that the bath, which is a topological waveguide, is described by two interspersed photonic lattices with alternating nearest-neighbor hopping $J_\pm = J(1 \pm \delta)$ between their bosonic modes, where J defines their strength, while δ, the so-called dimerization parameter, controls the asymmetry between them. When $\delta < 0$, the accompanying winding number equals one, and the bath supports topologically nontrivial phases, belonging to the Bott-Dummit-Iverson class in the topological classification of phase [222]. Conversely, when $\delta > 0$, the winding number is zero, corresponding to a topologically trivial phase. It is worth mentioning that the rotating wave approximation

is always applicable when both g and J are very small and comparable. The counter-rotating terms cannot be neglected when the strong coupling condition $g \gg \{J, \Delta\}$ is met. However, even considering the contribution of the counter-rotating wave, it only leads to more substantial dissipation, which does not affect the conclusions of work.

3.2.2 Dynamics

Let us move on to the study of the population dynamics of the quantum battery. Specifically, we focus on the nonunitary evolution $|\psi(t)\rangle = e^{-iH_{\text{eff}}t}|\psi(0)\rangle$ starting from the initial state, $|\psi(0)\rangle = |e, g; \text{vac}\rangle$ of the total system, for which the quantum charger is fully charged while the quantum battery is empty, where $|\text{vac}\rangle$ denotes the vacuum state of the lattice of bosonic modes. To analytically solve the dynamics of the quantum battery in this scenario, we assume that the bath is in the thermodynamic limit $(N \to \infty)$. By using the resolvent method [223, 224], the probability amplitude for the quantum battery to be excited at any time can be calculated

$$c_{\text{B}}(t) = \int_{\mathcal{C}} \frac{\mathrm{d}z}{2\pi i} \frac{\Sigma_{12}^{\alpha\beta}(z) + \Omega_{12}^{\alpha\beta}}{\mathscr{D}(z)} e^{-izt}, \tag{3-6}$$

where $\Sigma_{mn}^{\alpha\beta}(z) = \text{g}^2 G(x_{m,\alpha}, x_{n,\beta}; z)$ refers to the self-energy of the two-level systems. The detailed derivations of the self-energy can be found in Appendix B.2. The single-particle Green's function of the bath is denoted as

$$G(x_{m,\alpha}, x_{n,\beta}; z) = \langle \text{vac}| o_{x_{m,\alpha}} (z - \sum\nolimits_k \mathbf{o}_k^\dagger \tilde{\mathbf{h}}_k \mathbf{o}_k)^{-1} o_{x_{n,\beta}}^\dagger |\text{vac}\rangle, \tag{3-7}$$

and $\mathscr{D}(z) = [z - \Delta - \Sigma_{11}^{\alpha\alpha}(z)][z - \Delta - \Sigma_{22}^{\beta\beta}(z)] - [\Omega_{12}^{\alpha\beta} + \Sigma_{12}^{\alpha\beta}(z)]^2$.

3.2.3 Bound state

Now, we introduce the bound state, a critical "hidden" physical quantity impacting quantum-battery performance. By precisely solving the probability amplitude in Eq. (3-6), we find that the time evolution of the two-level systems is fully contributed by three parts, including bound-state energies, branch-cut detours, and unstable poles. Since the contributions from the branch-

cut detours and the unstable poles decay quickly over time, only the bound-state energies survive in the long-time limit, and we obtain

$$c_{\mathrm{B}}(\infty)=\sum_{z_k\in E_b}\mathrm{Res}\left[\frac{\Sigma_{12}^{\alpha\beta}(z)+\Omega_{12}^{\alpha\beta}}{\mathscr{D}(z)},z_k\right]e^{-iz_kt}, \tag{3-8}$$

where E_b represents the coherent bound-state energies [225], *i.e.*, the completely real eigenenergies of the bound states, which can be obtained by solving the real roots of the pole equation $\mathscr{D}(E_b)=0$, or equivalently, by imposing the eigenstate condition $H_{\mathrm{eff}}|\psi_b\rangle=E_b|\psi_b\rangle$. Henceforth, we denote the residue in Eq. (3-8) as $\mathrm{Res}(z_k)$, defined as $\mathrm{Res}[\{\Sigma_{12}^{\alpha\beta}(z)+\Omega_{12}^{\alpha\beta}\}/\mathscr{D}(z),z_k]$. Refer to Appendix B.3 for detailed derivations of Eq. (3-8).

We next undertake the task of characterizing various thermodynamic properties of quantum batteries. We initially introduce three crucial thermodynamic quantities essential for quantum battery performance evaluation: stored energy, ergotropy, and charging power. Subsequently, we explore how dissipation impacts quantum-battery performance under different configurations. Lastly, we confirm that with increasing dissipation, the emergence of the quantum Zeno effect significantly improves the short-time performance of the quantum battery.

3.3 Quantum battery performance

3.3.1 Performance indicators of quantum battery

To quantify the performance of quantum batteries, we introduce three thermodynamic indicators, starting with the stored energy. The energy of the quantum battery at time t is defined as

$$\mathcal{E}(t)=\mathrm{Tr}\left[\rho_{\mathrm{B}}(t)H_{\mathrm{B}}\right]=\omega_e|c_{\mathrm{B}}(t)|^2, \tag{3-9}$$

where $H_{\mathrm{B}}=\omega_e\sigma_+^{\mathrm{B}}\sigma_-^{\mathrm{B}}$ describes the Hamiltonian of the quantum battery with a characteristic frequency ω_e, while $\rho_{\mathrm{B}}(t)$ denotes the reduced density matrix of the quantum battery.

Based on the stored energy, we can define the second thermodynamic indicator, the charg-

ing power of the quantum battery, as $P(t) = \mathcal{E}(t)/t$, which we will discuss the related performance in 3.3.4.

The third key indicator is called the ergotropy, which is used to describe the maximum energy that can be extracted at time t, defined by

$$\mathcal{W}(t) = \mathrm{Tr}\left[\rho_{\mathrm{B}}(t) H_{\mathrm{B}}\right] - \mathrm{Tr}\left[\tilde{\rho}_{\mathrm{B}}(t) H_{\mathrm{B}}\right], \tag{3-10}$$

where $\tilde{\rho}_B(t) = \sum_s r_s(t) |\varepsilon_s\rangle \langle\varepsilon_s|$ is the passive state, $r_s(t)$ are the eigenvalues of $\rho_B(t)$ arranged in descending order, while $|\varepsilon_s\rangle$ are the eigenstates of H_B with the corresponding egienvalues ε_s sorted in ascending order.

3.3.2 Phase diagram of quantum battery

By substituting Eq. (3-8) into Eq. (3-9), we see that the stored energy of quantum battery in the long-time limit is only determined by the contributions of coherent bound-state energies. Thus, both the value of coherent bound-state energies and their corresponding residues are crucial for quantum battery performance. In Fig. 3.2(a) and Fig. 3.2(c), we observe that under resonance conditions ($\Delta = 0$), the maximum stored energy (MSE) of the quantum battery varies across different unit-cell distances d between the quantum charger and quantum battery, showing a singular behavior (derivative discontinuity) precisely at phase boundaries

$$\ell_1 : |\mathrm{g}| = 2J\sqrt{\frac{(-1)^{\Theta[d]}\delta(1-\delta^2)}{(2d+1)\delta - 1}}; \quad \ell_2 : |\mathrm{g}| = 2J\sqrt{\frac{(-1)^{\Theta[d]}(1-\delta^2)}{\delta - (2d+1)}}, \tag{3-11}$$

where $\Theta[d]$ is the Heaviside step function.

For detailed derivations of Eq. (3-11), see Appendix B.4.1. Specifically, this behavior originates from a jump in the number of bound states at the phase boundaries and a corresponding discontinuity in the residues of these states. However, despite the occurrence of such jumps at the topological phase boundary as well, the maximum stored energy remains continuous at the boundary [see the inserts in Fig. 3.2(c)] due to the vanishing residue of degenerate zero-energy bound states, as depicted by the middle black line in Fig. 3.2(b) and Fig. 3.2(d) for $\delta > 0$. Notably, we show that in the parameter region to the left of the phase boundary ℓ_1,

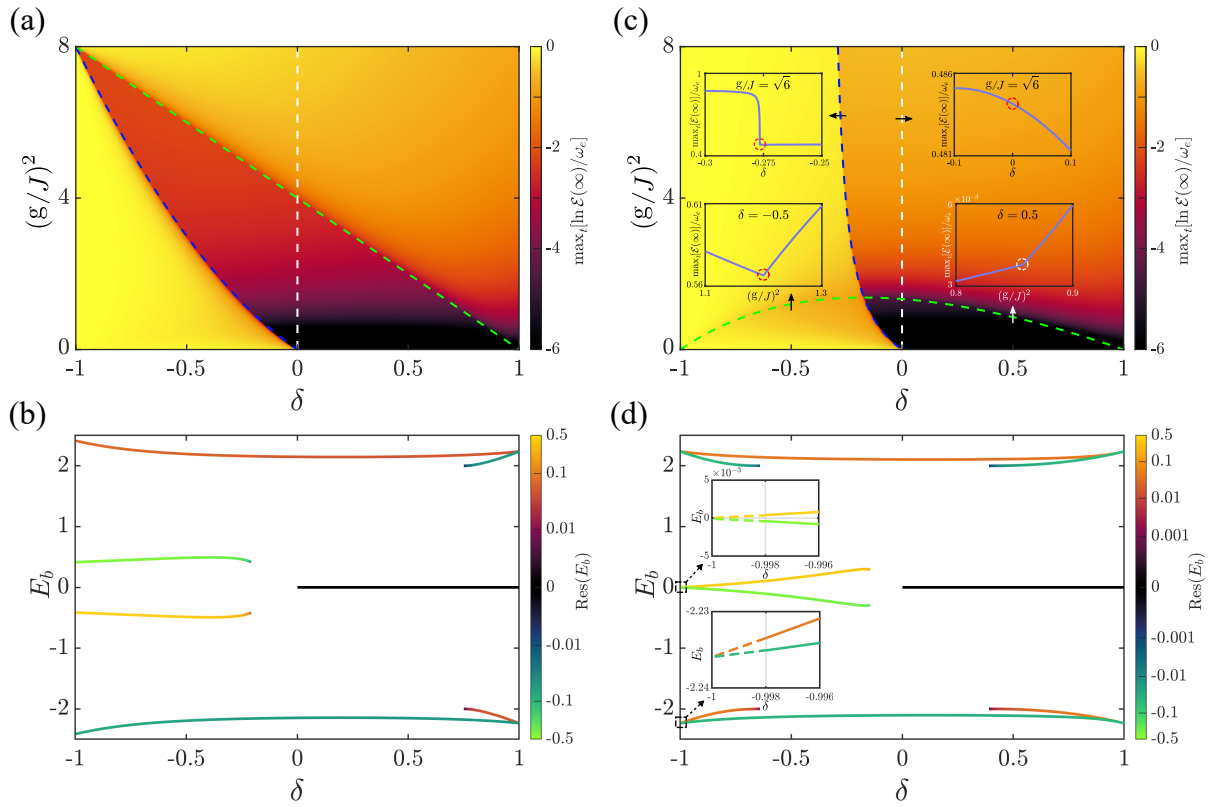

Figure 3.2: Panels (a) and (c) describe the maximum stored energy max $[\mathcal{E}(\infty)]$ as a function of the dimerization parameter δ and the atom-bath coupling strength g, for $d = -1$ and $d = -2$ respectively. The white dashed line represents the topological phase boundary of the bath $(\ell_0 : \delta = 0)$, while the blue and green dashed lines, ℓ_1 and ℓ_2, respectively, represent two phase boundaries of the maximum stored energy. In panel (c), the two insets at the bottom exhibit singular behavior (the derivative is discontinuous) of the maximum stored energy at $\delta = \pm 0.5$ upon crossing the phase boundary ℓ_2, which is indicated by the arrow. The same conclusion also appears at the phase boundary ℓ_1. Panels (b) and (d) show that the coherent bound-state energies varies with δ at different $d = -1$ and $d = -2$, respectively. Here, we set $g/J = 1$ for both panels (b) and (d). The residues at the coherent bound state energies are color-coded, facilitating observation of the contribution in Eq. (3-8) of these bound states. We choose $\kappa = 0$ in (a)-(d). For (a)-(d) the other parameters are chosen as $\Delta = 0$, $\alpha = B$, and $\beta = A$.

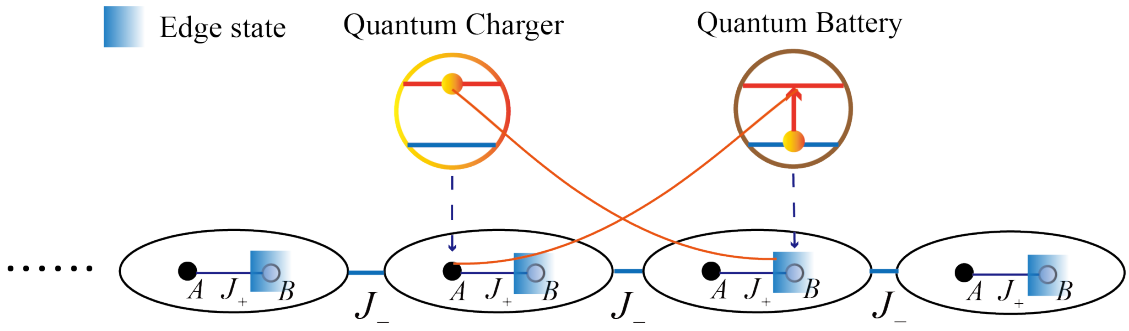

Figure 3.3: The optimal charging mechanism involves achieving the optimal energy transfer by placing the quantum charger and the quantum battery in different sublattices of distinct unit cells within a topologically nontrivial regime. In the topologically nontrivial phase, the bound states of two atoms have overlapping distributions. When a quantum charger is placed in sublattice A, the bound states emerge in sublattice B, allowing the quantum battery in sublattice B to be charged.

the majority of energy from the quantum charger is successfully transferred to the quantum battery. Conversely, to the right of this boundary, energy transmission is nearly completely obstructed. Additionally, we also observe that at $d = -1$ and $d = -2$, their intersection point of phase boundaries (ℓ_1 and ℓ_2) have shifted, thereby greatly expanding the parameter region for the optimal energy transmission, *i.e.*., the region to the left of phase boundary ℓ_1 where the intersection point can be obtained through Eq. (3-11). At the critical point $\delta = -1$ where the intracell hopping is absent, the quantum battery and the quantum charger become completely decoupled as long as $|d| > 1$, which results in a complete blockade of energy transfer from the quantum charger to the quantum battery. However, as δ approaches but does not reach the critical point, energy from the quantum charger can be transferred almost completely to the quantum battery, irrespective of the atom-bath interaction strength, as depicted in the insets of Fig. 3.2(d). To deepen physical intuition, Figure 3.3 shows that the distribution of the edge states is determined by the dimerization parameter δ and the placement of the atoms. Only when the quantum charger and quantum battery are placed in different sublattices and in a topologically non-trivial phase can photons be perfectly transmitted.

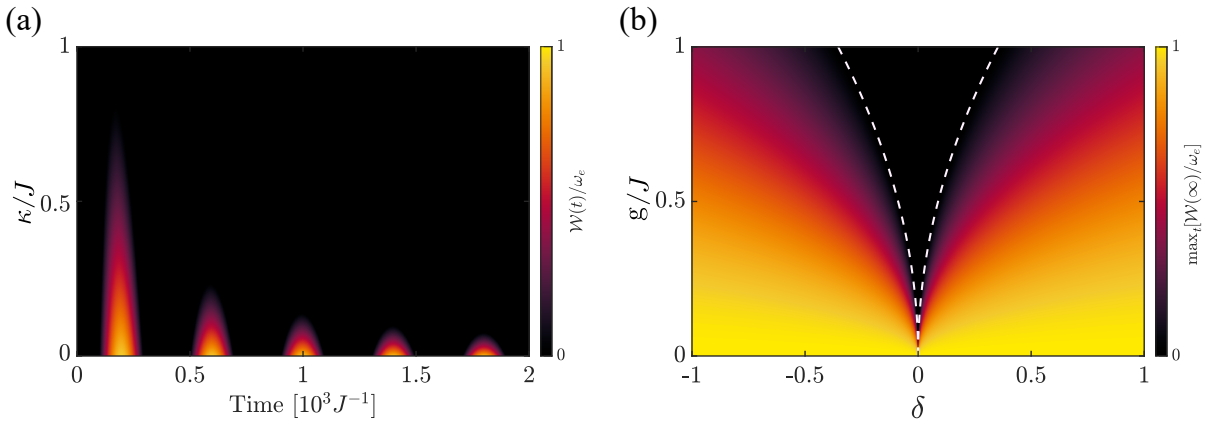

Figure 3.4: Panel (a) shows how dissipation κ affects the time-dependence of the ergotropy $\mathcal{W}(t)$ of the quantum battery varies over time with the other parameters set to $\mathrm{g}/J = 0.1$, $\delta = -0.26$, $\Delta = 0$, and $d = -1$. When the quantum charger and the quantum battery are placed in the same unit cell of the sublattice, the maximum ergotropy $\max_t[\mathcal{W}(\infty)]$ varies as a function of δ and g as shown in panel (b) with the other parameters set to $\Delta/J = -\Omega/J = 0.5$. The white dashed curve, defined by the equation $(\mathrm{g}/J)^2 = 2|\delta|\sqrt{2}$, depicts the boundaries where $\max_t[\mathcal{W}(\infty)] = 0$. Here, we set $\alpha = B$ and $\beta = A$ in (a), while in (b) both α and β set to A.

3.3.3 Dissipation immunity of quantum battery

As shown in Fig. 3.4(a), for $\Omega_{12}^{\alpha\beta} = 0$ (without direct coupling), we plot the ergotropy of the quantum battery (3-10) as a function of dissipation κ and time. We observe that dissipation causes a decrease in the ergotropy of a quantum battery and that increasing the dissipation rate further accelerates this decline. Specifically, when $\kappa > 0$, $\max_t[\mathcal{W}(\infty)] = 0$. For $\Omega_{12}^{\alpha\beta} \neq 0$, we are surprised to find that as long as the condition $\Delta = -\Omega$ is met, even if the direct coupling g between the quantum charger and the quantum battery is extremely weak, the quantum battery is still immune to direct dissipation $\kappa_a = \kappa$. This is evident from the analytical expression

$$\max_t[\mathcal{W}(\infty)] = \frac{\omega_e}{2}\frac{8J^4\delta^2 - \mathrm{g}^4}{\left(2J^2|\delta| + \mathrm{g}^2\right)^2}\Theta\left(2^{\frac{3}{4}}J\sqrt{|\delta|} - |\mathrm{g}|\right) \tag{3-12}$$

of the maximum ergotropy for $\Delta = -\Omega$ in the long-time limit, showing that it is independent of κ. This result is only applicable to topological waveguides. For detailed derivations of Eq. (3-12), see Appendix B.4.2.

Physically, we reveal that when the condition $\Delta - \Omega \neq 0$ is met, there always exists a superposition called the dark state [226]:

$$|\psi_{\text{dark}}\rangle = \frac{1}{\sqrt{2}} \left(|e, g\rangle - |g, e\rangle\right) \otimes |\text{vac}\rangle \,, \tag{3-13}$$

which decouple from the environment. Meanwhile, when the condition $\Delta + \Omega = 0$ also holds, we identify a hidden non-degenerate zero-energy bound state, termed a vacancy-like dressed bound state, also known as a topologically robust dressed bound state in the Su-Schrieffer-Heeger model, which enhances the ability of the system to resist dissipation [227]. Additionally, in practical physical systems, disorder is inevitable and has profound effects on the performance of quantum batteries. Notably, vacancy-like dressed bound states exhibit strong robustness against off-diagonal disorder that does not break sublattice chiral symmetry, directly resulting in ergotropy and demonstrating strong robustness to chiral-protected disorder. For a detailed analysis, see the appendix B.4.3.

For $\Omega_{12}^{\alpha\beta} \neq 0$, the maximum ergotropy $\max\left[\mathcal{W}\left(\infty\right)\right]$ as a function of δ and g as shown in Fig. 3.4(b). The white dashed curve, described by the equation $\left(\mathrm{g}/J\right)^2 = 2\left|\delta\right|\sqrt{2}$, represents the boundaries where $\max\left[\mathcal{W}\left(\infty\right)\right] = 0$. We observe that when $\Omega_{12}^{\alpha\beta} \neq 0$ but $\delta = 0$, the topological waveguide degenerates into a traditional waveguide, and the dissipation immunity of the quantum battery is destroyed. While $\Omega_{12}^{\alpha\beta} \neq 0$ and $\delta \neq 0$, as g/J decreases, we discern an increase in the maximum ergotropy, which indicates its sensitivity to the direct coupling strength between the quantum charger and the quantum battery.

3.3.4 Performance boost in short time of quantum battery

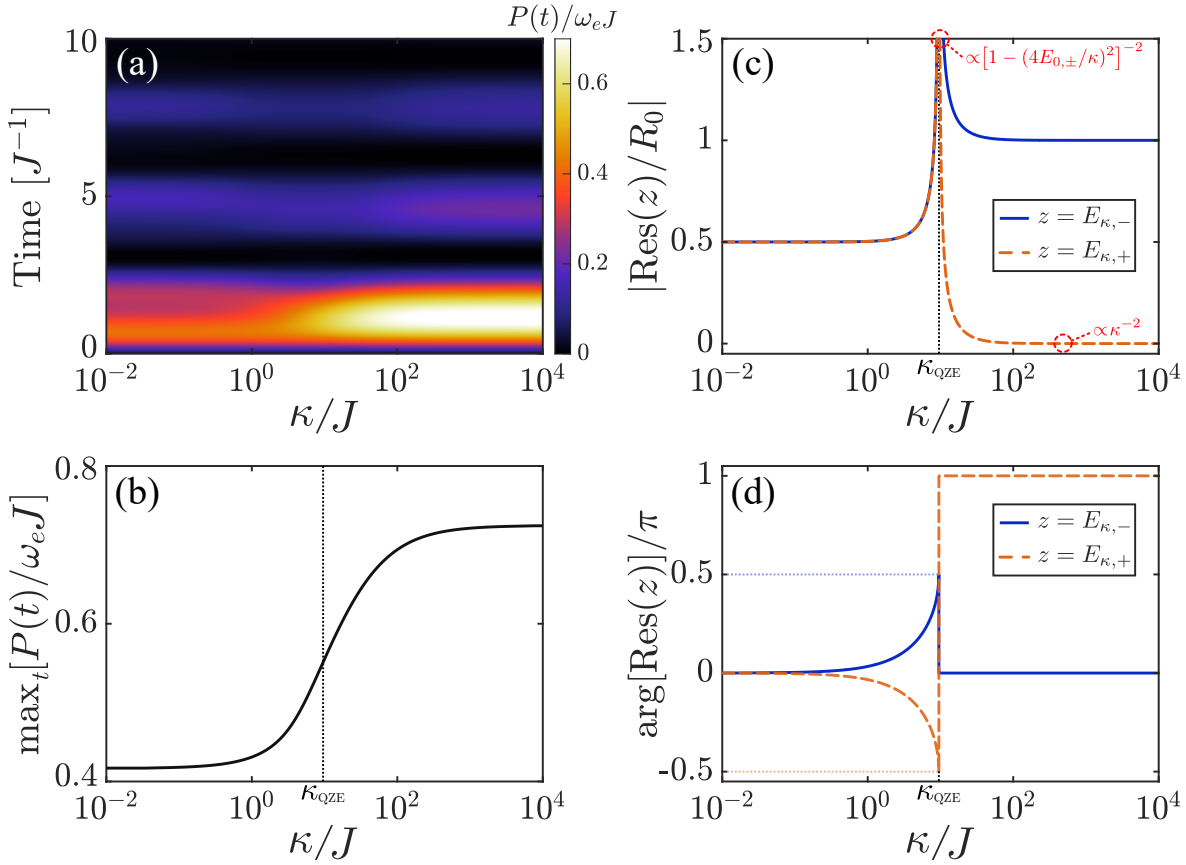

Figure 3.5: (a) Charging power $P(t)$ as a function of dissipation κ and time t. The corresponding maximum charging power $\max_t[P(t)]$ varies with κ as shown in (b). (c) and (d) respectively represent the modulus $|\mathrm{Res}(z)|$ and the phase $\arg[\mathrm{Res}(z)]$ of the residue at the dissipative bound-state energies $(E_{\kappa,\pm})$ as they vary with κ, which $E_{\kappa,-}$ and $E_{\kappa,+}$ are represented by the blue solid line and the orange dashed line, respectively. The critical point for the occurrence of the quantum Zeno effect is marked as κ_{QZE}. The parameters for (a) to (d) are chosen as $\Delta=-\Omega=J$, g/J $=1$, and $\delta=0.9$.

To assess the performance of quantum batteries, it is crucial to consider not only the stored energy and the ergotropy as key physical quantities but also the charging power as an indispensable indicator. Since the energy storage of a quantum battery composed of a two-level system is bounded, i.e., $0\leq\mathcal{E}(t)\leq\omega_e$, the charging power of quantum battery inevitably approaches zero in the long-time limit. Thus, discussions on the charging power of quantum batteries are primarily focused on short-time regions. Following the configuration of immu-

nity to dissipation over long-time limits, we are curious whether it is possible to enhance the charging power by utilizing dissipation in a short time. For $\Omega_{12}^{\alpha\beta} \neq 0$, the system is known to contain two states immune to dissipation, *i.e.*, a dark state and a vacancy-like dressed bound state. Furthermore, when the system is free from dissipation, two additional coherent bound states exist as well, whose energies are $E_{0,\pm} = \pm\sqrt{2J^2(1+\delta^2) + 2\sqrt{\mathrm{g}^4 + J^4(1-\delta)^2}}$. When dissipation is introduced, these two coherent bound states (*i.e.*, Im[E_i] = 0) transform into dissipative bound states (*i.e.*, Im[E_i] < 0) with imaginary energy less than zero, whose energies are

$$E_{\kappa,\pm} = -\frac{i}{4}\kappa \pm \sqrt{E_{0,\pm}^2 - \left(\frac{\kappa}{4}\right)^2}. \tag{3-14}$$

When $\kappa \gg \kappa_{\mathrm{QZE}} \equiv 4\left|E_{0,\pm}\right|$, we find a dramatic change in the lifetimes of the two dissipative bound states, *i.e.*, $\mathrm{Im}\left[E_{\kappa,+}\right] \propto -\kappa$ and $\mathrm{Im}\left[E_{\kappa,-}\right] \propto -1/\kappa$. Here, we note that the lifetime of the dissipative bound states with energy $E_{\kappa,-}$ is proportional to κ, and thus we may refer to this phenomenon as the quantum Zeno effect [228]. Simultaneously, their corresponding contribution to the residue is

$$\mathrm{Res}\left(E_{\kappa,+}\right) \approx \frac{-4R_0E_{0,\pm}^2}{\kappa^2}, \quad \mathrm{Res}\left(E_{\kappa,-}\right) \approx R_0, \tag{3-15}$$

where $R_0 = 2\mathrm{g}^4/\left\{\left[E_{0,\pm}^2 - 2J^2\left(1+\delta^2\right)\right]E_{0,\pm}^2\right\}$. From Eq. (3-15), we see that the contribution of Res $(E_{\kappa,+})$ significantly decreases as κ increases, while Res $(E_{\kappa,-})$ remains unchanged. According to Eq. (3-14), once κ exceeds κ_{QZE}, the energy of the dissipative bound states becomes purely imaginary. Furthermore, as κ increases, the imaginary parts of the energies of these two bound states exhibit opposite trends: one decreases while the other increases. Consequently, we refer to κ_{QZE} as the critical point where the quantum Zeno effect begins to emerge. In Fig. 3.5(c) and Fig. 3.5(d), we intuitively observe how both the modulus and the phase of Res $(E_{\kappa,\pm})$ vary with κ. In Fig. 3.5(a), we show that when κ is present, the charging power $P(t)$ exhibits a rapid periodic oscillatory decay over time. In a short time scale *i.e.*, $t \sim \pi/(2\left|\Omega\right|)$, increasing κ can be accompanied by enhancing $P(t)$. In Fig. 3.5(b), we observe that as κ continues to increase and goes beyond κ_{QZE}, the emergence of the quantum Zeno effect leads to a significant increase in $\max_t[P(t)]$. In addition, it is worth mentioning that if we observe the stroboscopic dynamics of the dissipative system at $t = (2\pi\mathbb{Z})/|E_{0,\pm}|$, we should find it nearly identical to the dynamics of a non-dissipative system. The detailed derivations in the

subsection 3.3.4 can be found in Appendix B.4.4.

3.4 Summary and prospect

To summarize, we have developed a general framework for analyzing the atomic dynamics of a battery-charger system comprised of two atoms coupled to a general bath. In particular, in the single-excitation sector, we have considered a typical one-dimensional lattice exhibiting topological properties as an environment, known as the Su-Schrieffer-Heeger model.

In the long-time limit, we have demonstrated that only the contributions from coherent bound state energies are retained. We have pointed out that in a topologically trivial phase, the zero-energy bound states exhibit twofold degeneracy at resonance, which results in the maximum stored energy approaching zero. In contrast, the maximum stored energy approaches one in a topologically nontrivial phase, which means that the quantum charger almost completely transfers energy to the quantum battery. Moreover, we discover that the maximum stored energy exhibits singular behavior at the phase boundary. We have also observed that the phase diagrams have shown significant differences for different unit cell distances between the quantum charger and the quantum battery.

Furthermore, we have discussed the performance of quantum batteries under different configurations. We discovered that when two directly coupled atoms are placed within the same cavity, the ergotropy is protected from the direct impact of sublattice dissipation due to the presence of a dark state and a vacancy-like dressed bound state. This configuration overcomes the environment-induced decoherence that causes energy loss and aging in quantum batteries. Intriguingly, we have also demonstrated that with the increase in dissipation, the emergence of the quantum Zeno effect significantly enhances the short-time performance of the quantum battery.

A significant issue is to further explore the performance of quantum batteries in generalized open quantum systems. As a concrete example, we will consider a one-dimensional tight-binding model with asymmetric hopping as an environment, investigating the performance of non-Hermitian quantum batteries through the perspective of the Hatano-Nelson model [229]. It would also be intriguing to understand the implicit relation between non-Markovian effects

and the alterations in the phase boundary curves within our phase diagram. One may also be interested in extending the study of quantum batteries to multi-excitation scenarios as another direction for future research. Specifically, it would be valuable to investigate the performance of multi-excitation [230, 231] using numerical techniques such as matrix product states [232] or hierarchical equations of motion analogs [233].

Appendix B

Appendix for Chapter 3

This Appendix contains four parts. B.1 and B.2: Exact dynamics of a quantum charger and quantum battery coupled to a structured bosonic environment; B.3: The dynamics of a quantum battery in a topological environment; B.4: Quantum battery performance in different configurations.

B.1 The dynamics of a quantum battery in a topological bath

In Appendix B.1, we show the full derivation of the setup in Sec. 3.2.1. We explore the dynamics of a quantum battery in a topological environment, both with and without dissipation. We begin with a detailed discussion of the topological environment in subsections B.1.1 and B.1.2. Next, we derive an analytical expression for self-energy in the dissipative topological environment and demonstrate the connection between bound state energies and the long-term behavior of the quantum battery dynamics.

B.1.1 Su-Schrieffer-Heeger model without dissipation

We choose the simplest topological model, the non-dissipative Su-Schrieffer-Heeger model, as a topological environment. For simplicity, we employ two abbreviations $o_{x_{j,A}} \equiv a_{x_j}$ and

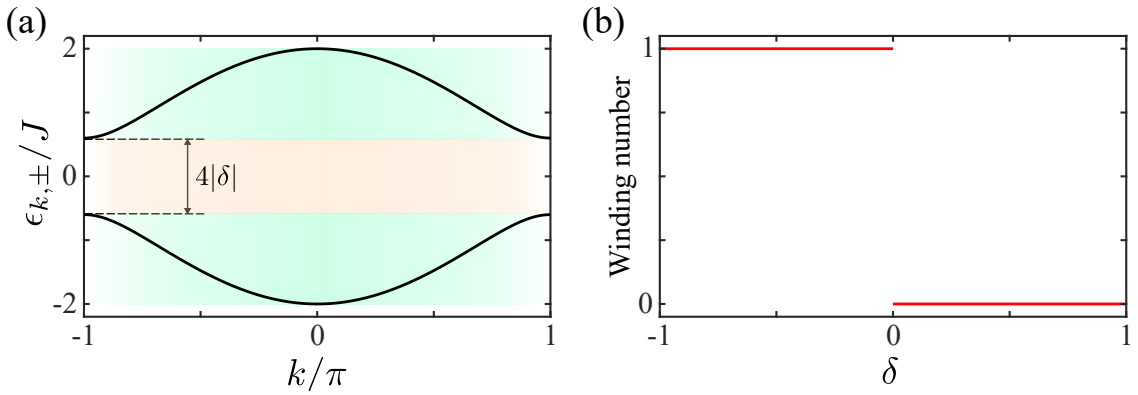

Figure B.1: (a) Dispersion relations $\epsilon_{k,\pm}$ of the Su-Schrieffer-Heeger environment with periodical boundary conditions. The parameter is set to $|\delta| = 0.3$. (b) The winding number as function of the dimerization strength δ. When $\delta < 0$, the model is in a topologically nontrivial phase with a winding number of one. Conversely, when $\delta > 0$, the model is in a topologically trivial phase with a winding number of zero.

$o_{x_{j,\mathrm{B}}} \equiv b_{x_j}$. By setting $\hbar = 1$, the Hamiltonian of the topological environment is given by

$$H_{\mathrm{ssh}} = \sum_{j=1}^{N} \omega_c \left(a_j^\dagger a_j + b_j^\dagger b_j \right) + J_+ \sum_{j=1}^{N} \left(a_j^\dagger b_j + b_j^\dagger a_j \right) + J_- \sum_{j=1}^{N} \left(b_j^\dagger a_{j+1} + a_{j+1}^\dagger b_j \right), \quad \text{(B-1)}$$

where a_j ($a_j^\dagger$) and b_j ($b_j^\dagger$) are the annihilation (creation) operators of boson on the sites a and b at position j, respectively. The resonant frequency of these bosonic modes is ω_c. The topological waveguide consists of two interspersed photonic lattices with alternating nearest-neighbor hopping $J_\pm = J\,(1 \pm \delta)$ between bosonic modes. Here, J defines the hopping strength, while δ, known as the dimerization parameter, controls the asymmetry between the lattices. Under the periodic boundary condition (*i.e.* $a_{N+j} = a_j$ and $b_{N+j} = b_j$) and in the momentum space with

$$a_k^\dagger = \frac{1}{\sqrt{N}} \sum_{j=1}^{N} e^{ikj} a_j^\dagger, \quad b_k^\dagger = \frac{1}{\sqrt{N}} \sum_{j=1}^{N} e^{ikj} b_j^\dagger, \quad k = \frac{2\pi n}{N}, \quad \text{(B-2)}$$

where $n \in (-N/2, N/2]$, we have the environment Hamiltonian in the momentum space as $H_{\mathrm{ssh}} = \sum_k \mathbf{o}_k^\dagger \mathbf{h}_k \mathbf{o}_k$, with $\mathbf{o}_k = [a_k, b_k]^T$, and the corresponding Bloch Hamiltonian reads

$$\mathbf{h}_k = \begin{bmatrix} \omega_c & f_k \\ f_k^* & \omega_c \end{bmatrix} = \mathrm{Re}[f_k]\sigma_x - \mathrm{Im}[f_k]\sigma_y + \omega_c \sigma_0, \quad \text{(B-3)}$$

where $f_k = J(1+\delta) + J(1-\delta)e^{-ik} \equiv \omega_k e^{i\phi_k}$ (with $\omega_k > 0$) is the coupling coefficient in the momentum space between the bosonic modes of a_k and b_k. Hereafter, we set ω_c as the energy reference. By simply diagonalizing $\mathbf{h}_k$, the Hamiltonian H_{ssh} in Eq. (B-1) can be written as

$$H_{\text{ssh}} = \sum_k \begin{bmatrix} u_k^\dagger & l_k^\dagger \end{bmatrix} \begin{bmatrix} \omega_k & 0 \\ 0 & -\omega_k \end{bmatrix} \begin{bmatrix} u_k \\ l_k \end{bmatrix} = \sum_k [\omega_k u_k^\dagger u_k - \omega_k l_k^\dagger l_k], \tag{B-4}$$

where $u_k/l_k = (\pm a_k + b_k e^{i\phi_k})/\sqrt{2}$, $\omega_k = J\sqrt{2(1+\delta^2) + 2(1-\delta^2)\cos(k)}$, and $\phi_k = \arctan$ $[\text{Im}(f_k)/\,\text{Re}(f_k)]$. The corresponding dispersion relations are given by $\epsilon_{k,\pm} = \pm\omega_k$, where the subscript $+$ $(-)$ denotes the upper (lower) energy band of the Su-Schrieffer-Heeger environment.

In Fig. B.1(a), we present the dispersion relation for a dimerization parameter $|\delta| = 0.3$. The energy bands of the bath are observed to be symmetric with respect to the cavity resonant frequency ω_c. The energy bands span the range $[-2J, -2\,|\delta|\,J] \cup [2\,|\delta|\,J, 2J]$, featuring a central bandgap of $4\,|\delta|\,J$. These energy bands can be adjusted by varying the dimerization strength δ. In the Su-Schrieffer-Heeger model, the topological properties of the system are characterized by the winding number, which takes values of either one or zero, depending on the parameters of the system. In Fig. B.1(b), we depict the winding number of the Su-Schrieffer-Heeger bath. In the case in which the intracell hopping strength outweighs the intercell hopping strength (*i.e.* $\delta > 0$), the winding number equals to zero, corresponding to the so-called topologically trivial phase. Conversely, when the intercell hopping strength dominates over the intracell hopping strength (*i.e.* $\delta < 0$), the winding number is one, indicating a topologically nontrivial phase.

B.1.2 Su-Schrieffer-Heeger model with dissipation

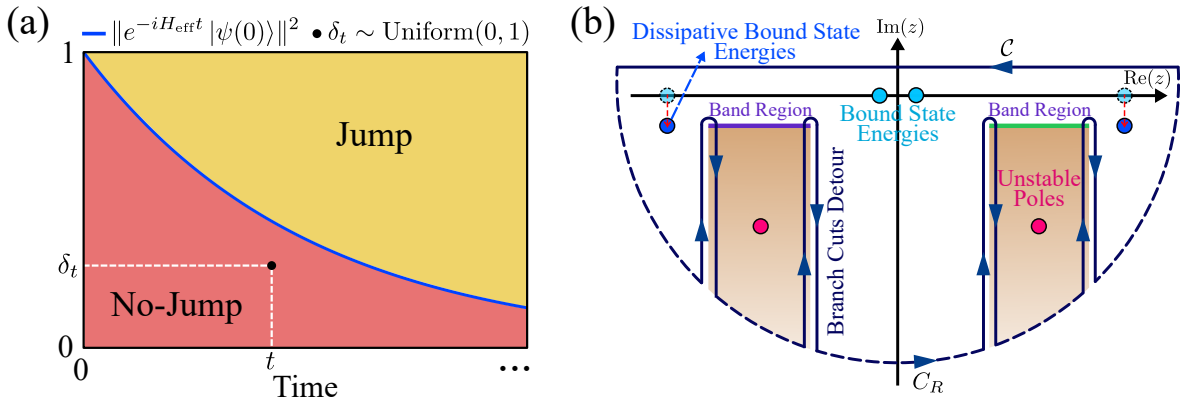

Figure B.2: (a) The norm squared of the evolved state governed by the effective non-Hermitian Hamiltonian H_{eff} as a function of time. For a single trajectory, the occurrence of a quantum jump at time t can be determined by comparing a random number δ_t with the norm squared at that time, as indicated by the black dot falling within the red region. (b) An integration contour (horizontal dark blue line) to calculate Eq. (3-6). One needs to close the contour of integration in the lower half of the complex plane (dashed and vertical dark blue line) in evaluating the integration. Here, the information including dissipative bound-state energies, branch-cuts detour, and unstable poles, within the lower half of the complex plane is given by the effective non-Hermitian Hamiltonian described by Subsection B.1.2. At the band edges the path changes from the first to the second Riemann sheet of the integrand $\mathscr{C}(z)$ (brown areas).

Let us consider a realistic scenario: a one-dimensional Su-Schrieffer-Heeger photonic lattice with engineered photon loss. Under the Born-Markov and rotating-wave approximations, the equation of motion takes the form of Eq. (3-1), where H_{sys}, H_{ssh}, and H_{int} are given by Eqs. (3-2)-(3-4). Here, the photon dissipators of different sublattices are given by $\mathcal{L}_a = \kappa_a \sum_j \mathcal{D}[a_j]$ and $\mathcal{L}_b = \kappa_b \sum_j \mathcal{D}[b_j]$, where κ_a (κ_b) control the photon loss rates of sublattice A (B), and $\mathcal{D}[L]\rho = L\rho L^\dagger - \{L^\dagger L, \rho\}/2$ is the Lindblad superoperator.

To find the solution to Eq. (3-1) in the single-excitation sector, we rewrite the Lindblad master equation (3-1) as

$$\dot{\rho}_t = -i(H_{\text{eff}}\rho_t - \rho_t H_{\text{eff}}^\dagger) + \kappa_a \sum_{j=1}^{N} a_j \rho_t a_j^\dagger + \kappa_b \sum_{j=1}^{N} b_j \rho_t b_j^\dagger, \tag{B-5}$$

where a_j and b_j within the last two terms are the "jump" operators associated with the lattice dissipation resulting from emission into free space, and H_{eff} is the effective non-Hermitian Hamiltonian for the dissipative system, *i.e.* $H_{\text{eff}} = H_{\text{sys}} + H_{\text{ssh}}^{\text{eff}} + H_{\text{int}}$ with $H_{\text{ssh}}^{\text{eff}} = H_{\text{ssh}} - (i/2)\sum_j(\kappa_a a_j^\dagger a_j + \kappa_b b_j^\dagger b_j)$. In this form, the terms $\kappa_a \sum_j a_j \rho_t a_j^\dagger$ and $\kappa_b \sum_j b_j \rho_t b_j^\dagger$ are often called the recycling terms, as it recycles the population that is lost from certain states due to the effective non-Hermitian Hamiltonian, placing it in other states. For the initial state $|\psi(0)\rangle$ in the single-excitation subspace, on the one hand, the time evolution under the effective non-Hermitian Hamiltonian is given by $|\psi(t)\rangle = e^{-iH_{\text{eff}}t}|\psi(0)\rangle$, resulting in a non-normalized final state with a norm squared that monotonically decreases over time, as shown by the blue line in Fig. B.2(a). On the other hand, once the recycling terms work, *i.e.* when a jump process occurs, the final state deterministically transitions to the zero-excitation state $|g, g; \text{vac}\rangle$. According to the quantum trajectory method, whether a jump process occurs at time t is determined by comparing a random number δ_t between zero and one with the norm squared $\langle\psi(t) \mid \psi(t)\rangle = \left\| e^{-iH_{\text{eff}}t}|\psi(0)\rangle \right\|^2$. Specifically, if $\delta_t > \langle\psi(t)|\psi(t)\rangle$, the jump occurs; otherwise, it does not, as illustrated by the red and yellow regions in Fig. B.2(a).

Then, we focus on the state at time t and generate N random numbers uniformly distributed between zero and one. For the sake of simplicity, we define N_1 and N_2 as the counts of no-jump and jump occurrences, respectively, where $N_1 + N_2 = N$ is satisfied. As a result, because of the condition for the occurrence of jumps, the solution to Eq. (3-1) reads

$$\rho_t = \lim_{N\to\infty} \frac{|\tilde{\psi}(t)\rangle\langle\tilde{\psi}(t)| \times N_1 + |g, g; \text{vac}\rangle\langle g, g; \text{vac}| \times N_2}{N}, \tag{B-6}$$

where $|\tilde{\psi}(t)\rangle = |\psi(t)\rangle/\sqrt{\langle\psi(t) \mid \psi(t)\rangle}$ represents the normalized state. Provided our random number generators are well-behaved, these two ratios should satisfy

$$\lim_{N\to\infty} \frac{N_1}{N} = \langle\psi(t)|\psi(t)\rangle\,, \quad \lim_{N\to\infty} \frac{N_2}{N} = 1 - \lim_{N\to\infty} \frac{N_1}{N} = 1 - \langle\psi(t)|\psi(t)\rangle = p_t. \tag{B-7}$$

Finally, by plugging Eq. (B-7) into Eq. (B-6), we have

$$\rho_t = |\psi(t)\rangle\langle\psi(t)| + p_t\,|g, g; \text{vac}\rangle\langle g, g; \text{vac}| = e^{-iH_{\text{eff}}t}\rho_0 e^{iH_{\text{eff}}^\dagger t} + p_t\,|g, g; \text{vac}\rangle\langle g, g; \text{vac}|\,. \tag{B-8}$$

If the initial state is a mixed state ρ_0, the norm squared $\langle\psi(t)|\psi(t)\rangle$ mentioned above should

be rewritten as $\mathrm{Tr}[e^{-iH_{\mathrm{eff}}t}\rho_0 e^{iH_{\mathrm{eff}}^{\dagger}t}]$. Notice that $\mathrm{Tr}[e^{-iH_{\mathrm{eff}}t}\rho_0 e^{iH_{\mathrm{eff}}^{\dagger}t}] = \langle\psi(t)|\psi(t)\rangle$ when $\rho_0 = |\psi(0)\rangle\langle\psi(0)|$. In fact, when we replace the total Hamiltonian H_{tot} in Eq. (1.10) with the effective non-Hermitian Hamiltonian H_{eff}, *i.e.* $H_{\mathrm{ssh}} \to H_{\mathrm{ssh}}^{\mathrm{eff}}$, the derivation procedures from Eq. (1.10) to $\rho_{\mathrm{B}}(t)$ remain valid.

Therefore, we focus on studying the effective non-Hermitian Hamiltonian when we restrict ourselves to the single-excitation subspace. Following Eqs. (B-1)-(B-4), we express the corresponding non-Hermitian Bloch Hamiltonian as

$$\tilde{\mathbf{h}}_k = \begin{bmatrix} -i\kappa_a/2 & f_k \\ f_k^* & -i\kappa_b/2 \end{bmatrix} = \mathrm{Re}[f_k]\sigma_x - \mathrm{Im}[f_k]\sigma_y - i\kappa_-\sigma_z - i\kappa_+\sigma_0, \tag{B-9}$$

whose energy dispersion reads $\tilde{\epsilon}_{k,\pm} = -i\kappa_+ \pm \tilde{\omega}_k$, where $\tilde{\omega}_k = \omega_k^2 - \kappa_-^2$ and $\kappa_\pm = (\kappa_a \pm \kappa_b)/4$. Remarkably, we find that the system exhibits a passive parity-time ($\mathcal{PT}$) symmetry in the form of $\sigma_x\big(\tilde{\mathbf{h}}_k + i\kappa_+\sigma_0\big)^*\sigma_x = \tilde{\mathbf{h}}_k + i\kappa_+\sigma_0$ and has two exceptional points (EPs) at $k_{\mathrm{EP}} = \pm\arccos[(\kappa_-^2 - 2J^2(1+\delta^2))/(2J^2(1-\delta^2))]$ in the Brillouin zone for $|\delta| \le |\kappa_-/(2J)| < 1$. Then, by diagonalizing $\tilde{\mathbf{h}}_k$, the effective non-Hermitian Hamiltonian $H_{\mathrm{ssh}}^{\mathrm{eff}}$ in Eq. (B-5) can be further written as

$$H_{\mathrm{ssh}}^{\mathrm{eff}} = \sum_k \begin{bmatrix} u_{k,L}^{\dagger} & l_{k,L}^{\dagger} \end{bmatrix} \begin{bmatrix} \tilde{\epsilon}_{k,+} & 0 \\ 0 & \tilde{\epsilon}_{k,-} \end{bmatrix} \begin{bmatrix} u_{k,R} \\ l_{k,R} \end{bmatrix} = \sum_k [\tilde{\epsilon}_{k,+} u_{k,L}^{\dagger} u_{k,R} + \tilde{\epsilon}_{k,-} l_{k,L}^{\dagger} l_{k,R}] \tag{B-10}$$

with

$$u_{k,L}^{\dagger}/l_{k,L}^{\dagger} = \frac{1}{\sqrt{2}}\left[\pm a_k^{\dagger} + \frac{\tilde{\omega}_k \pm i\kappa_-}{\omega_k e^{i\phi_k}} b_k\right], u_{k,R}/l_{k,R} = \frac{1}{\sqrt{2}}\left[\frac{\pm\tilde{\omega}_k - i\kappa_-}{\tilde{\omega}_k} a_k + \frac{\omega_k e^{i\phi_k}}{\tilde{\omega}_k} b_k\right], \tag{B-11}$$

which satisfy $u_{k,R} = u_{k,L} = u_k$, $l_{k,R} = l_{k,L} = l_k$, and $\tilde{\epsilon}_{k,\pm} = \epsilon_{k,\pm}$ when $\kappa_a = \kappa_b = 0$.

B.2 The calculation of self-energy in the dissipative topological environment

To evaluate the integral (3-6), the quantity (1.16), referred to as the self-energies of two quantum emitters, require further computation. By setting $\kappa_a = \kappa_b = 0$, the dissipative envi-

ronment can be reduced to a non-dissipative environment. For the sake of generality, we compute the self-energy directly within a dissipative topological environment. Firstly, we transform Q in Eq. (1.11) into momentum space, *i.e.*

$$\begin{aligned} Q &= |g,g\rangle\langle g,g| \otimes \sum_j (a_j^\dagger \,|\text{vac}\rangle\langle\text{vac}|\, a_j + b_j^\dagger \,|\text{vac}\rangle\langle\text{vac}|\, b_j) \\ &= |g,g\rangle\langle g,g| \otimes \sum_k \left(|u_{k,L}\rangle\langle u_{k,R}| + |l_{k,L}\rangle\langle l_{k,R}|\right), \end{aligned} \tag{B-12}$$

where $|u_{k,L}\rangle = u_{k,L}^\dagger\,|\text{vac}\rangle$, $|l_{k,L}\rangle = l_{k,L}^\dagger\,|\text{vac}\rangle$, $\langle u_{k,R}| = \langle\text{vac}|\,u_{k,R}$, and $\langle l_{k,R}| = \langle\text{vac}|\,l_{k,R}$, which satisfy $\langle u_{k,R}|u_{k',L}\rangle = \langle l_{k,R}|l_{k',L}\rangle = \delta_{k,k'}$ and $\langle u_{k,R}|l_{k',L}\rangle = \langle l_{k,R}|u_{k',L}\rangle = 0$. For the sake of simplicity, we define $\tilde{Q} = \sum_k \left(|u_{k,L}\rangle\langle u_{k,R}| + |l_{k,L}\rangle\langle l_{k,R}|\right)$. According to Eqs. (1.16), (B-2), (B-10), and (B-12), we have

$$\begin{aligned} G(x_{1,\alpha}, x_{2,\beta}; z) =& \ \langle\text{vac}|o_{x_{1,\alpha}}(z - H_{\text{ssh}}^{\text{eff}})^{-1} o_{x_{2,\beta}}^\dagger|\text{vac}\rangle = \langle\text{vac}|o_{x_{1,\alpha}}\tilde{Q}(z - H_{\text{ssh}}^{\text{eff}})^{-1}\tilde{Q}o_{x_{2,\beta}}^\dagger|\text{vac}\rangle \\ =& \ \langle\text{vac}|o_{x_{1,\alpha}} \sum_k \left[\frac{|u_{k,L}\rangle\langle u_{k,R}|}{z + i\kappa_+ - \tilde{\omega}_k} + \frac{|l_{k,L}\rangle\langle l_{k,R}|}{z + i\kappa_+ + \tilde{\omega}_k}\right] o_{x_{2,\beta}}^\dagger|\text{vac}\rangle\,. \end{aligned} \tag{B-13}$$

For $\alpha = \beta = A$, according to Eq. (B-11), Eq. (B-13) can be further written as

$$\begin{aligned} G(x_{1,A}, x_{2,A}; z) &= \frac{1}{N}\sum_{k,k',k''} e^{ik'x_1 - ik''x_2} \langle\text{vac}|a_{k'} \left[\frac{|u_{k,L}\rangle\langle u_{k,R}|}{z + i\kappa_+ - \tilde{\omega}_k} + \frac{|l_{k,L}\rangle\langle l_{k,R}|}{z + i\kappa_+ + \tilde{\omega}_k}\right] a_{k''}^\dagger|\text{vac}\rangle \\ &= \frac{1}{2N}\sum_{k,k',k''} e^{ik'x_1 - ik''x_2} \left[\frac{\tilde{\omega}_{k''} - i\kappa_-}{z + i\kappa_+ - \tilde{\omega}_k} + \frac{\tilde{\omega}_{k''} + i\kappa_-}{z + i\kappa_+ + \tilde{\omega}_k}\right] \frac{\delta_{k,k'}\delta_{k,k''}}{\tilde{\omega}_{k''}} \\ &= \frac{1}{N}\sum_k \frac{(z + i\kappa_b/2)e^{ik(x_1 - x_2)}}{z_{\text{nh}}^2 - \omega_k^2} = \int_{-\pi}^{\pi} \frac{\mathrm{d}k}{2\pi} \frac{(z + i\kappa_b/2)e^{ik(x_1 - x_2)}}{z_{\text{nh}}^2 - \omega_k^2}, \end{aligned} \tag{B-14}$$

where $z_{\text{nh}}^2 = (z + i\kappa_+)^2 + \kappa_-^2$. Similarly, for $\alpha = \beta = B$, we have

$$G(x_{1,B}, x_{2,B}; z) = \frac{1}{N}\sum_k \frac{(z + i\kappa_a/2)e^{ik(x_1 - x_2)}}{z_{\text{nh}}^2 - \omega_k^2} = \int_{-\pi}^{\pi} \frac{\mathrm{d}k}{2\pi} \frac{(z + i\kappa_a/2)e^{ik(x_1 - x_2)}}{z_{\text{nh}}^2 - \omega_k^2}, \tag{B-15}$$

whereas for other cases of α and β, we have

$$G(x_{1,A}, x_{2,B}; z) = \int_{-\pi}^{\pi} \frac{\mathrm{d}k}{2\pi} \frac{\omega_k e^{ik(x_1 - x_2) + i\phi_k}}{z_{\text{nh}}^2 - \omega_k^2}, \tag{B-16}$$

$$G(x_{1,B}, x_{2,A}; z) = \int_{-\pi}^{\pi} \frac{\mathrm{d}k}{2\pi} \frac{\omega_k e^{ik(x_1 - x_2) - i\phi_k}}{z_{\text{nh}}^2 - \omega_k^2}. \tag{B-17}$$

By substituting the given dispersion relation, these two integrals in Eqs. (B-14)-(B-15) can be evaluated as

$$\begin{aligned} G(x_{1,A}, x_{2,A}; z) &= \int_{-\pi}^{\pi} \frac{\mathrm{d}k}{2\pi} \frac{(z + i\kappa_b/2) e^{ik(x_1 - x_2)}}{z_{\text{nh}}^2 - J^2[2(1+\delta^2) + 2(1-\delta^2)\cos(k)]} \\ &= \oint_{|y|=1} \frac{\mathrm{d}y}{2\pi i} \frac{(z + i\kappa_b/2) y^{x_1 - x_2}}{J^2(\delta^2 - 1)(y^2 + 1) + [z_{\text{nh}}^2 - 2J^2(1+\delta^2)]y} \\ &= -\frac{(z + i\kappa_b/2) \sum_{p=\pm} p \tilde{y}_p^{|x_1 - x_2|} \Theta[p(1 - |\tilde{y}_+|)]}{\sqrt{z_{\text{nh}}^4 - 4J^2 z_{\text{nh}}^2 (1+\delta^2) + 16 J^4 \delta^2}} = G(x_{2,A}, x_{1,A}; z), \end{aligned} \tag{B-18}$$

$$\begin{aligned} G(x_{1,B}, x_{2,B}; z) &= \int_{-\pi}^{\pi} \frac{\mathrm{d}k}{2\pi} \frac{(z + i\kappa_a/2) e^{ik(x_1 - x_2)}}{z_{\text{nh}}^2 - J^2[2(1+\delta^2) + 2(1-\delta^2)\cos(k)]} \\ &= \oint_{|y|=1} \frac{\mathrm{d}y}{2\pi i} \frac{(z + i\kappa_a/2) y^{x_1 - x_2}}{J^2(\delta^2 - 1)(y^2 + 1) + [z_{\text{nh}}^2 - 2J^2(1+\delta^2)]y} \\ &= -\frac{(z + i\kappa_a/2) \sum_{p=\pm} p \tilde{y}_p^{|x_1 - x_2|} \Theta[p(1 - |\tilde{y}_+|)]}{\sqrt{z_{\text{nh}}^4 - 4J^2 z_{\text{nh}}^2 (1+\delta^2) + 16 J^4 \delta^2}} = G(x_{2,B}, x_{1,B}; z), \end{aligned} \tag{B-19}$$

where

$$\tilde{y}_\pm = \frac{z_{\text{nh}}^2 - 2J^2(1+\delta^2) \pm \sqrt{z_{\text{nh}}^4 - 4J^2 z_{\text{nh}}^2 (1+\delta^2) + 16 J^4 \delta^2}}{2J^2(1-\delta^2)}, \ \Theta[x] = \begin{cases} 1 & x \geq 0 \\ 0 & x < 0 \end{cases}. \tag{B-20}$$

Given $f_k = \omega_k e^{i\phi_k}$ and $f_k^* = \omega_k e^{-i\phi_k}$, the integrals in Eqs. (B-16)-(B-17) are evaluated as:

$$\begin{aligned} G(x_{1,A}, x_{2,B}; z) &= \int_{-\pi}^{\pi} \frac{\mathrm{d}k}{2\pi} \frac{J[1 + \delta + (1-\delta)e^{-ik}] e^{ik(x_1 - x_2)}}{z_{\text{nh}}^2 - J^2[2(1+\delta^2) + 2(1-\delta^2)\cos(k)]} \\ &= \oint_{|y|=1} \frac{\mathrm{d}y}{2\pi i} \frac{J[(1+\delta) y^{x_1 - x_2} + (1-\delta) y^{x_1 - x_2 - 1}]}{z_{\text{nh}}^2 - J^2[2(1+\delta^2) + 2(1-\delta^2)\cos(k)]} \\ &= -\frac{J \sum_{p=\pm} p F_{x_1 - x_2}(\tilde{y}_p, \delta) \Theta[p(1 - |\tilde{y}_+|)]}{\sqrt{z_{\text{nh}}^4 - 4J^2 z_{\text{nh}}^2 (1+\delta^2) + 16 J^4 \delta^2}} = G(x_{2,B}, x_{1,A}; z), \end{aligned} \tag{B-21}$$

$$\begin{aligned} G(x_{1,B}, x_{2,A}; z) &= \int_{-\pi}^{\pi} \frac{\mathrm{d}k}{2\pi} \frac{J[1 + \delta + (1-\delta)e^{ik}] e^{ik(x_1 - x_2)}}{z_{\text{nh}}^2 - J^2[2(1+\delta^2) + 2(1-\delta^2)\cos(k)]} \\ &= \oint_{|y|=1} \frac{\mathrm{d}y}{2\pi i} \frac{J[(1+\delta) y^{x_1 - x_2} + (1-\delta) y^{x_1 - x_2 + 1}]}{z_{\text{nh}}^2 - J^2[2(1+\delta^2) + 2(1-\delta^2)\cos(k)]} \\ &= -\frac{J \sum_{p=\pm} p F_{x_1 - x_2 + 1}(\tilde{y}_p, -\delta) \Theta[p(1 - |\tilde{y}_+|)]}{\sqrt{z_{\text{nh}}^4 - 4J^2 z_{\text{nh}}^2 (1+\delta^2) + 16 J^4 \delta^2}} = G(x_{2,A}, x_{1,B}; z), \end{aligned} \tag{B-22}$$

where $F_d(\tilde{y}_p, \delta) = (1+\delta)\tilde{y}_p^{|d|} + (1-\delta)\tilde{y}_p^{|d-1|}$.

B.3 The calculation of the probability amplitude for a quantum battery

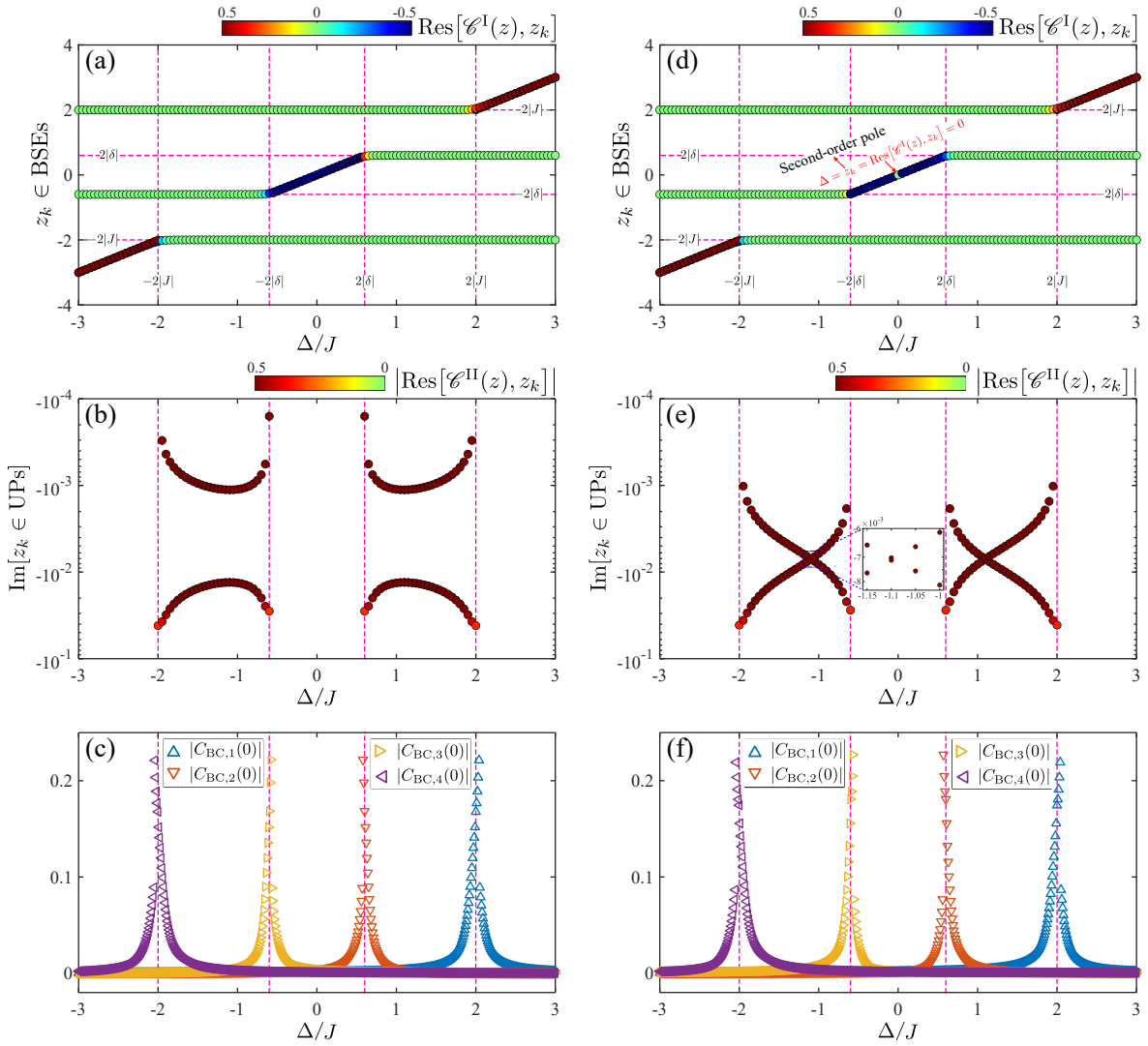

Figure B.3: First row (a)-(c): topologically nontrivial phase ($\delta = -0.3$). Second row (d)-(f): topologically trivial phase ($\delta = 0.3$). Panels (a) and (d) describe the bound-state energies z_k and its corresponding residue $\mathrm{Res}[\mathscr{C}^{\mathrm{I}}(z), z_k]$ as a function of the emitter detuning Δ. Panels (b) and (e) describe the imaginary part of the unstable poles $\mathrm{Im}[z_k]$ and the absolute value of its corresponding residue $\left|\mathrm{Res}[\mathscr{C}^{\mathrm{II}}(z), z_k]\right|$ as a function of the emitter detuning Δ. Panels (c) and (f) describe the contributions at time $t = 0$ of the branch-cut detours $C_{\mathrm{BC},k}(0)$ as a function of the emitter detuning Δ. The system parameters are $\mathrm{g}/J = 0.1$, $\alpha = B$, $\beta = A$, and $d = x_1 - x_2 = -1$.

To further obtain the dynamics of quantum battery, *i.e.* calculating the integral in Eq. (3-6), we employ residue integration by closing the contour in the lower half of the complex plane, as illustrated in Fig. B.1(b). Since the presence of sublattice dissipation makes the distribution of band regions (namely branch cuts) in the complex plane exceedingly intricate in certain cases, the following calculations will focus solely on the non-dissipative Su-Schrieffer-Heeger environment (see subsection. B.1.1). Accordingly, Fig. B.1(b) should be slightly modified for the non-dissipative environment as follows: (i) Dissipative bound-state energies should be replaced by bound-state energies; (ii) The band regions should be shifted to the real axis, Re$[z]$.

Now, let us focus on the integral in Eq. (3-6) and its integrand. Since the integrand has branch cuts in the real axis along the regions (*i.e.* $z \in [-2J, -2|\delta|] \cup [2|\delta|, 2J]$), where bands of the topological environment are defined (the continuous spectrum of H_{tot}), it is necessary to detour at the band edges to other Riemann sheets of the integrand, as shown in Fig. B.1(b). For convenience, we use the symbol $\mathscr{C}(z)$ to represent the integrand excluding the term $\exp(-izt)$. The analytical expressions for the self-energies presented in Eqs.(B-18), (B-19), (B-21), and (B-22) correspond to the integrand in the first Riemann sheet $\mathscr{C}^{\text{I}}(z)$. We can analytically continue it to the second Riemann sheet $\mathscr{C}^{\text{II}}(z)$ (brown areas) by simply replacing $\Theta[p(\cdots)]$ with $\Theta[-p(\cdots)]$ in the expressions of the self-energies. As a result, the integrand in the first and second Riemann sheets is given by

$$\mathscr{C}^{\text{I/II}}(z) = \frac{\mathrm{g}^2 G^{\text{I/II}}(x_{1,\alpha}, x_{2,\beta}; z) + \Omega_{12}^{\alpha\beta}}{\mathscr{D}^{\text{I/II}}(z)} \tag{B-23}$$

with

$$G^{\text{I/II}}(x_{1,A}, x_{2,A}; z) = -\frac{z \sum_{p=\pm} p y_p^{|x_1 - x_2|} \Theta[\pm p(1 - |y_+|)]}{\sqrt{z^4 - 4J^2 z^2 (1+\delta^2) + 16 J^4 \delta^2}} = G^{\text{I/II}}(x_{1,B}, x_{2,B}; z), \tag{B-24}$$

$$G^{\text{I/II}}(x_{1,A}, x_{2,B}; z) = -\frac{J \sum_{p=\pm} p F_{x_1 - x_2}(y_p, \delta) \Theta[\pm p(1 - |y_+|)]}{\sqrt{z^4 - 4J^2 z^2 (1+\delta^2) + 16 J^4 \delta^2}}, \tag{B-25}$$

where $y_\pm = \tilde{y}_\pm|_{z_{\text{nh}} \to z}$ represents non-dissipative environment. Here, since $\Sigma_{11}^{\alpha\alpha}(z) = \Sigma_{11}^{\beta\beta}(z)$ and $\Sigma_{12}^{\alpha\beta}(z) = \Sigma_{21}^{\beta\alpha}(z)$, the denominator in Eq. (B-23) can be further simplified as

$$\mathscr{D}^{\text{I/II}}(z) = [z - \Delta - \mathrm{g}^2 G^{\text{I/II}}(x_{1,\alpha}, x_{1,\alpha}; z)]^2 - [\Omega_{12}^{\alpha\beta} + \mathrm{g}^2 G^{\text{I/II}}(x_{1.\alpha}, x_{2,\beta}; z)]^2, \tag{B-26}$$

where $\Delta = \omega_e - \omega_c$ is the emitter detuning.

On one hand, since the imaginary part of $\mathscr{C}^{\mathrm{I}}(z+i0^{+})$ and $\mathscr{C}^{\mathrm{II}}(z-i0^{+})$ is nonzero in the band regions, we should only take into account the real poles (*i.e.* the roots of $\mathscr{D}^{\mathrm{I}}(z)=0$) of $\mathscr{C}^{\mathrm{I}}(z)$ outside the band regions, corresponding to the bound-state energies (BSEs), and the complex poles (*i.e.* the roots of $\mathscr{D}^{\mathrm{II}}(z)=0$) of $\mathscr{C}^{\mathrm{II}}(z)$ with real part inside band regions, corresponding to the unstable poles (UPs). On the other hand, aside from the integral path $\mathcal{C}$ (which corresponds to Eq. (3-6)) and the semicircular path C_R (which vanished as the radius of the semicircle approaches infinity, according to Jordan's lemma), we need to add eight additional integral paths again parallel to the imaginary axis, corresponding to the branch-cut detours (BCDs), so that these paths form a closed loop on the complex plane, as shown in Fig. B.2(b). According to the residue theorem, the sum of the contributions from these paths should equal the sum of the residues at the aforementioned poles. Thus, we have

$$c_{\mathrm{B}}(t)=\sum_{z_k\in\mathrm{BSEs}}\mathrm{Res}\big[\mathscr{C}^{\mathrm{I}}(z),z_k\big]e^{-iz_kt}+\sum_{z_k\in\mathrm{UPs}}\mathrm{Res}\big[\mathscr{C}^{\mathrm{II}}(z),z_k\big]e^{-iz_kt}+\sum_{k=1}^{4}C_{\mathrm{BC},k}(t). \quad \text{(B-27)}$$

The last term in Eq. (B-27) represents the contributions of the branch-cut detours, which can be computed as

$$C_{\mathrm{BC},k}(t)=(-1)^{k-1}\int_0^{\infty}\frac{\mathrm{d}y}{2\pi}\left[\mathscr{D}^{\mathrm{I}}(c_k-iy)-\mathscr{D}^{\mathrm{II}}(c_k-iy)\right]e^{-ic_kt-yt}, \quad \text{(B-28)}$$

where $c_1=2J, c_2=2\left|\delta\right|, c_3=-2\left|\delta\right|$, and $c_4=-2J$. Based on the form of Eq. (B-27), we find that the quantum bound dynamics are fully described by the contributions from bound-state energies, unstable poles, and the branch-cut detours. Given that the integrand in Eq. (B-28) contains $\exp(-yt)$ with $y\geq 0$, the contribution from the branch-cut detours diminishes as time passes. Furthermore, because the imaginary parts of the UPs are negative, their contribution also decays over time. Therefore, only the bound-state contributions survive in the long-time limit $t\gg 1/\mathrm{g}$, *i.e.*

$$c_{\mathrm{B}}(\infty)\equiv\lim_{t\gg 1/\mathrm{g}}c_{\mathrm{B}}(t)=\sum_{z_k\in\mathrm{BSEs}}\mathrm{Res}\big[\mathscr{C}^{\mathrm{I}}(z),z_k\big]e^{-iz_kt}. \quad \text{(B-29)}$$

Next, we demonstrate how the residues of the bound-state energies, the absolute values of the residues of the unstable poles, and the contributions of branch-cut detours vary with the emitter detuning Δ in both the topologically trivial and non-trivial phases. First, as shown in

Figs. B.3(a) and B.3(d), for topologically trivial and non-trivial phases, the number of bound states and the corresponding residues varies with detuning in the same way, except at zero detuning. Particularly at zero detuning, in the topologically non-trivial phase, the two non-zero bound-state energies (their residues are close to ± 0.5, respectively), which are opposite in sign, will merge into a degenerate zero-energy bound state, its residue approaching to zero. Moreover, the contribution of bound-state energies becomes most significant only when the detuning falls within the bandgap, and the number of bound states also increases by one compared to those within the bands, except at $\Delta = 0$ in the topologically trivial phase. Second, as shown in Figs. B.3(b) and B.3(e), unstable poles appear in pairs only when the detuning is within the bands, and the effective dissipation (*i.e.* $-\mathrm{Im}[z_k]$) is significantly enhanced in the topologically trivial phase compared to the topologically non-trivial phase. Finally, as shown in Figs. B.3(c) and B.3(f), the contribution from branch-cut detours at time $t = 0$ is almost identical in both topologically trivial and non-trivial phases and is most significant when the detuning is near the band edges.

B.4 Quantum battery performance in different configurations

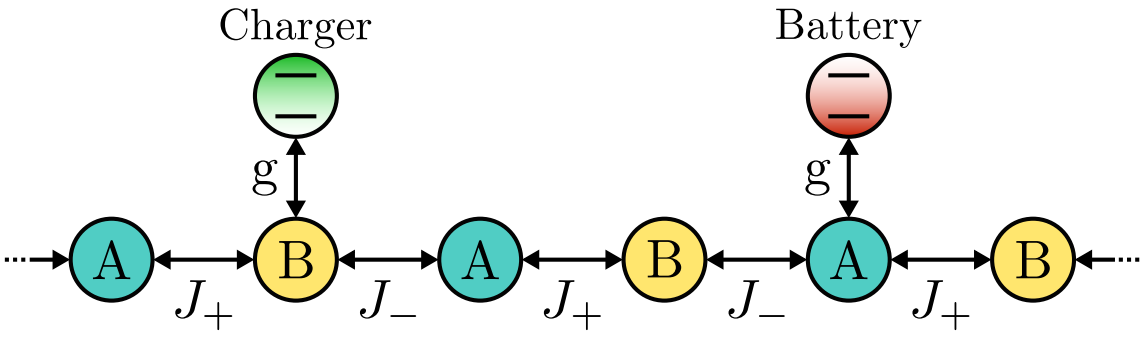

Figure B.4: Configuration-I: The quantum charger and the quantum battery are located in different sublattices, *i.e.* $x_{1,\alpha} = x_{1,B}$ and $x_{2,\beta} = x_{2,A}$, which indicates that the quantum charger and the quantum battery are not directly coupled, *i.e.*, $\Omega_{12}^{\alpha\beta} = 0$.

To support the phase boundaries outlined in Eq. (3-11) and the maximum stored energy described in Eq. (3-12) of Chapter 3, we provide detailed derivations and discussions in the

following subsections: Subsection B.4.1 covers the phase diagram of quantum battery, Subsection B.4.2 addresses the dissipation immunity of quantum battery, and Subsection B.4.3 demonstrates how environmental dissipation can be utilized to enhance quantum battery performance over a short time.

B.4.1 Phase diagram of quantum battery

Here, the definition of the stored energy for the quantum battery is given by $\mathcal{E}(t) = \mathrm{Tr}[\rho_{\mathrm{B}}(t)H_{\mathrm{B}}]$, where $H_{\mathrm{B}} = \omega_e \sigma_+^{\mathrm{B}}\sigma_-^{\mathrm{B}}$ and $\rho_{\mathrm{B}}(t)$ are the free Hamiltonian and the reduced density matrix of quantum battery, respectively. For a general system described in subsection 1, the reduced density matrix of the quantum battery can be obtained from the steps of Eqs. (1.10)-(1.19). Then, by substituting Eq. (1.19) into $\mathcal{E}\,(t)$, the stored energy of quantum battery is simplified to $\mathcal{E}(t) = \omega_e \left|c_{\mathrm{B}}(t)\right|^2$. The calculation of the stored energy of the quantum battery is thus reduced to calculating the probability amplitude. According to Eq. (B-29), we know that in the long-time limit, only the bound states contribute to the probability amplitude. Therefore, to obtain the maximum stored energy $\max[\mathcal{E}(\infty)]$, we need to find the poles of the integrand in Eq. (1.19) in the band-gap regime (*i.e.* the bound-state energies) by solving the pole equation $\mathscr{D}(E_i)$:

$$[E_i - \Delta - \Sigma_{11}^{\alpha\alpha}(E_i)][E_i - \Delta - \Sigma_{22}^{\beta\beta}(E_i)] - [\Omega_{12}^{\alpha\beta} + \Sigma_{12}^{\alpha\beta}(E_i)][\Omega_{12}^{\alpha\beta} + \Sigma_{21}^{\beta\alpha}(E_i)] = 0. \quad \text{(B-30)}$$

Subsequently, we focus solely on the system presented in Fig. 3.2(a)-(d) of Chapter 3. The corresponding total Hamiltonian is denoted as

$$H_{\mathrm{tot}} = \frac{\omega_e}{2}\sigma_z^{\mathrm{B}} + \frac{\omega_e}{2}\sigma_z^{\mathrm{C}} + H_{\mathrm{ssh}} + \mathrm{g}(\sigma_+^{\mathrm{B}} o_{x_{1,B}} + \sigma_+^{\mathrm{C}} o_{x_{2,A}} + \mathrm{H.c.}), \quad \text{(B-31)}$$

where H_{ssh} is given by Eq. (B-1). For simplicity, we assume that the quantum charger is always positioned on the left side of the quantum battery, which implies $d = x_1 - x_2 \in \mathbb{Z}^-$. According to these expressions of the self-energies in Eqs. (B-18), (B-19), (B-21), and (B-22) without environmental dissipation (*i.e.* $\kappa_a = \kappa_b = 0$), the pole equation (B-30) can be further simplified

as

$$\begin{aligned}\mathscr{D}(E_i) &= [E_i - \Delta - \mathrm{g}^2 G(x_{1,B}, x_{1,B}; E_i)]^2 - [\mathrm{g}^2 G(x_{1,B}, x_{2,A}; E_i)]^2 \\ &= \mathrm{g}^4 \prod_{p=\pm} [(E_i - \Delta)/\mathrm{g}^2 + G_p(E_i)] = 0,\end{aligned} \tag{B-32}$$

where

$$\begin{aligned}G_{\pm}(E_i) &= [G(x_{1,B}, x_{1,B}; E_i) \pm G(x_{1,B}, x_{2,A}; E_i)] \\ &= -\frac{\sum_{p=\pm}[z \pm J F_{d+1}(y_p, -\delta)] p \Theta[p(1 - |y_+|)]}{\sqrt{z^4 - 4J^2 z^2 (1+\delta^2) + 16 J^4 \delta^2}}\Bigg|_{z=E_i},\end{aligned} \tag{B-33}$$

which satisfies $G_{\pm}(E_i) = -G_{\mp}(-E_i)$ since both $y_{\pm}$ are even functions with respect to z.

To solve this pole equation, we first need to analyze the characteristics of $G_{\pm}(E_i)$ within the band-gap region and at the band edges. This analysis will help us determine the number of intersection points between $G_{\pm}(E_i)$ and $(E_i - \Delta)/\mathrm{g}^2$, *i.e.* the number of bound states. For simplicity, we divide the bandgap into three intervals, *i.e.* $\mathcal{R}_l = (-\infty, -2J)$, $\mathcal{R}_m = (-2J\,|\delta|\,, 2J\,|\delta|)$, and $\mathcal{R}_r = (2J, +\infty)$. It is not difficult to observe that when $z \in \mathcal{R}_m$, $-1 < y_+ < 0$; while when $z \in \mathcal{R}_l \cup \mathcal{R}_r$, $y_+ > 1$.

First, we will start our analysis with the middle region of the bandgap $\mathcal{R}_m$, and we have

$$\begin{aligned}G_{\pm}(z) &= \frac{-[z \pm J F_{d+1}(y_+, -\delta)]}{\sqrt{z^4 - 4J^2 z^2 (1+\delta^2) + 16 J^4 \delta^2}} = -\frac{z \pm J[(1-\delta) y_+^{|d+1|} + (1+\delta) y_+^{|d|}]}{\sqrt{z^4 - 4J^2 z^2 (1+\delta^2) + 16 J^4 \delta^2}} \\ &= -G_{\mp}(-z), \quad z \in \mathcal{R}_m.\end{aligned} \tag{B-34}$$

According to Eq. (B-34), we only need to analyze the behavior of $G_+(z)$ because G_+ and G_- are mutually symmetric with respect to the ordinate origin, as shown in Figs. B.5(a) and B.5(c). Additionally, we find that $G_+(z)$ is a monotonic function with respect to z in the interval $\mathcal{R}_m$, *i.e.* $[\mathrm{d}G_+/\mathrm{d}z]|_{z \in \mathcal{R}_m} < 0$. Finally, determining whether the number of bound states can be changed abruptly depends on the behavior (divergence or convergence) of $G_{\pm}(z)$ at the band edges. As $z \to \pm 2J\,|\delta|$, the denominator of $G_{\pm}(z)$ evidently approaches zero with a behavior proportional to $\sqrt{2J\,|\delta| \pm z}$. Thus, we only need to analyze the Taylor expansion

of $F_{d+1}(y_+, -\delta)$ at $z = \pm 2J\,|\delta|$, *i.e.*,

$$F_{d+1}(y_+, -\delta)|_{z=\pm 2J|\delta|} = 2(-1)^d\{\delta - \sqrt{\frac{|\delta|\,/J}{1-\delta^2}}[\delta(|d|+|d+1|)+|d|-|d+1|](2J\,|\delta| \pm z)^{\frac{1}{2}}\} + o[(2J\,|\delta| \pm z)^{\frac{1}{2}}]. \tag{B-35}$$

By plugging Eq. (B-35) into $G_+(z)$ in Eq. (B-34), we have

$$\lim_{z\to\pm 2J|\delta|} G_+(z) = \frac{-1}{2J\sqrt{1-\delta^2}} \lim_{z\to\pm 2J|\delta|} \frac{z + 2J(-1)^d\delta}{\sqrt{4J^2\delta^2 - z^2}} + \mathcal{G}_1(d,\delta), \tag{B-36}$$

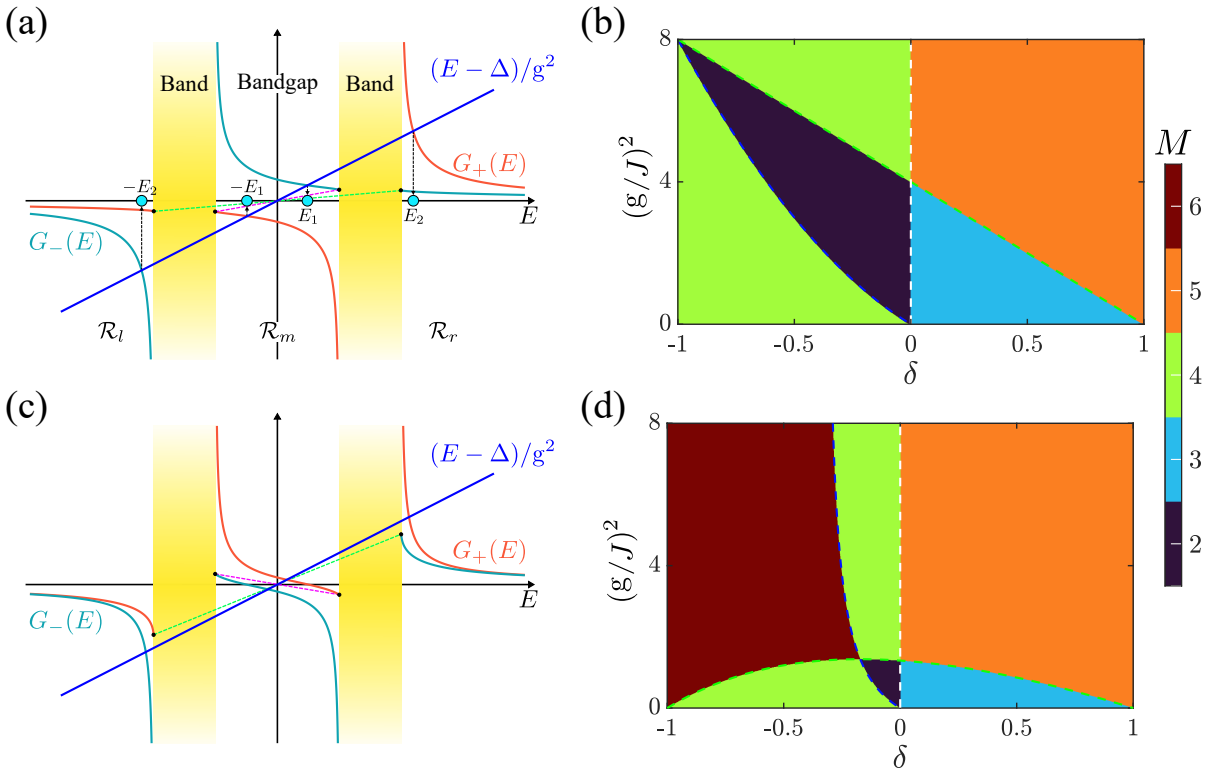

Figure B.5: Panels (a) and (c) describe the difference $G_\pm(E)$ as a function of E in the Su-Schrieffer-Heeger environment for $d = -1$ and $d = -2$ respectively. Roots of the poles equation (*i.e.* the BSEs) are obtained from the intersection points between $(E-\Delta)/g^2$ (blue solid line) and $G_\pm(E)$ (teal and orange solid lines). Panels (b) and (d) show the number of bound states M as a function of the dimerization parameter δ and the atom-bath coupling strength g for $d = -1$ and $d = -2$ respectively. The blue and green dashed lines are given by Eqs. (B-49)-(B-50). Here, we focus on a non-dissipative environment, *i.e.* $\kappa_a = \kappa_b = 0$.

where, for later convenience, we define

$$\mathcal{G}_1(d,\delta)=\frac{(-1)^{d+\Theta[d]}}{2J(1-\delta^2)}[1-(2d+1)\delta]. \tag{B-37}$$

For the first term on the right-hand side of Eq. (B-36), it is evident that different values of d and δ yield distinctly different results, *i.e.*

$$\lim_{z\to -2J|\delta|}\frac{z+2J(-1)^d\delta}{\sqrt{4J^2\delta^2-z^2}}=\begin{cases}-\infty & \text{if} \quad \Theta[(-1)^d\delta]=0,\\ 0 & \text{if} \quad \Theta[(-1)^d\delta]=1,\end{cases} \tag{B-38}$$

$$\lim_{z\to 2J|\delta|}\frac{z+2J(-1)^d\delta}{\sqrt{4J^2\delta^2-z^2}}=\begin{cases}0 & \text{if} \quad \Theta[(-1)^d\delta]=0,\\ +\infty & \text{if} \quad \Theta[(-1)^d\delta]=1,\end{cases} \tag{B-40}$$

which result in

$$\lim_{z\to -2J|\delta|}G_+(z)=\begin{cases}+\infty & \text{if} \quad \Theta[(-1)^d\delta]=0,\\ \mathcal{G}_1(d,\delta) & \text{if} \quad \Theta[(-1)^d\delta]=1,\end{cases} \tag{B-41}$$

$$\lim_{z\to 2J|\delta|}G_+(z)=\begin{cases}\mathcal{G}_1(d,\delta) & \text{if} \quad \Theta[(-1)^d\delta]=0,\\ -\infty & \text{if} \quad \Theta[(-1)^d\delta]=1.\end{cases} \tag{B-42}$$

In addition, the difference $G_+(z)-G_-(z)$ also plays an important role in the analysis of the aforementioned intersection points. According to $\max(y_+)=y_+|_{z=0}=[(\delta-1)/(\delta+1)]^{\text{sign}(\delta)}$ and Eq. (B-34), the difference is computed as

$$\begin{aligned}G_+(z)-G_-(z)=G_+(z)+G_+(-z)&=\frac{-2J[(1-\delta)y_+^{|d+1|}+(1+\delta)y_+^{|d|}]}{\sqrt{z^4-4J^2z^2(1+\delta^2)+16J^4\delta^2}}\\ &=\begin{cases}2J(1+\delta)y_+^{|d+1|}[\max{(y_+)}^{\text{sign}(\delta)}-y_+] & \text{for} \quad d\le -1,\\ 2J(1-\delta)y_+^{|d|}[\max{(y_+)}^{\text{sign}(-\delta)}-y_+] & \text{for} \quad d\ge 0.\end{cases}\end{aligned} \tag{B-43}$$

For given parameters δ and d, within the band-gap region $\mathcal{R}_m$, $G_+(z)$ is consistently positioned either entirely above or entirely below $G_-(z)$, and these two functions have a unique intersection point [i,e., $G_+(0)=G_-(0)=0$] only when $d\le -1\wedge\delta>0$ or $d\ge 0\wedge\delta<0$.

Second, for the other two band-gap regions $\mathcal{R}_l$ and $\mathcal{R}_r$, we also have

$$G_{\pm}(z) = \frac{z \pm JF_{d+1}(y_-, -\delta)}{\sqrt{z^4 - 4J^2z^2(1+\delta^2) + 16J^4\delta^2}} = \frac{z \pm J[(1-\delta)y_-^{|d+1|} + (1+\delta)y_-^{|d|}]}{\sqrt{z^4 - 4J^2z^2(1+\delta^2) + 16J^4\delta^2}}, \quad \text{(B-44)}$$

where $z \in \mathcal{R}_l \cup \mathcal{R}_r$. Similarly, we only need to analyze the behavior of $G_{\pm}(z)$ in one of these regions due to $G_{\pm}(z) = -G_{\mp}(-z)$. As a consequence, we focus on the case of $z \in \mathcal{R}_r$. We find that $G_{\pm}(z)$ both are a monotonic function in the interval $\mathcal{R}_l$, *i.e.* $[\mathrm{d}G_{\pm}/\mathrm{d}z]|_{z\in\mathcal{R}_r} < 0$, and the difference $G_+(z) - G_-(z)$ is always more than zero, *i.e.* $G_+(z) > G_-(z)$ for $z \in \mathcal{R}_r$. It is evident that when $z \to +\infty$, $G_{\pm}(z)$ both approach zero. As $z \to 2J$, the denominator of $G_{\pm}(z)$ evidently approaches zero with a behavior proportional to $\sqrt{z-2J}$. Thus, the Taylor expansion of $F_{d+1}(y_-, -\delta)$ at $z = 2J$ is given by

$$\begin{aligned} F_{d+1}(y_-, -\delta)|_{z=2J} = 2 - \frac{2[\delta(|d| - |d+1|) + |d| + |d+1|]}{\sqrt{J(1-\delta^2)}}(z-2J)^{\frac{1}{2}} \\ + o[(z-2J)^{\frac{1}{2}}]. \end{aligned} \quad \text{(B-45)}$$

By plugging Eq. (B-45) into $G_{\pm}(z)$ of Eq. (B-44), we have

$$\lim_{z\to 2J} G_+(z) = +\infty, \quad \lim_{z\to 2J} G_-(z) = \mathcal{G}_2(d,\delta) \equiv \frac{(-1)^{\Theta[d]}[\delta - (2d+1)]}{2J(1-\delta^2)} > 0. \quad \text{(B-46)}$$

As shown in Figs. B.5(a) and B.5(c), for $\Delta = 0$, we find that the critical point, where the number of intersection points (bound state energies) between $(E-\Delta)/\mathrm{g}^2$ and $G_{\pm}(E)$ undergoes an abrupt change, occurs when the slope of the blue solid line equals the slopes of the pink or green dashed lines. For the pink dashed line within the bandgap $\mathcal{R}_m$, according to Eqs. (B-41)-(B-42), its slope is given by

$$k_1 = (-1)^{\Theta[(-1)^d\delta]} \frac{\mathcal{G}_1(d,\delta) - [-\mathcal{G}_1(d,\delta)]}{2J\,|\delta| - [-2J\,|\delta|]} = \frac{(-1)^{\Theta[d]}[(2d+1)\delta - 1]}{4J^2\delta(1-\delta^2)}. \quad \text{(B-47)}$$

Similarly, for the green dashed line, according to Eq. (B-46), its slope is given by

$$k_2 = \frac{\mathcal{G}_2(d,\delta) - [-\mathcal{G}_2(d,\delta)]}{2J - [-2J]} = \frac{(-1)^{\Theta[d]}[\delta - (2d+1)]}{4J^2(1-\delta^2)}. \quad \text{(B-48)}$$

Thus, the two-phase boundaries are given by

$$\ell_1:\ k_1=\frac{1}{\mathrm{g}^2}\Longrightarrow|\mathrm{g}|=2J\sqrt{\frac{(-1)^{\Theta[d]}\delta(1-\delta^2)}{(2d+1)\delta-1}}, \tag{B-49}$$

$$\ell_2:\ k_2=\frac{1}{\mathrm{g}^2}\Longrightarrow|\mathrm{g}|=2J\sqrt{\frac{(-1)^{\Theta[d]}(1-\delta^2)}{\delta-(2d+1)}}, \tag{B-50}$$

which recover Eq. (3-11) in Chapter 3. The number of bound states changes in pairs on either side of these two phase boundaries. Additionally, when $d\leq-1\wedge\delta>0$ or $d\geq0\wedge\delta<0$ are satisfied, the number of bound states also changes on either side of the topological phase boundary ($\delta=0$) due to $G_{\pm}(E)|_{E=0}=0$, but these changes do not occur in pairs, as shown in Figs. B.5(b) and B.5(d).

Finally, let us return to the long-time behavior of the maximum stored energy, *i.e.* $\mathcal{E}(\infty)=\omega_e\left|c_{\mathrm{B}}(\infty)\right|^2$. After analyzing the situation of changes in the number of bound states, according to Eq. (B-29), we also need to calculate the residues corresponding to these bound states, *i.e.* $\mathrm{Res}[\mathscr{C}(z),E_i]$. When $d\leq-1\wedge\delta>0$ or $d\geq0\wedge\delta<0$, based on the above discussion, we know that the number of bound states is odd. Among these, there must be a zero-energy bound state (corresponding to a second-order pole), and the remaining BSEs are non-zero and occur in pairs with opposite signs (corresponding to a first-order pole). Meanwhile, the residue of the zero-energy bound state equals zero due to $G(x_{1,B},x_{2,A};E_i=0)=0$, whereas the residues of the other bound states are non-zero due to $G(x_{1,B},x_{2,A};E_i\neq0)\neq0$; specifically,

$$\mathrm{Res}[\mathscr{C}(z),E_i=0]=0,\quad \mathrm{Res}[\mathscr{C}(z),E_i\neq0]=-\mathrm{Res}[\mathscr{C}(z),-E_i\neq0]\neq0. \tag{B-51}$$

The last term in Eq. (B-51) also holds when the above condition ($d\leq-1\wedge\delta>0$ or $d\geq0\wedge\delta<0$) is not satisfied. As a consequence, the maximum stored energy in the long-time limit is computed as

$$\begin{aligned}\frac{\max_t[\mathcal{E}(\infty)]}{\omega_e}&=\max_t\left|\sum_{E_k\in\mathrm{BSEs}}\mathrm{Res}[\mathscr{C}(z),E_k]e^{-iE_kt}\right|^2\\&=\max_t\left|\sum_{E_i>0}2\,\mathrm{Res}[\mathscr{C}(z),E_i]\sin(E_it)\right|^2,\end{aligned} \tag{B-52}$$

which can reach values arbitrarily close to $4\{\sum_i|\mathrm{Res}[\mathscr{C}(z),E_i]|\}^2$, where $E_i>0$. Because

these self-energies and their derivatives are continuous across different bandgaps (*i.e.* $\mathcal{R}_l$, $\mathcal{R}_m$, and $\mathcal{R}_r$), the residues corresponding to the bound-state energies distributed in these bandgaps should also be continuous.

Furthermore, since $\mathrm{d}G_{\pm}/\mathrm{d}z$ diverges at the band-gap edges, $\mathrm{Res}[\mathscr{C}(z), E_i]$ approaches zero when the bound-state energy E_i is close to the band-gap edges. Therefore, integrating the above discussions and Eq. (B-51), we conclude that the derivative of the maximum stored energy (itself is always continuous), $\max[\mathcal{E}(\infty)]$, remains continuous across the topological phase boundary, while it becomes discontinuous across the phase boundaries ℓ_1 and ℓ_2. This corresponds to the results shown in the inset of Fig. 3.2(c) in Chapter 3.

B.4.2 Dissipation immunity of quantum battery

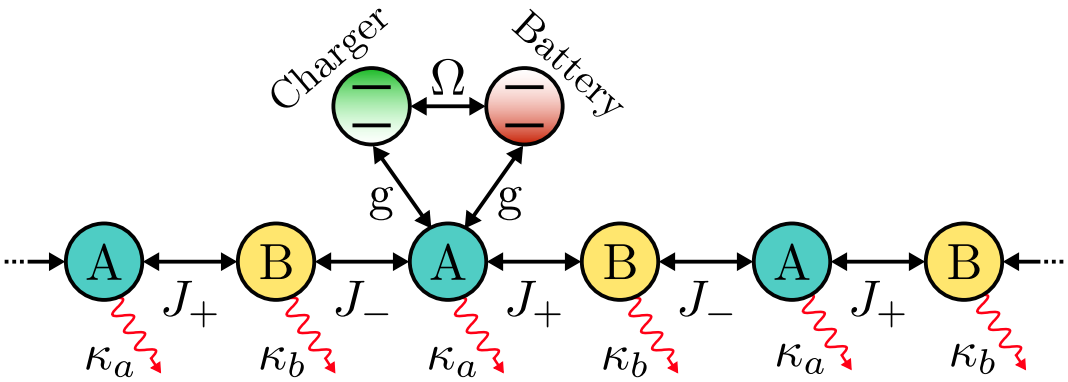

Figure B.6: Configuration-II: The quantum charger and the quantum battery are located in the same sublattices at the same positions, *i.e.*$\alpha = \beta = A$ and $x_1 = x_2$, which means that the direct coupling interaction appears (*i.e.* $\Omega_{12}^{\alpha\beta} = \Omega \neq 0$). Here, κ_a and κ_b are the decay rate of the sublattice A and B, respectively, and we assume that there is only single-sublattice dissipation, *i.e.* $\kappa_a = \kappa \neq 0$ and $\kappa_b = 0$.

For the configuration considered in Sec. B.4.1, as shown in Fig. B.4, regardless of the distance between the quantum charger and quantum battery, at the appropriate parameters, the quantum charger can always transfer almost all of its energy to the quantum battery through the topological environment, *i.e.* $\max_t[\mathcal{E}(\infty)]/\omega_e \approx 1$. However, once there is photon loss in the Su-Schrieffer-Heeger photonic lattice, all the coherent bound states (*i.e.* $\mathrm{Im}[E_i] = 0$) will transform into dissipative bound states (*i.e.* $\mathrm{Im}[E_i] < 0$), and consequently, all the energy

in the quantum charger and the quantum battery will be lost in the long-time limit, which implies $\max_t[\mathcal{E}(\infty)]/\omega_e = 0$. In fact, there exists another configuration with a dark state, different from configuration-I, whose energy transfer from the quantum charger to the quantum battery remains unaffected by the environmental dissipation, as shown in Fig. B.6. For the configuration II, the corresponding pole equation is given by

$$\begin{aligned}\mathscr{D}(E_i) &= [E_i - \Delta - \Sigma_{11}^{AA}(E_i)]^2 - [\Omega + \Sigma_{11}^{AA}(E_i)]^2 \\ &= [E_i - \Delta - \Omega - 2 \times \Sigma_{11}^{AA}(E_i)][E_i - \Delta + \Omega] = 0\end{aligned} \tag{B-53}$$

with the single-emitter self-energy

$$\Sigma_{11}^{AA}(z) = \mathrm{g}^2 G(x_{1,A}, x_{1,A}; z) = -\frac{z\mathrm{g}^2 \sum_{p=\pm} p\Theta[p(1-|\tilde{y}_+|)}{\sqrt{z_{\text{nh}}^4 - 4J^2 z_{\text{nh}}^2(1+\delta^2) + 16J^4\delta^2}}, \tag{B-54}$$

where $z_{\text{nh}} = \sqrt{z(z+i\kappa/2)}$. According to the pole equation, it is evident that this dissipative system can have at most two coherent bound states. One is an environment-independent bound state, also known as the dark state, with energy $E_{\text{dark}} = \Delta - \Omega$. The other, known as the vacancy-like dressed bound state, appears only when $\Delta + \Omega = 0$, and has the energy $E_{\text{vbs}} = 0$. Subsequently, when $\Delta = -\Omega \neq 0$, the residues of these bound states are computed as

$$\text{Res}[\mathscr{C}(z), E_{\text{dark}}] = \left.\frac{\Omega + \Sigma_{11}^{AA}(z)}{\mathrm{d}\mathscr{D}(z)/\mathrm{d}z}\right|_{z=E_{\text{dark}}} = -\frac{1}{2}, \tag{B-55}$$

$$\text{Res}[\mathscr{C}(z), E_{\text{vbs}}] = \left.\frac{\Omega + \Sigma_{11}^{AA}(z)}{\mathrm{d}\mathscr{D}(z)/\mathrm{d}z}\right|_{z=E_{\text{vbs}}} = \frac{J^2|\delta|}{\mathrm{g}^2 + 2J^2|\delta|}. \tag{B-56}$$

Besides, the dark state $|\psi_{\text{dark}}\rangle$ and the vacancy-like dressed bound state $|\psi_{\text{vbs}}\rangle$ can be obtained by solving the secular equation $H_{\text{eff}}|\psi\rangle = E|\psi\rangle$. Consequently, these bound states are derived as

$$|\psi_{\text{dark}}\rangle = \frac{1}{\sqrt{2}}(\sigma_+^{\text{C}} - \sigma_+^{\text{B}})|g, g; \text{vac}\rangle\,, \tag{B-57}$$

$$|\psi_{\text{vbs}}\rangle = \sqrt{\frac{2J^2|\delta|}{\mathrm{g}^2 + 2J^2|\delta|}}\left[\frac{1}{\sqrt{2}}(\sigma_+^{\text{C}} + \sigma_+^{\text{B}}) + \sum_j (c_{j,a}a_j^\dagger + c_{j,b}b_j^\dagger)\right]|g, g; \text{vac}\rangle\,, \tag{B-58}$$

where

$$c_{j,a}=0,\quad c_{j,b}=-\frac{\sqrt{2}\mathrm{g}}{J(1+\delta)}\left(\frac{\delta-1}{\delta+1}\right)^{x_j-x_1}\mathrm{sign}(\delta)\times\Theta[\delta(x_j-x_1+0^+)]. \tag{B-59}$$

Finally, combining Eqs. (B-29), (B-55), and (B-56), the probability amplitude for the quantum battery to be in the excited state in the long-time limit is given by

$$c_{\mathrm{B}}(\infty)=\frac{J^2\left|\delta\right|}{\mathrm{g}^2+2J^2\left|\delta\right|}-\frac{1}{2}e^{2iGt}. \tag{B-60}$$

This formula shows beyond doubt that even in the dissipative environment, the energy in the quantum charger can always be transferred to the quantum battery, particularly in the case of weak coupling, *i.e.* $\mathrm{g}\ll J$, and nearly all the energy can be transferred to the quantum battery. The two bound states play a crucial role in the energy transfer process. Additionally, according to Eq. (3-10) in Chapter 3, the maximum ergotropy is computed as

$$\begin{aligned}\max_t[\mathcal{W}(\infty)]/\omega_e&=\max_t[2\left|c_{\mathrm{B}}(\infty)\right|^2-1]\Theta[\left|c_{\mathrm{B}}(\infty)\right|^2-1/2]\\&=\frac{8J^4\delta^2-\mathrm{g}^4}{2(2J^2\left|\delta\right|+\mathrm{g}^2)^2}\Theta\left(2^{\frac{3}{4}}J\sqrt{|\delta|}-|\mathrm{g}|\right).\end{aligned} \tag{B-61}$$

We note that both of these bound states are essential; without either one, the maximum of the extractable energy would be zero in the long-time limit, *i.e.* $\max_t[\mathcal{W}(\infty)]=0$.

B.4.3 Effects of Disorder

In practical physical systems, disorder is inevitable and has profound effects on the performance of quantum batteries. In this section, we will discuss in detail the manifestation of disorder in the one-dimensional Su-Schrieffer-Heeger model and its impact on vacancy-like dressed bound state and the performance of quantum batteries, particularly focusing on ergotropy.

Here, we primarily investigate the impact of two types of disorder: one that affects the free frequencies of cavities (diagonal), and the other that affects the tunneling amplitudes between them (off-diagonal). The former corresponds to adding random diagonal terms to the Hamiltonian of the bath, modifying it as $H_{\text{bath}}\to H_{\text{bath}}+\sum_j(\epsilon_{a,j}a_j^\dagger a_j+\epsilon_{b,j}b_j^\dagger b_j)$, thereby breaking the

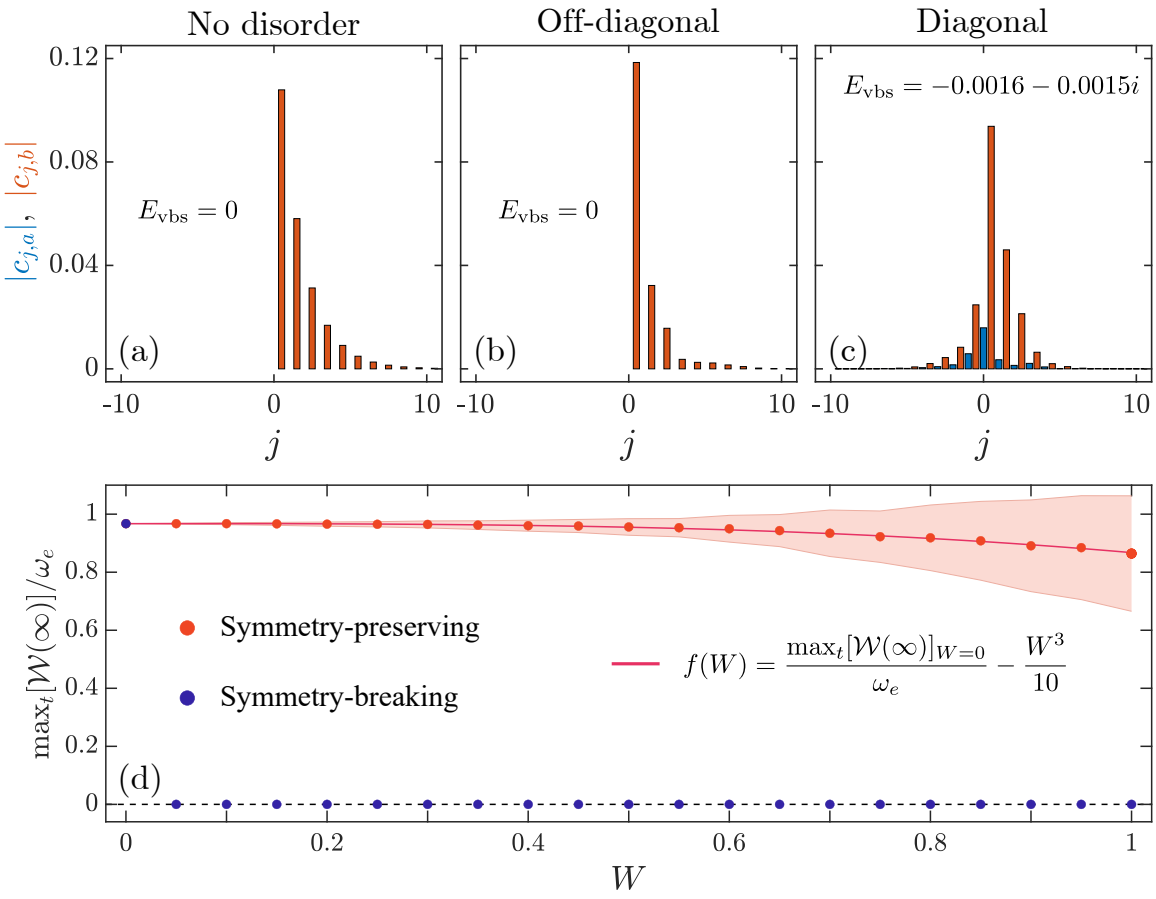

Figure B.7: Panels (a-c) describe the properties of the vacancy-like dressed bound state with and without disorder. The absolute value of probability amplitudes $|c_{j,a}|$ are shown in blue, while the $|c_{j,b}|$ are shown in orange. Panel (a) corresponds to the model without disorder, panel (b) corresponds to the model with disorder in the couplings between cavities, and panel (c) corresponds to the model with disorder in the resonant frequencies of cavities. The disorder strength is set to $W = 0.5$ in both cases with the disorder. For each case, the value of the energy of the vacancy-like dressed bound state is shown at the inside of the plots, e.g., $E_{\rm vbs} = 0$. Panel (d) shows the maximum ergotropy $\max_t[\mathcal{W}(\infty)]$ of quantum battery for the two different models of disorder as a function of the disorder strength W. The red (blue) dots correspond to the average value computed with a total of 10^3 instances of disorder for the symmetry-preserving (symmetry-breaking) case, and the shadow areas span their corresponding standard deviation. The pink line represents a fit. In all plots, the system parameters are chosen to be $\delta = 0.3$, g $= 0.1J$, $\Delta = -\Omega = 0.2J$, $\kappa_a = 10J$, $\kappa_b = 0$, and $x_1 = x_2 = 0$.

chiral symmetry of the original model. The latter corresponds to the addition of off-diagonal random terms, modifying the Hamiltonian as $H_{\text{bath}} \to H_{\text{bath}} + \sum_j (\epsilon_{1,j} a_j^\dagger b_j + \epsilon_{2,j} b_j^\dagger a_{j+1} + \text{H.c.})$, which preserves the chiral symmetry. We take the disorder parameters $\epsilon_{\nu,j}/J$ $(\nu = a, b, 1, 2)$ from a uniform distribution within the range $[-W, W]$ for each jth unit cell, where W represents the disorder strength. Additionally, we only focus on the configuration-II (see Fig. B.6) and the maximum ergotropy. Therefore, as concluded in B.4.2, we know that even in the presence of sublattice dissipation, the energy in the quantum charger can be almost completely transferred to quantum battery through the dissipative topological environment, primarily due to the contributions from the dark state and vacancy-like dressed bound state, i.e., Eqs. (B-57)-(B-58). We can be confident that the dark state is unaffected by any disorder due to the unique properties of the dark state, which decouple from the environment. Therefore, in the presence of disorder, the changes in the vacancy-like dressed bound state are the only factor influencing the performance of the quantum battery.

In the first row of Fig. B.7, we plot the shape of the three vacancy-like dressed bound states for a situation without disorder and with off-diagonal (diagonal) disorder. Note that for the situation with a diagonal disorder, although there is no vacancy-like dressed bound state, we still refer to it as such for convenience. For the symmetry-preserving case (i.e., no disorder or off-diagonal disorder), as shown in Figs. B.7(a) and B.7(b), we observe that the dressed bound state exhibits a unidirectional spatial profile and has components only on sublattice B. Additionally, compared to the clean system, in the case with off-diagonal disorder, the dressed bound state energy remains zero, indicating that chiral symmetry ensures the presence of the dressed bound state, with slight changes in the absolute magnitude of the component of the bound state on sublattice B. In contrast, for the symmetry-breaking case (i.e., diagonal disorder), as shown in Fig. B.7(c), we find that the state loses its unidirectional property and has a non-zero component on each sublattice. Furthermore, its energy also becomes a complex number with a non-zero imaginary part, i.e., $E_{\text{vbs}} = -0.0016 - 0.0015i$, indicating that breaking chiral symmetry disrupts the presence of the dressed bound state. Consequently, for our system, we can conclude that as long as chiral symmetry is preserved, even in the presence of disorder, the maximum ergotropy can remain high due to the contributions of the dark state and the vacancy-like dressed bound state. Conversely, when chiral symmetry is broken, resulting in the disappearance of the vacancy-like dressed bound state, the maximum ergotropy drops

to zero. In fact, the data of these orange and blue dots in Fig. B.7(c) corroborates this conclusion. More importantly, as shown by the orange dots in Fig. B.7(c), we find that the maximum ergotropy is strongly robust to off-diagonal disorder. As disorder strength W increases, its average value obeys a power-law distribution, i.e., $f(W) = \max_t[\mathcal{W}(\infty)]_{W=0}/\omega_e - W^3/10$, where $\max_t[\mathcal{W}(\infty)]_{W=0}/\omega_e$ is given by Eq. (B-61), as indicated by the pink line in Fig. B.7(c). Even under strong off-diagonal disorder, such as $W = 1$, the average value of maximum ergotropy can still exceed 4/5. However, as shown by the blue dots in Fig. B.7(c), the maximum ergotropy is always zero for the symmetry-breaking case.

B.4.4 The impact of environmental dissipation on quantum battery performance: Quantum Zeno effect

Before proceeding, we turn to the pole equation (B-53) and take $\Delta = -\Omega$. The pole equation can be further simplified as

$$\mathscr{D}(E_i) = E_i(E_i + 2\Omega)\left[1 + \frac{\mathrm{g}^2\sum_{p=\pm} p\Theta[p(1-|\tilde{y}_+|)]}{\sqrt{z_{\mathrm{nh}}^4 + 4J^2 z_{\mathrm{nh}}^2(1+\delta^2) + 16J^4\delta^2}}\right]_{z=E_i} = 0. \tag{B-62}$$

Apart from the two coherent bound states mentioned in Sec. B.4.2, according to the pole equation, we can also find two dissipative bound states and the corresponding energies can be obtained by solving

$$z_{\mathrm{nh}}|_{z=E_i} = \pm\sqrt{2J^2(1+\delta^2) + 2\sqrt{\mathrm{g}^4 + J^4(1-\delta)^2}} \equiv E_{0,\pm}, \tag{B-63}$$

where $E_{0,\pm}$ are the bound-state energies in the non-dissipative environment, which satisfy $\mathscr{D}(E_{0,\pm})|_{\kappa=0} = 0$. The solution in Eq. (B-63) is given by

$$E_{\kappa,\pm} = -\frac{i}{4}\kappa \pm \sqrt{E_{0,\pm}^2 - (\kappa/4)^2}, \tag{B-64}$$

which represent the dissipative bound-state energies in the dissipative environment. Subsequently, let us analyze the dissipative bound-state contributions in a short time when $\kappa/J \gg 1$.

First, following Eqs. (B-55) and (B-56), the corresponding residues are computed as

$$\begin{aligned}\mathrm{Res}[\mathscr{D}(z), E_{\kappa,\pm}] &= \left.\frac{\Omega + \Sigma_{11}^{AA}(z)}{\mathrm{d}\mathscr{D}(z)/\mathrm{d}z}\right|_{z=E_{\kappa,\pm}} \\ &= \frac{\mathrm{g}^4}{E_{\kappa,\pm}(E_{\kappa,\pm} + i\kappa/4)[E_{0,\pm}^2 - 2J^2(1+\delta^2)]}. \end{aligned} \tag{B-65}$$

Second, when $\kappa/J \gg 1$, we have

$$\begin{aligned}E_{\kappa,\pm} &= -\frac{i\kappa}{4}\left[1 \pm \sqrt{1 - (4E_{0,\pm}/\kappa)^2}\right] \\ &= -\frac{i\kappa}{4}\left\{1 \pm \left[1 - 8(E_{0,\pm}/\kappa)^2 + o(\kappa^{-2})\right]\right\} \approx -(1 \pm 1)\frac{i\kappa}{4} \pm \frac{2iE_{0,\pm}^2}{\kappa}, \end{aligned} \tag{B-66}$$

and the corresponding residues are given by

$$\begin{aligned}\mathrm{Res}[\mathscr{D}(z), E_{\kappa,+}] &\approx \frac{\mathrm{g}^4}{[E_{0,+}^2 - 2J^2(1+\delta^2)](-i\kappa/2)(-i\kappa/2 + i\kappa/4)} \\ &= \frac{-8\mathrm{g}^4}{[E_{0,+}^2 - 2J^2(1+\delta^2)]\kappa^2}, \end{aligned} \tag{B-67}$$

$$\begin{aligned}\mathrm{Res}[\mathscr{D}(z), E_{\kappa,-}] &\approx \frac{\mathrm{g}^4}{[E_{0,+}^2 - 2J^2(1+\delta^2)](-2iE_{0,-}^2/\kappa)(-2iE_{0,-}^2/\kappa + i\kappa/4)} \\ &\approx \frac{2\mathrm{g}^4}{[E_{0,-}^2 - 2J^2(1+\delta^2)]E_{0,-}^2}. \end{aligned} \tag{B-68}$$

Consequently, the contribution of the dissipative bound states can be written as

$$\begin{aligned}c_{\mathrm{B}}^{\mathrm{DBS}}(t) &= \sum_{p=\pm} \mathrm{Res}[\mathscr{D}(z), E_{\kappa,p}] e^{-iE_{\kappa,p}t} \\ &\approx \frac{-8\mathrm{g}^4 \exp[-\kappa t/2]}{[E_{0,+}^2 - 2J^2(1+\delta^2)]\kappa^2} + \frac{2\mathrm{g}^4 \exp\left[-2E_{0,-}^2 t/\kappa\right]}{[E_{0,+}^2 - 2J^2(1+\delta^2)]E_{0,-}^2}. \end{aligned} \tag{B-69}$$

Finally, when $t \ll \kappa$, the first term on the right-hand side of Eq. (B-69) can be ignored, and $\exp\left[-2E_{0,-}^2 t/\kappa\right] \approx 1$ within the last term. Thus, according to Eq. (B-65), we have

$$c_{\mathrm{B}}^{\mathrm{DBS}}(t) \approx \frac{2\mathrm{g}^4}{[E_{0,+}^2 - 2J^2(1+\delta^2)]E_{0,-}^2} = c_{\mathrm{B}}^{\mathrm{CBS}}(t_n), \tag{B-70}$$

where $t_n = 2n\pi/E_{0,+}$ while $c_{\mathrm{B}}^{\mathrm{BS}}(t)$ represents the contribution of the coherent bound states with energies $E_{0,\pm}$ in the non-dissipative environment.

In conclusion, as the dissipation κ increases, we find that the stroboscopic dynamics of the dissipative system revert to those of the non-dissipative system, thereby achieving immunity to the effects of dissipation in a short time. Note that the contributions from the branch cuts are generally small and, therefore, have not been discussed here.

Chapter 4

Summary and outlook

In this thesis, I studied suppressing decoherence in open quantum systems. I focused on utilizing resonance and topological effects to counteract dissipation and quantum noise. My major contributions included preserving optomechanical entanglement through non-resonance filtering and improving quantum battery performance via topological waveguides. Let us start with a summary.

In Chapter 2, we have demonstrated that resonance effects between a mechanical mode and its thermal environment can protect optomechanical entanglement. Specifically, these resonance effects have nearly doubled the robustness of optomechanical entanglement against mechanical dissipation and environmental temperature. This protection mechanism has involved eliminating degrees of freedom associated with significant detuning between the mechanical mode and its thermal reservoirs, effectively countering decoherence. Our approach has proven particularly effective under conditions of both near-resonance and weak coupling between the mechanical mode and its environment. We have also proposed a feasible experimental implementation of the filtering model to observe these phenomena. Furthermore, we have extended this theory to an optical cavity array with one oscillating end mirror and investigated optimal optomechanical entanglement transfer. Our study has presented a significant advancement in applying resonance effects to protect quantum systems against decoherence, opening up new possibilities for large-scale quantum information processing and the construction of quantum networks.

In Chapter 3, we have developed a general framework for analyzing the atomic dynamics of a battery-charger system composed of two atoms coupled to a general bath. Specifically, in the single-excitation sector, we considered a typical one-dimensional lattice with topological properties as an environment, known as the Su-Schrieffer-Heeger model. In the long-time limit, we demonstrated that only the contributions from coherent bound state excitations are retained. We pointed out that in a topologically trivial phase, the zero-energy bound states exhibit twofold degeneracy at resonance, resulting in the maximum stored energy approaching zero. In contrast, in a topologically nontrivial phase, the maximum stored energy approaches one, indicating that the quantum charger almost completely transfers energy to the quantum battery. Moreover, we discovered that the maximum stored energy exhibits singular behavior at the phase boundary. We also observed significant differences in phase diagrams for different unit cell distances between the quantum charger and the quantum battery. Additionally, we discussed the performance of quantum batteries under different configurations. We found that when two directly coupled atoms are placed within the same cavity, the ergotropy is protected from the direct impact of sublattice dissipation due to the presence of a dark state and a vacancy-like dressed bound state. This configuration overcomes the environment-induced decoherence that causes energy loss and aging in quantum batteries. Intriguingly, we demonstrated that with the increase in dissipation, the emergence of the quantum Zeno effect significantly enhances the short-time performance of the quantum battery.

In short, I outlook for the work in Chapters 2 and Chapter 3 is as follows.

In fact, the theory of resonance-dominated entanglement, discussed in Chapter 2, applies to all interactions between light and matter [234, 235]. For instance, in the Quantum Rabi Model [236–240], which describes the interaction between the two-level atoms (qubit) and an electromagnetic field, I can similarly use non-resonant filtering to improve the robustness of concurrence [31, 38, 241, 242] (an entanglement measure for two qubits) against quantum noise and dissipation. Measuring and protecting the entanglement between qubits is crucial in quantum information and quantum computing. Observing the robustness of concurrence in the quantum Rabi model after non-resonant filtering against quantum noise and dissipation is also highly significant. The experimental setup for measuring concurrence can be found in Refs [243–245].

To extend the results in Chapter 3, I will consider the coherence charging of atomic ensembles to develop topological quantum batteries for practical applications effectively. First, we extend the conclusions from the single-excitation case to the double-excitation case, where the battery performance metric can also be elegantly solved analytically using the resolvent method [246]. Second, we can perform numerical simulations using the matrix product states [232] or hierarchical equations of motion analog [233] for the multi-excitation case.

Overall, controlling and suppressing decoherence in open quantum systems is fundamental to unlocking the potential of quantum technologies. While exploring the theoretical mechanisms of decoherence suppression may have a limited immediate impact on society and industry, the long-term implications are significant. Continued research and development in this area will pave the way for more reliable and efficient quantum devices, bringing us closer to realizing the transformative benefits of quantum computing, communication, sensing, *etc* [247].

Bibliography

[1] Heinz-Peter Breuer and Francesco Petruccione. *The theory of open quantum systems*. OUP Oxford, 2002.

[2] T. Baumgratz, M. Cramer, and M. B. Plenio. Quantifying coherence. *Phys. Rev. Lett.*, 113:140401, Sep 2014.

[3] Alexander Streltsov, Gerardo Adesso, and Martin B. Plenio. Colloquium: Quantum coherence as a resource. *Rev. Mod. Phys.*, 89:041003, Oct 2017.

[4] Wojciech Hubert Zurek. Decoherence, einselection, and the quantum origins of the classical. *Rev. Mod. Phys.*, 75:715–775, May 2003.

[5] Angel Rivas and Susana F Huelga. *Open quantum systems*, volume 10. Springer, 2012.

[6] Vittorio Gorini, Andrzej Kossakowski, and Ennackal Chandy George Sudarshan. Completely positive dynamical semigroups of n-level systems. *Journal of Mathematical Physics*, 17(5):821–825, 1976.

[7] Goran Lindblad. On the generators of quantum dynamical semigroups. *Communications in mathematical physics*, 48:119–130, 1976.

[8] Crispin W Gardiner and Peter Zoller. Quantum noise, vol. 56 of springer series in synergetics. *Springer–Verlag, Berlin*, 97:98, 2000.

[9] Paul Langevin et al. Sur la théorie du mouvement brownien. *CR Acad. Sci. Paris*, 146(530-533):530, 1908.

[10] Werner Heisenberg. Über den anschaulichen inhalt der quantentheoretischen kinematik und mechanik. *Zeitschrift für Physik*, 43(3):172–198, 1927.

[11] Roy J Glauber. Coherent and incoherent states of the radiation field. *Physical Review*, 131(6):2766, 1963.

[12] Howard J Carmichael. *Statistical methods in quantum optics 1: master equations and Fokker-Planck equations*. Springer Science & Business Media, 2013.

[13] Ulrich Weiss. *Quantum dissipative systems*. World Scientific, 2012.

[14] Richard Phillips Feynman and Frank L Vernon Jr. The theory of a general quantum system interacting with a linear dissipative system. *Annals of physics*, 281(1-2):547–607, 2000.

[15] MD LaHaye, Olivier Buu, Benedetta Camarota, and KC Schwab. Approaching the quantum limit of a nanomechanical resonator. *Science*, 304(5667):74–77, 2004.

[16] Miles Blencowe. Nanomechanical quantum limits. *Science*, 304(5667):56–57, 2004.

[17] Marlan O Scully and M Suhail Zubairy. *Quantum optics*. Cambridge university press, 1997.

[18] G. M Moy, J. J Hope, and C. M Savage. Born and markov approximations for atom lasers. *Physical Review A*, 59(1):667, 1999.

[19] Edward Brian Davies. Quantum theory of open systems. *Academic Press*, 1976.

[20] Takahiro Sagawa and Masahito Ueda. Quantum measurement and quantum control. *Science Publishing*, 2018.

[21] Ivar Fredholm. Sur une classe d'équations fonctionnelles. *Acta Mathematica*, 27:365–390, 1903.

[22] Dariusz Chruściński and Andrzej Kossakowski. Feshbach projection formalism for open quantum systems. *Phys. Rev. Lett.*, 111:050402, Jul 2013.

[23] E Schr et al. Die gegenw rtige situation in der quantenmechanik. *Die Naturwissenschaften*, 23(48):807–812, 1935.

[24] John S Bell. On the einstein podolsky rosen paradox. *Physics Physique Fizika*, 1(3):195, 1964.

[25] Dirk Bouwmeester and Anton Zeilinger. The physics of quantum information: basic concepts. In *The physics of quantum information: quantum cryptography, quantum teleportation, quantum computation*, pages 1–14. Springer, 2000.

[26] Frank J Duarte and Travis S Taylor. *Quantum Entanglement Engineering and Applications*. IOP Publishing, 2021.

[27] Alexander Streltsov, Gerardo Adesso, and Martin B Plenio. Colloquium: Quantum coherence as a resource. *Reviews of Modern Physics*, 89(4):041003, 2017.

[28] Shuntaro Takeda, Maria Fuwa, Peter van Loock, and Akira Furusawa. Entanglement swapping between discrete and continuous variables. *Physical review letters*, 114(10):100501, 2015.

[29] Genta Masada, Kazunori Miyata, Alberto Politi, Toshikazu Hashimoto, Jeremy L O'brien, and Akira Furusawa. Continuous-variable entanglement on a chip. *Nature Photonics*, 9(5):316–319, 2015.

[30] J.-M. Raimond D. Estève and J. Dalibard. *Quantum Entanglement and Information Processing*. Elsevier Amsterdam, 2003.

[31] William K Wootters. Entanglement of formation of an arbitrary state of two qubits. *Physical Review Letters*, 80(10):2245, 1998.

[32] Adam Miranowicz and Andrzej Grudka. Ordering two-qubit states with concurrence and negativity. *Physical Review A*, 70(3):032326, 2004.

[33] Ingemar Bengtsson and Karol Życzkowski. *Geometry of quantum states: an introduction to quantum entanglement*. Cambridge university press, 2017.

[34] Vlatko Vedral. Quantifying entanglement in macroscopic systems. *Nature*, 453(7198):1004–1007, 2008.

[35] Lu-Ming Duan, Géza Giedke, Juan Ignacio Cirac, and Peter Zoller. Entanglement purification of gaussian continuous variable quantum states. *Physical Review Letters*, 84(17):4002, 2000.

[36] Warwick P Bowen, Raik Schnabel, Ping Koy Lam, and Timothy Cameron Ralph. Experimental investigation of criteria for continuous variable entanglement. *Physical review letters*, 90(4):043601, 2003.

[37] SP Walborn, BG Taketani, A Salles, F Toscano, and RL de Matos Filho. Entropic entanglement criteria for continuous variables. *Physical Review Letters*, 103(16):160505, 2009.

[38] Ryszard Horodecki, Paweł Horodecki, Michał Horodecki, and Karol Horodecki. Quantum entanglement. *Reviews of modern physics*, 81(2):865, 2009.

[39] Carlton M Caves. Quantum-mechanical radiation-pressure fluctuations in an interferometer. *Physical Review Letters*, 45(2):75, 1980.

[40] Markus Aspelmeyer, Tobias J Kippenberg, and Florian Marquardt. Cavity optomechanics. *Reviews of Modern Physics*, 86(4):1391, 2014.

[41] Adrian Bachtold, Joel Moser, and MI Dykman. Mesoscopic physics of nanomechanical systems. *Reviews of Modern Physics*, 94(4):045005, 2022.

[42] Markus Aspelmeyer, Pierre Meystre, and Keith Schwab. Quantum optomechanics. *Physics Today*, 65(7):29–35, 2012.

[43] Pierre Meystre. Cavity optomechanics: Nano-and micromechanical resonators interacting with light; quantum optomechanics, 2017.

[44] Samuel L Braunstein and Peter Van Loock. Quantum information with continuous variables. *Reviews of modern physics*, 77(2):513, 2005.

[45] Mihai A Macovei and Adriana Pálffy. Multiphonon quantum dynamics in cavity optomechanical systems. *Physical Review A*, 105(3):033503, 2022.

[46] David Vitali, Sylvain Gigan, Anderson Ferreira, HR Böhm, Paolo Tombesi, Ariel Guerreiro, Vlatko Vedral, Anton Zeilinger, and Markus Aspelmeyer. Optomechanical entanglement between a movable mirror and a cavity field. *Physical review letters*, 98(3):030405, 2007.

[47] Kahlil Y Dixon, Lior Cohen, Narayan Bhusal, Christopher Wipf, Jonathan P Dowling, and Thomas Corbitt. Optomechanical entanglement at room temperature: A simulation study with realistic conditions. *Physical Review A*, 102(6):063518, 2020.

[48] Martin B Plenio. Logarithmic negativity: a full entanglement monotone that is not convex. *Physical review letters*, 95(9):090503, 2005.

[49] Deng-Gao Lai, Jie-Qiao Liao, Adam Miranowicz, and Franco Nori. Noise-tolerant optomechanical entanglement via synthetic magnetism. *Physical Review Letters*, 129(6):063602, 2022.

[50] Jing-Xue Liu, Ya-Feng Jiao, Ying Li, Xun-Wei Xu, Qiong-Yi He, and Hui Jing. Phase-controlled asymmetric optomechanical entanglement against optical backscattering. *Science China Physics, Mechanics & Astronomy*, 66(3):230312, 2023.

[51] Ya-Feng Jiao, Sheng-Dian Zhang, Yan-Lei Zhang, Adam Miranowicz, Le-Man Kuang, and Hui Jing. Nonreciprocal optomechanical entanglement against backscattering losses. *Physical Review Letters*, 125(14):143605, 2020.

[52] Cheng Shang, Hong-Zhi Shen, and Xue-Xi Yi. Nonreciprocity in a strongly coupled three-mode optomechanical circulatory system. *Optics Express*, 27(18):25882–25901, 2019.

[53] Jian Huang, Deng-Gao Lai, and Jie-Qiao Liao. Thermal-noise-resistant optomechanical entanglement via general dark-mode control. *Physical Review A*, 106(6):063506, 2022.

[54] Gabriele De Chiara, Mauro Paternostro, and G Massimo Palma. Entanglement detection in hybrid optomechanical systems. *Physical Review A*, 83(5):052324, 2011.

[55] Ling Zhou, Yan Han, Jietai Jing, and Weiping Zhang. Entanglement of nanomechanical oscillators and two-mode fields induced by atomic coherence. *Physical Review A*, 83(5):052117, 2011.

[56] Cheng Shang. Coupling enhancement and symmetrization of single-photon optomechanics in open quantum systems. *arXiv preprint arXiv:2302.04897*, 2023.

[57] Mekonnen Bekele, Tewodros Yirgashewa, and Sintayehu Tesfa. Entanglement of mechanical modes in a doubly resonant optomechanical cavity of a correlated emission laser. *Physical Review A*, 107(1):012417, 2023.

[58] Mekonnen Bekele, Tewodros Yirgashewa, and Sintayehu Tesfa. Effects of a three-level laser on mechanical squeezing in a doubly resonant optomechanical cavity coupled to biased noise fluctuations. *Physical Review A*, 105(5):053502, 2022.

[59] Yu-Qing Shi, Lei Cong, and Hans-Peter Eckle. Entanglement resonance in the asymmetric quantum rabi model. *Physical Review A*, 105(6):062450, 2022.

[60] Rooholla Ghobadi, S Kumar, B Pepper, D Bouwmeester, AI Lvovsky, and C Simon. Optomechanical micro-macro entanglement. *Physical Review Letters*, 112(8):080503, 2014.

[61] Corentin Gut, Klemens Winkler, Jason Hoelscher-Obermaier, SG Hofer, R Moghadas Nia, Nathan Walk, Adrian Steffens, Jens Eisert, Witlef Wieczorek, JA Slater, et al. Stationary optomechanical entanglement between a mechanical oscillator and its measurement apparatus. *Physical Review Research*, 2(3):033244, 2020.

[62] Jonathan Kohler, Nicolas Spethmann, Sydney Schreppler, and Dan M Stamper-Kurn. Cavity-assisted measurement and coherent control of collective atomic spin oscillators. *Physical Review Letters*, 118(6):063604, 2017.

[63] HY Sun, Cheng Shang, XX Luo, YH Zhou, and HZ Shen. Optical-assisted photon blockade in a cavity system via parametric interactions. *International Journal of Theoretical Physics*, 58:3640–3650, 2019.

[64] TA Palomaki, JD Teufel, RW Simmonds, and Konrad W Lehnert. Entangling mechanical motion with microwave fields. *Science*, 342(6159):710–713, 2013.

[65] Jasper Chan, TP Mayer Alegre, Amir H Safavi-Naeini, Jeff T Hill, Alex Krause, Simon Gröblacher, Markus Aspelmeyer, and Oskar Painter. Laser cooling of a nanomechanical oscillator into its quantum ground state. *Nature*, 478(7367):89–92, 2011.

[66] Andrey A Rakhubovsky and Radim Filip. Robust entanglement with a thermal mechanical oscillator. *Physical Review A*, 91(6):062317, 2015.

[67] C. K. Law. Interaction between a moving mirror and radiation pressure: A hamiltonian formulation. *Phys. Rev. A*, 51:2537–2541, Mar 1995.

[68] Rafael Benguria and Mark Kac. Quantum langevin equation. *Physical review letters*, 46(1):1, 1981.

[69] Yu-Long Liu, Rebing Wu, Jing Zhang, Şahin Kaya Özdemir, Lan Yang, Franco Nori, and Yu-xi Liu. Controllable optical response by modifying the gain and loss of a mechanical resonator and cavity mode in an optomechanical system. *Physical Review A*, 95(1):013843, 2017.

[70] Vittorio Giovannetti and David Vitali. Phase-noise measurement in a cavity with a movable mirror undergoing quantum brownian motion. *Physical Review A*, 63(2):023812, 2001.

[71] Zhi-Guang Lu, Cheng Shang, Ying Wu, and Xin-You Lü. Analytical approach to higher-order correlation functions in u (1) symmetric systems. *Physical Review A*, 108(5):053703, 2023.

[72] Dario Antonio, Damián H Zanette, and Daniel López. Frequency stabilization in nonlinear micromechanical oscillators. *Nature communications*, 3(1):806, 2012.

[73] Ewold Verhagen, Samuel Deléglise, Stefan Weis, Albert Schliesser, and Tobias J Kippenberg. Quantum-coherent coupling of a mechanical oscillator to an optical cavity mode. *Nature*, 482(7383):63–67, 2012.

[74] Robert Alicki. Master equations for a damped nonlinear oscillator and the validity of the markovian approximation. *Physical Review A*, 40(7):4077, 1989.

[75] Neil W Ashcroft and N David Mermin. Solid state physics. *Holt, Rinehart and Winston, New York*, 1976.

[76] Nathan Rafaël Bernier, Laszlo Daniel Toth, A Koottandavida, Marie Adrienne Ioannou, Daniel Malz, Andreas Nunnenkamp, AK Feofanov, and TJ Kippenberg. Nonreciprocal reconfigurable microwave optomechanical circuit. *Nature communications*, 8(1):604, 2017.

[77] John D Teufel, Dale Li, Michael S Allman, Katarina Cicak, AJ Sirois, Jed D Whittaker, and RW Simmonds. Circuit cavity electromechanics in the strong-coupling regime. *Nature*, 471(7337):204–208, 2011.

[78] NR Bernier, LD Tóth, AK Feofanov, and TJ Kippenberg. Level attraction in a microwave optomechanical circuit. *Physical Review A*, 98(2):023841, 2018.

[79] Mankei Tsang and Carlton M Caves. Evading quantum mechanics: engineering a classical subsystem within a quantum environment. *Physical Review X*, 2(3):031016, 2012.

[80] Keye Zhang, Pierre Meystre, and Weiping Zhang. Back-action-free quantum optomechanics with negative-mass bose-einstein condensates. *Physical Review A*, 88(4):043632, 2013.

[81] Christoffer B Møller, Rodrigo A Thomas, Georgios Vasilakis, Emil Zeuthen, Yeghishe Tsaturyan, Mikhail Balabas, Kasper Jensen, Albert Schliesser, Klemens Hammerer, and Eugene S Polzik. Quantum back-action-evading measurement of motion in a negative mass reference frame. *Nature*, 547(7662):191–195, 2017.

[82] MJ Woolley and AA Clerk. Two-mode back-action-evading measurements in cavity optomechanics. *Physical Review A*, 87(6):063846, 2013.

[83] CF Ockeloen-Korppi, Erno Damskägg, J-M Pirkkalainen, AA Clerk, MJ Woolley, and MA Sillanpää. Quantum backaction evading measurement of collective mechanical modes. *Physical review letters*, 117(14):140401, 2016.

[84] Anja Metelmann and Aashish A Clerk. Nonreciprocal photon transmission and amplification via reservoir engineering. *Physical Review X*, 5(2):021025, 2015.

[85] Aashish A Clerk, Michel H Devoret, Steven M Girvin, Florian Marquardt, and Robert J Schoelkopf. Introduction to quantum noise, measurement, and amplification. *Reviews of Modern Physics*, 82(2):1155, 2010.

[86] Gerardo Adesso, Alessio Serafini, and Fabrizio Illuminati. Extremal entanglement and mixedness in continuous variable systems. *Physical Review A*, 70(2):022318, 2004.

[87] Emanuel Knill, Raymond Laflamme, and Gerald J Milburn. A scheme for efficient quantum computation with linear optics. *nature*, 409(6816):46–52, 2001.

[88] Edmund X DeJesus and Charles Kaufman. Routh-hurwitz criterion in the examination of eigenvalues of a system of nonlinear ordinary differential equations. *Physical Review A*, 35(12):5288, 1987.

[89] Guifré Vidal and Reinhard F Werner. Computable measure of entanglement. *Physical Review A*, 65(3):032314, 2002.

[90] Christian Weedbrook, Stefano Pirandola, Raúl García-Patrón, Nicolas J Cerf, Timothy C Ralph, Jeffrey H Shapiro, and Seth Lloyd. Gaussian quantum information. *Reviews of Modern Physics*, 84(2):621, 2012.

[91] Rajiah Simon. Peres-horodecki separability criterion for continuous variable systems. *Physical Review Letters*, 84(12):2726, 2000.

[92] Schwab Gigan, HR Böhm, Mauro Paternostro, Florian Blaser, G Langer, JB Hertzberg, Keith C Schwab, Dieter Bäuerle, Markus Aspelmeyer, and Anton Zeilinger. Self-cooling of a micromirror by radiation pressure. *Nature*, 444(7115):67–70, 2006.

[93] Olivier Arcizet, P-F Cohadon, Tristan Briant, Michel Pinard, and Antoine Heidmann. Radiation-pressure cooling and optomechanical instability of a micromirror. *Nature*, 444(7115):71–74, 2006.

[94] Dustin Kleckner and Dirk Bouwmeester. Sub-kelvin optical cooling of a micromechanical resonator. *Nature*, 444(7115):75–78, 2006.

[95] Dustin Kleckner, William Marshall, Michiel JA de Dood, Khodadad Nima Dinyari, Bart-Jan Pors, William TM Irvine, and Dirk Bouwmeester. High finesse opto-mechanical cavity with a movable thirty-micron-size mirror. *Physical review letters*, 96(17):173901, 2006.

[96] Wei Xiong, Da-Yu Jin, Yueyin Qiu, Chi-Hang Lam, and JQ You. Cross-kerr effect on an optomechanical system. *Physical Review A*, 93(2):023844, 2016.

[97] TA Palomaki, JW Harlow, JD Teufel, RW Simmonds, and Konrad W Lehnert. Coherent state transfer between itinerant microwave fields and a mechanical oscillator. *Nature*, 495(7440):210–214, 2013.

[98] JR Johansson, Göran Johansson, and Franco Nori. Optomechanical-like coupling between superconducting resonators. *Physical Review A*, 90(5):053833, 2014.

[99] Haixing Miao, Stefan Danilishin, and Yanbei Chen. Universal quantum entanglement between an oscillator and continuous fields. *Physical Review A*, 81(5):052307, 2010.

[100] Simon Groeblacher, A Trubarov, N Prigge, GD Cole, M Aspelmeyer, and J Eisert. Observation of non-markovian micromechanical brownian motion. *Nature communications*, 6(1):7606, 2015.

[101] Gianfranco Cariolaro and Roberto Corvaja. Implementation of two-mode gaussian states whose covariance matrix has the standard form. *Symmetry*, 14(7):1485, 2022.

[102] Julien Laurat, Gaëlle Keller, José Augusto Oliveira-Huguenin, Claude Fabre, Thomas Coudreau, Alessio Serafini, Gerardo Adesso, and Fabrizio Illuminati. Entanglement of two-mode gaussian states: characterization and experimental production and manipulation. *Journal of Optics B: Quantum and Semiclassical Optics*, 7(12):S577, 2005.

[103] Jin-Shi Xu, Chuan-Feng Li, Xiao-Ye Xu, Cheng-Hao Shi, Xu-Bo Zou, and Guang-Can Guo. Experimental characterization of entanglement dynamics in noisy channels. *Physical review letters*, 103(24):240502, 2009.

[104] Bi-Heng Liu, Li Li, Yun-Feng Huang, Chuan-Feng Li, Guang-Can Guo, Elsi-Mari Laine, Heinz-Peter Breuer, and Jyrki Piilo. Experimental control of the transition from markovian to non-markovian dynamics of open quantum systems. *Nature Physics*, 7(12):931–934, 2011.

[105] Luca Mancino, Marco Sbroscia, Ilaria Gianani, Emanuele Roccia, and Marco Barbieri. Quantum simulation of single-qubit thermometry using linear optics. *Physical Review Letters*, 118(13):130502, 2017.

[106] Jin-Shi Xu, Man-Hong Yung, Xiao-Ye Xu, Sergio Boixo, Zheng-Wei Zhou, Chuan-Feng Li, Alán Aspuru-Guzik, and Guang-Can Guo. Demon-like algorithmic quantum cooling and its realization with quantum optics. *Nature Photonics*, 8(2):113–118, 2014.

[107] Karol Bartkiewicz, Antonín Černoch, Karel Lemr, Adam Miranowicz, and Franco Nori. Experimental temporal quantum steering. *Scientific Reports*, 6(1):38076, 2016.

[108] Shao-Jie Xiong, Yu Zhang, Zhe Sun, Li Yu, Qiping Su, Xiao-Qiang Xu, Jin-Shuang Jin, Qingjun Xu, Jin-Ming Liu, Kefei Chen, et al. Experimental simulation of a quantum channel without the rotating-wave approximation: testing quantum temporal steering. *Optica*, 4(9):1065–1072, 2017.

[109] SG Mokarzel, AN Salgueiro, and MC Nemes. Modeling the reversible decoherence of mesoscopic superpositions in dissipative environments. *Physical Review A*, 65(4):044101, 2002.

[110] Kuan-Liang Liu and Hsi-Sheng Goan. Non-markovian entanglement dynamics of quantum continuous variable systems in thermal environments. *Physical Review A*, 76(2):022312, 2007.

[111] FF Fanchini, T Werlang, CA Brasil, LGE Arruda, and AO Caldeira. Non-markovian dynamics of quantum discord. *Physical Review A*, 81(5):052107, 2010.

[112] HZ Shen, Cheng Shang, YH Zhou, and XX Yi. Unconventional single-photon blockade in non-markovian systems. *Physical Review A*, 98(2):023856, 2018.

[113] Inés De Vega and Daniel Alonso. Dynamics of non-markovian open quantum systems. *Reviews of Modern Physics*, 89(1):015001, 2017.

[114] Yan-Hui Zhou, Xing-Yuan Zhang, Tong Liu, Qi-Cheng Wu, Zhi-Cheng Shi, Hong-Zhi Shen, and Chui-Ping Yang. Environmentally induced photon blockade via two-photon absorption. *Physical Review Applied*, 18(6):064009, 2022.

[115] P Djorwe, Yan Pennec, and Bahram Djafari-Rouhani. Frequency locking and controllable chaos through exceptional points in optomechanics. *Physical Review E*, 98(3):032201, 2018.

[116] Carl M Bender. Making sense of non-hermitian hamiltonians. *Reports on Progress in Physics*, 70(6):947, 2007.

[117] Xi-Wang Luo, Chuanwei Zhang, and Shengwang Du. Quantum squeezing and sensing with pseudo-anti-parity-time symmetry. *Physical Review Letters*, 128(17):173602, 2022.

[118] Gonzalo Ordonez and Naomichi Hatano. The arrow of time in open quantum systems and dynamical breaking of the resonance–anti-resonance symmetry. *Journal of Physics A: Mathematical and Theoretical*, 50(40):405304, 2017.

[119] Naomichi Hatano. What is the resonant state in open quantum systems? *Journal of Physics: Conference Series*, 2038(1):012013, 2021.

[120] Alexander L Fetter and John Dirk Walecka. *Quantum theory of many-particle systems*. Courier Corporation, 2012.

[121] Mauro Paternostro, David Vitali, Sylvain Gigan, MS Kim, Caslav Brukner, Jens Eisert, and Markus Aspelmeyer. Creating and probing multipartite macroscopic entanglement with light. *Physical Review Letters*, 99(25):250401, 2007.

[122] Robert Alicki and Mark Fannes. Entanglement boost for extractable work from ensembles of quantum batteries. *Phys. Rev. E*, 87:042123, Apr 2013.

[123] Francesco Campaioli, Felix A. Pollock, Felix C. Binder, Lucas Céleri, John Goold, Sai Vinjanampathy, and Kavan Modi. Enhancing the charging power of quantum batteries. *Phys. Rev. Lett.*, 118:150601, Apr 2017.

[124] Stella Seah, Martí Perarnau-Llobet, Géraldine Haack, Nicolas Brunner, and Stefan Nimmrichter. Quantum speed-up in collisional battery charging. *Phys. Rev. Lett.*, 127:100601, Aug 2021.

[125] Gaoyan Zhu, Yuanbo Chen, Yoshihiko Hasegawa, and Peng Xue. Charging quantum batteries via indefinite causal order: Theory and experiment. *Phys. Rev. Lett.*, 131:240401, Dec 2023.

[126] Federico Centrone, Luca Mancino, and Mauro Paternostro. Charging batteries with quantum squeezing. *Phys. Rev. A*, 108:052213, Nov 2023.

[127] Davide Rossini, Gian Marcello Andolina, Dario Rosa, Matteo Carrega, and Marco Polini. Quantum advantage in the charging process of sachdev-ye-kitaev batteries. *Phys. Rev. Lett.*, 125:236402, Dec 2020.

[128] Ju-Yeon Gyhm and Uwe R Fischer. Beneficial and detrimental entanglement for quantum battery charging. *AVS Quantum Science*, 6(1), 2023.

[129] Ju-Yeon Gyhm, Dominik Šafránek, and Dario Rosa. Quantum charging advantage cannot be extensive without global operations. *Phys. Rev. Lett.*, 128:140501, Apr 2022.

[130] Dario Rosa, Davide Rossini, Gian Marcello Andolina, Marco Polini, and Matteo Carrega. Ultra-stable charging of fast-scrambling syk quantum batteries. *Journal of High Energy Physics*, 2020(11):1–29, 2020.

[131] Carla Rodríguez, Dario Rosa, and Jan Olle. Artificial intelligence discovery of a charging protocol in a micromaser quantum battery. *Phys. Rev. A*, 108:042618, Oct 2023.

[132] Francesco Mazzoncini, Vasco Cavina, Gian Marcello Andolina, Paolo Andrea Erdman, and Vittorio Giovannetti. Optimal control methods for quantum batteries. *Phys. Rev. A*, 107:032218, Mar 2023.

[133] Tanoy Kanti Konar, Leela Ganesh Chandra Lakkaraju, and Aditi Sen (De). Quantum battery with non-hermitian charging. *Phys. Rev. A*, 109:042207, Apr 2024.

[134] Yu-Yu Zhang, Tian-Ran Yang, Libin Fu, and Xiaoguang Wang. Powerful harmonic charging in a quantum battery. *Phys. Rev. E*, 99:052106, May 2019.

[135] Xue Yang, Yan-Han Yang, Mir Alimuddin, Raffaele Salvia, Shao-Ming Fei, Li-Ming Zhao, Stefan Nimmrichter, and Ming-Xing Luo. Battery capacity of energy-storing quantum systems. *Phys. Rev. Lett.*, 131:030402, Jul 2023.

[136] Sergi Julià-Farré, Tymoteusz Salamon, Arnau Riera, Manabendra N. Bera, and Maciej Lewenstein. Bounds on the capacity and power of quantum batteries. *Phys. Rev. Res.*, 2:023113, May 2020.

[137] Lei Gao, Chen Cheng, Wen-Bin He, Rubem Mondaini, Xi-Wen Guan, and Hai-Qing Lin. Scaling of energy and power in a large quantum battery-charger model. *Phys. Rev. Res.*, 4:043150, Nov 2022.

[138] Tinggui Zhang, Hong Yang, and Shao-Ming Fei. Local-projective-measurement-enhanced quantum battery capacity. *Phys. Rev. A*, 109:042424, Apr 2024.

[139] Salvatore Tirone, Raffaele Salvia, Stefano Chessa, and Vittorio Giovannetti. Quantum work capacitances: Ultimate limits for energy extraction on noisy quantum batteries. *SciPost Physics*, 17(2):041, 2024.

[140] Hai-Long Shi, Shu Ding, Qing-Kun Wan, Xiao-Hui Wang, and Wen-Li Yang. Entanglement, coherence, and extractable work in quantum batteries. *Phys. Rev. Lett.*, 129:130602, Sep 2022.

[141] Gian Marcello Andolina, Maximilian Keck, Andrea Mari, Michele Campisi, Vittorio Giovannetti, and Marco Polini. Extractable work, the role of correlations, and asymptotic freedom in quantum batteries. *Phys. Rev. Lett.*, 122:047702, Feb 2019.

[142] Gianluca Francica and Luca Dell'Anna. Optimal work extraction from quantum batteries based on the expected utility hypothesis. *Phys. Rev. E*, 109:044119, Apr 2024.

[143] Juliette Monsel, Marco Fellous-Asiani, Benjamin Huard, and Alexia Auffèves. The energetic cost of work extraction. *Phys. Rev. Lett.*, 124:130601, Mar 2020.

[144] Salvatore Tirone, Raffaele Salvia, Stefano Chessa, and Vittorio Giovannetti. Work extraction processes from noisy quantum batteries: The role of nonlocal resources. *Phys. Rev. Lett.*, 131:060402, Aug 2023.

[145] Salvatore Tirone, Raffaele Salvia, Stefano Chessa, and Vittorio Giovannetti. Quantum work extraction efficiency for noisy quantum batteries: the role of coherence. *arXiv: 2305.16803*, 2023.

[146] Dario Ferraro, Michele Campisi, Gian Marcello Andolina, Vittorio Pellegrini, and Marco Polini. High-power collective charging of a solid-state quantum battery. *Phys. Rev. Lett.*, 120:117702, Mar 2018.

[147] Davide Rossini, Gian Marcello Andolina, and Marco Polini. Many-body localized quantum batteries. *Phys. Rev. B*, 100:115142, Sep 2019.

[148] Li Peng, Wen-Bin He, Stefano Chesi, Hai-Qing Lin, and Xi-Wen Guan. Lower and upper bounds of quantum battery power in multiple central spin systems. *Phys. Rev. A*, 103:052220, May 2021.

[149] Lorenzo Fusco, Mauro Paternostro, and Gabriele De Chiara. Work extraction and energy storage in the dicke model. *Phys. Rev. E*, 94:052122, Nov 2016.

[150] S. S. Seidov and S. I. Mukhin. Quantum dicke battery supercharging in the bound-luminosity state. *Phys. Rev. A*, 109:022210, Feb 2024.

[151] Alba Crescente, Matteo Carrega, Maura Sassetti, and Dario Ferraro. Ultrafast charging in a two-photon dicke quantum battery. *Phys. Rev. B*, 102:245407, Dec 2020.

[152] Borhan Ahmadi, Paweł Mazurek, Paweł Horodecki, and Shabir Barzanjeh. Nonreciprocal quantum batteries. *Physical Review Letters*, 132(21):210402, 2024.

[153] Joonho Kim, Jeff Murugan, Jan Olle, and Dario Rosa. Operator delocalization in quantum networks. *Phys. Rev. A*, 105:L010201, Jan 2022.

[154] Vahid Shaghaghi, Varinder Singh, Giuliano Benenti, and Dario Rosa. Micromasers as quantum batteries. *Quantum Science and Technology*, 7(4):04LT01, aug 2022.

[155] Giulia Gemme, Gian Marcello Andolina, Francesco Maria Dimitri Pellegrino, Maura Sassetti, and Dario Ferraro. Off-resonant dicke quantum battery: Charging by virtual photons. *Batteries*, 9:040197, 2023.

[156] Gian Marcello Andolina, Paolo Andrea Erdman, Frank Noé, Jukka Pekola, and Marco Schirò. Dicke superradiant enhancement of the heat current in circuit qed. *arXiv: 2401.17469*, 2024.

[157] Tanoy Kanti Konar, Leela Ganesh Chandra Lakkaraju, Srijon Ghosh, and Aditi Sen(De). Quantum battery with ultracold atoms: Bosons versus fermions. *Phys. Rev. A*, 106:022618, Aug 2022.

[158] A.G. Catalano, S.M. Giampaolo, O. Morsch, V. Giovannetti, and F. Franchini. Frustrating quantum batteries. *PRX Quantum*, 5:030319, Jul 2024.

[159] Felix C Binder, Sai Vinjanampathy, Kavan Modi, and John Goold. Quantacell: powerful charging of quantum batteries. *New Journal of Physics*, 17(7):075015, 2015.

[160] Luis Pedro García-Pintos, Alioscia Hamma, and Adolfo del Campo. Fluctuations in extractable work bound the charging power of quantum batteries. *Phys. Rev. Lett.*, 125:040601, Jul 2020.

[161] F. H. Kamin, F. T. Tabesh, S. Salimi, and Alan C. Santos. Entanglement, coherence, and charging process of quantum batteries. *Phys. Rev. E*, 102:052109, Nov 2020.

[162] Lu Wang, Shu-Qian Liu, Feng-lin Wu, Hao Fan, and Si-Yuan Liu. Two-mode raman quantum battery dependent on coupling strength. *Phys. Rev. A*, 108:062402, Dec 2023.

[163] F. H. Kamin, S. Salimi, and M. B. Arjmandi. Steady-state charging of quantum batteries via dissipative ancillas. *Phys. Rev. A*, 109:022226, Feb 2024.

[164] Alan C. Santos. Quantum advantage of two-level batteries in the self-discharging process. *Phys. Rev. E*, 103:042118, Apr 2021.

[165] Colin D Bruzewicz, John Chiaverini, Robert McConnell, and Jeremy M Sage. Trapped-ion quantum computing: Progress and challenges. *Applied Physics Reviews*, 6(2), 2019.

[166] P Forn-Díaz, J José García-Ripoll, Borja Peropadre, J-L Orgiazzi, MA Yurtalan, R Belyansky, Christopher M Wilson, and A Lupascu. Ultrastrong coupling of a single artificial atom to an electromagnetic continuum in the nonperturbative regime. *Nature Physics*, 13(1):39–43, 2017.

[167] Kristian Baumann, Christine Guerlin, Ferdinand Brennecke, and Tilman Esslinger. Dicke quantum phase transition with a superfluid gas in an optical cavity. *Nature*, 464(7293):1301–1306, 2010.

[168] Michel H Devoret and Robert J Schoelkopf. Superconducting circuits for quantum information: an outlook. *Science*, 339(6124):1169–1174, 2013.

[169] Francesco Campaioli, Felix A Pollock, and Sai Vinjanampathy. Quantum batteries. *Thermodynamics in the Quantum Regime: Fundamental Aspects and New Directions*, pages 207–225, 2018.

[170] Karen Southwell. Quantum coherence. *Nature*, 453(7198):1003–1004, 2008.

[171] Obinna Abah, Gabriele De Chiara, Mauro Paternostro, and Ricardo Puebla. Harnessing nonadiabatic excitations promoted by a quantum critical point: Quantum battery and spin squeezing. *Phys. Rev. Res.*, 4:L022017, Apr 2022.

[172] Debarupa Saha, Aparajita Bhattacharyya, Kornikar Sen, and Ujjwal Sen. Harnessing energy extracted from heat engines to charge quantum batteries. *arXiv:2309.15634*, 2023.

[173] Francesco Campaioli, Stefano Gherardini, James Q. Quach, Marco Polini, and Gian Marcello Andolina. Colloquium: Quantum batteries. *Rev. Mod. Phys.*, 96:031001, Jul 2024.

[174] Armen E Allahverdyan, Roger Balian, and Th M Nieuwenhuizen. Maximal work extraction from finite quantum systems. *Europhysics Letters*, 67(4):565, 2004.

[175] Wan-Lu Song, Hai-Bin Liu, Bin Zhou, Wan-Li Yang, and Jun-Hong An. Remote charging and degradation suppression for the quantum battery. *Phys. Rev. Lett.*, 132:090401, Feb 2024.

[176] Si-Yuan Bai and Jun-Hong An. Generating stable spin squeezing by squeezed-reservoir engineering. *Phys. Rev. Lett.*, 127:083602, Aug 2021.

[177] Wanlu Song, Wanli Yang, Junhong An, and Mang Feng. Dissipation-assisted spin squeezing of nitrogen-vacancy centers coupled to a rectangular hollow metallic waveguide. *Optics Express*, 25(16):19226–19235, 2017.

[178] Daniele Morrone, Matteo A.C. Rossi, and Marco G. Genoni. Daemonic ergotropy in continuously monitored open quantum batteries. *Phys. Rev. Appl.*, 20:044073, Oct 2023.

[179] Faezeh Pirmoradian and Klaus Mølmer. Aging of a quantum battery. *Phys. Rev. A*, 100:043833, Oct 2019.

[180] Shadab Zakavati, Fatemeh T. Tabesh, and Shahriar Salimi. Bounds on charging power of open quantum batteries. *Phys. Rev. E*, 104:054117, Nov 2021.

[181] Kai Xu, Han-Jie Zhu, Guo-Feng Zhang, and Wu-Ming Liu. Enhancing the performance of an open quantum battery via environment engineering. *Phys. Rev. E*, 104:064143, Dec 2021.

[182] Cheng Shang and Hongchao Li. Resonance-dominant optomechanical entanglement in open quantum systems. *Phys. Rev. Appl.*, 21:044048, Apr 2024.

[183] Matteo Carrega, Alba Crescente, Dario Ferraro, and Maura Sassetti. Dissipative dynamics of an open quantum battery. *New Journal of Physics*, 22(8):083085, 2020.

[184] Y. Yao and X. Q. Shao. Optimal charging of open spin-chain quantum batteries via homodyne-based feedback control. *Phys. Rev. E*, 106:014138, Jul 2022.

[185] Felipe Barra. Dissipative charging of a quantum battery. *Phys. Rev. Lett.*, 122:210601, May 2019.

[186] FH Kamin, FT Tabesh, S Salimi, F Kheirandish, and Alan C Santos. Non-markovian effects on charging and self-discharging process of quantum batteries. *New Journal of Physics*, 22(8):083007, 2020.

[187] Si-Yuan Bai and Jun-Hong An. Floquet engineering to reactivate a dissipative quantum battery. *Phys. Rev. A*, 102:060201, Dec 2020.

[188] Klaus von Klitzing. The quantized hall effect. *Rev. Mod. Phys.*, 58:519–531, Jul 1986.

[189] M. Z. Hasan and C. L. Kane. Colloquium: Topological insulators. *Rev. Mod. Phys.*, 82:3045–3067, Nov 2010.

[190] Ling Lu, John D Joannopoulos, and Marin Soljačić. Topological photonics. *Nature photonics*, 8(11):821–829, 2014.

[191] Tomoki Ozawa, Hannah M. Price, Alberto Amo, Nathan Goldman, Mohammad Hafezi, Ling Lu, Mikael C. Rechtsman, David Schuster, Jonathan Simon, Oded Zilberberg, and Iacopo Carusotto. Topological photonics. *Rev. Mod. Phys.*, 91:015006, Mar 2019.

[192] Philippe St-Jean, V Goblot, Elisabeth Galopin, A Lemaître, T Ozawa, Luc Le Gratiet, Isabelle Sagnes, J Bloch, and A Amo. Lasing in topological edge states of a one-dimensional lattice. *Nature Photonics*, 11(10):651–656, 2017.

[193] Yasutomo Ota, Ryota Katsumi, Katsuyuki Watanabe, Satoshi Iwamoto, and Yasuhiko Arakawa. Topological photonic crystal nanocavity laser. *Communications Physics*, 1(1):86, 2018.

[194] Brandon M. Anderson, Ruichao Ma, Clai Owens, David I. Schuster, and Jonathan Simon. Engineering topological many-body materials in microwave cavity arrays. *Phys. Rev. X*, 6:041043, Dec 2016.

[195] W. Cai, J. Han, Feng Mei, Y. Xu, Y. Ma, X. Li, H. Wang, Y. P. Song, Zheng-Yuan Xue, Zhang-qi Yin, Suotang Jia, and Luyan Sun. Observation of topological magnon insulator states in a superconducting circuit. *Phys. Rev. Lett.*, 123:080501, Aug 2019.

[196] Serge Haroche and J-M Raimond. *Exploring the quantum: atoms, cavities, and photons*. Oxford university press, 2006.

[197] Peter Lodahl, Sahand Mahmoodian, and Søren Stobbe. Interfacing single photons and single quantum dots with photonic nanostructures. *Rev. Mod. Phys.*, 87:347–400, May 2015.

[198] D. E. Chang, J. S. Douglas, A. González-Tudela, C.-L. Hung, and H. J. Kimble. Colloquium: Quantum matter built from nanoscopic lattices of atoms and photons. *Rev. Mod. Phys.*, 90:031002, Aug 2018.

[199] Sabyasachi Barik, Aziz Karasahin, Christopher Flower, Tao Cai, Hirokazu Miyake, Wade DeGottardi, Mohammad Hafezi, and Edo Waks. A topological quantum optics interface. *Science*, 359(6376):666–668, 2018.

[200] Sajeev John and Jian Wang. Quantum electrodynamics near a photonic band gap: Photon bound states and dressed atoms. *Phys. Rev. Lett.*, 64:2418–2421, May 1990.

[201] Yanbing Liu and Andrew A Houck. Quantum electrodynamics near a photonic bandgap. *Nature Physics*, 13(1):48–52, 2017.

[202] Neereja M. Sundaresan, Rex Lundgren, Guanyu Zhu, Alexey V. Gorshkov, and Andrew A. Houck. Interacting qubit-photon bound states with superconducting circuits. *Phys. Rev. X*, 9:011021, Feb 2019.

[203] Peter Lodahl, Sahand Mahmoodian, Søren Stobbe, Arno Rauschenbeutel, Philipp Schneeweiss, Jürgen Volz, Hannes Pichler, and Peter Zoller. Chiral quantum optics. *Nature*, 541(7638):473–480, 2017.

[204] Wei Nie, Tao Shi, Franco Nori, and Yu-xi Liu. Topology-enhanced nonreciprocal scattering and photon absorption in a waveguide. *Phys. Rev. Appl.*, 15:044041, Apr 2021.

[205] Miguel Bello, Gloria Platero, Juan Ignacio Cirac, and Alejandro González-Tudela. Unconventional quantum optics in topological waveguide qed. *Science advances*, 5(7):eaaw0297, 2019.

[206] C. Tabares, A. Muñoz de las Heras, L. Tagliacozzo, D. Porras, and A. González-Tudela. Variational quantum simulators based on waveguide qed. *Phys. Rev. Lett.*, 131:073602, Aug 2023.

[207] Guoqing Tian, Ying Wu, and Xin-You Lü. Power-law-exponential interaction induced quantum spiral phases. *arXiv:2405.14243*, 2024.

[208] Jens Koch, Terri M. Yu, Jay Gambetta, A. A. Houck, D. I. Schuster, J. Majer, Alexandre Blais, M. H. Devoret, S. M. Girvin, and R. J. Schoelkopf. Charge-insensitive qubit design derived from the cooper pair box. *Phys. Rev. A*, 76:042319, Oct 2007.

[209] Mohammad Mirhosseini, Eunjong Kim, Vinicius S Ferreira, Mahmoud Kalaee, Alp Sipahigil, Andrew J Keller, and Oskar Painter. Superconducting metamaterials for waveguide quantum electrodynamics. *Nature communications*, 9(1):3706, 2018.

[210] Vinicius S. Ferreira, Jash Banker, Alp Sipahigil, Matthew H. Matheny, Andrew J. Keller, Eunjong Kim, Mohammad Mirhosseini, and Oskar Painter. Collapse and revival of an artificial atom coupled to a structured photonic reservoir. *Phys. Rev. X*, 11:041043, Dec 2021.

[211] Xiu Gu, Anton Frisk Kockum, Adam Miranowicz, Yu-xi Liu, and Franco Nori. Microwave photonics with superconducting quantum circuits. *Physics Reports*, 718:1–102, 2017.

[212] Dibyendu Roy, C. M. Wilson, and Ofer Firstenberg. Colloquium: Strongly interacting photons in one-dimensional continuum. *Rev. Mod. Phys.*, 89:021001, May 2017.

[213] Eunjong Kim, Xueyue Zhang, Vinicius S. Ferreira, Jash Banker, Joseph K. Iverson, Alp Sipahigil, Miguel Bello, Alejandro González-Tudela, Mohammad Mirhosseini, and Oskar Painter. Quantum electrodynamics in a topological waveguide. *Phys. Rev. X*, 11:011015, Jan 2021.

[214] Jia-shun Yan and Jun Jing. Charging by quantum measurement. *Phys. Rev. Appl.*, 19:064069, Jun 2023.

[215] W. P. Su, J. R. Schrieffer, and A. J. Heeger. Solitons in polyacetylene. *Phys. Rev. Lett.*, 42:1698–1701, Jun 1979.

[216] W. P. Su, J. R. Schrieffer, and A. J. Heeger. Soliton excitations in polyacetylene. *Phys. Rev. B*, 22:2099–2111, Aug 1980.

[217] Zongping Gong, Miguel Bello, Daniel Malz, and Flore K. Kunst. Anomalous behaviors of quantum emitters in non-hermitian baths. *Phys. Rev. Lett.*, 129:223601, Nov 2022.

[218] Zongping Gong, Miguel Bello, Daniel Malz, and Flore K. Kunst. Bound states and photon emission in non-hermitian nanophotonics. *Phys. Rev. A*, 106:053517, Nov 2022.

[219] Robert Alicki. Master equations for a damped nonlinear oscillator and the validity of the markovian approximation. *Phys. Rev. A*, 40:4077–4081, Oct 1989.

[220] A. González-Tudela and J. I. Cirac. Markovian and non-markovian dynamics of quantum emitters coupled to two-dimensional structured reservoirs. *Phys. Rev. A*, 96:043811, Oct 2017.

[221] Zongping Gong, Sho Higashikawa, and Masahito Ueda. Zeno hall effect. *Phys. Rev. Lett.*, 118:200401, May 2017.

[222] János K Asbóth, László Oroszlány, and András Pályi. A short course on topological insulators: *Band Structure and Edge States in One and Two Dimensions*. *Lecture notes in physics*, 919:166, 2016.

[223] A. González-Tudela and J. I. Cirac. Quantum emitters in two-dimensional structured reservoirs in the nonperturbative regime. *Phys. Rev. Lett.*, 119:143602, Oct 2017.

[224] Claude Cohen-Tannoudji, Jacques Dupont-Roc, and Gilbert Grynberg. *Atom-photon interactions: basic processes and applications*. John Wiley & Sons, 1998.

[225] Gerbold C Ménard, Sébastien Guissart, Christophe Brun, Stéphane Pons, Vasily S Stolyarov, François Debontridder, Matthieu V Leclerc, Etienne Janod, Laurent Cario, Dimitri Roditchev, et al. Coherent long-range magnetic bound states in a superconductor. *Nature Physics*, 11(12):1013–1016, 2015.

[226] James Q. Quach and William J. Munro. Using dark states to charge and stabilize open quantum batteries. *Phys. Rev. Appl.*, 14:024092, Aug 2020.

[227] Luca Leonforte, Angelo Carollo, and Francesco Ciccarello. Vacancy-like dressed states in topological waveguide qed. *Phys. Rev. Lett.*, 126:063601, Feb 2021.

[228] Vladislav Popkov and Carlo Presilla. Full spectrum of the liouvillian of open dissipative quantum systems in the zeno limit. *Phys. Rev. Lett.*, 126:190402, May 2021.

[229] Naomichi Hatano and David R. Nelson. Localization transitions in non-hermitian quantum mechanics. *Phys. Rev. Lett.*, 77:570–573, Jul 1996.

[230] Tao Shi, Ying Hai Wu, Alejandro González-Tudela, and J Ignacio Cirac. Effective many-body hamiltonians of qubit-photon bound states. *New Journal of Physics*, 20(10):105005, 2018.

[231] T. Shi, Shanhui Fan, and C. P. Sun. Two-photon transport in a waveguide coupled to a cavity in a two-level system. *Phys. Rev. A*, 84:063803, Dec 2011.

[232] Ulrich Schollwöck. The density-matrix renormalization group in the age of matrix product states. *Annals of physics*, 326(1):96–192, 2011.

[233] Yoshitaka Tanimura. Numerically "exact" approach to open quantum dynamics: The hierarchical equations of motion (heom). *The Journal of chemical physics*, 153(2), 2020.

[234] Rico Gutzler, Manish Garg, Christian R Ast, Klaus Kuhnke, and Klaus Kern. Light–matter interaction at atomic scales. *Nature Reviews Physics*, 3(6):441–453, 2021.

[235] Alejandro González-Tudela, Andreas Reiserer, Juan José García-Ripoll, and Francisco J García-Vidal. Light–matter interactions in quantum nanophotonic devices. *Nature Reviews Physics*, 6(3):166–179, 2024.

[236] Loïc Henriet, Zoran Ristivojevic, Peter P Orth, and Karyn Le Hur. Quantum dynamics of the driven and dissipative rabi model. *Physical Review A*, 90(2):023820, 2014.

[237] LO Castanos-Cervantes. Quantum rabi model with dissipation and qubit driving. *Physical Review A*, 104(3):033709, 2021.

[238] Lei Cong, Simone Felicetti, Jorge Casanova, L Lamata, Enrique Solano, and Iñigo Arrazola. Selective interactions in the quantum rabi model. *Physical Review A*, 101(3):032350, 2020.

[239] II Rabi. On the process of space quantization. *Physical Review*, 49(4):324, 1936.

[240] Xiang-Bin Wang, J. Q. You, and Franco Nori. Quantum entanglement via two-qubit quantum zeno dynamics. *Phys. Rev. A*, 77:062339, Jun 2008.

[241] Sam A Hill and William K Wootters. Entanglement of a pair of quantum bits. *Physical review letters*, 78(26):5022, 1997.

[242] Pranaw Rungta, V. Bužek, Carlton M. Caves, M. Hillery, and G. J. Milburn. Universal state inversion and concurrence in arbitrary dimensions. *Phys. Rev. A*, 64:042315, Sep 2001.

[243] G. Romero, C. E. López, F. Lastra, E. Solano, and J. C. Retamal. Direct measurement of concurrence for atomic two-qubit pure states. *Phys. Rev. A*, 75:032303, Mar 2007.

[244] Sang Min Lee, Se-Wan Ji, Hai-Woong Lee, and M. Suhail Zubairy. Proposal for direct measurement of concurrence via visibility in a cavity qed system. *Phys. Rev. A*, 77:040301, Apr 2008.

[245] Shi-Biao Zheng and Guang-Can Guo. Efficient scheme for two-atom entanglement and quantum information processing in cavity qed. *Phys. Rev. Lett.*, 85:2392–2395, Sep 2000.

[246] Tao Shi, Ying-Hai Wu, A. González-Tudela, and J. I. Cirac. Bound states in boson impurity models. *Phys. Rev. X*, 6:021027, May 2016.

[247] Christiane P Koch. Controlling open quantum systems: tools, achievements, and limitations. *Journal of Physics: Condensed Matter*, 28(21):213001, 2016.

Acknowledgment

What do I stand here alone for if without you? In the immense expanse of the universe, our home, earth, is but a speck of dust. Over the lengthy timeline of history, human civilization will inevitably vanish like a fleeting bird across the sky. If everything is destined to return to nothingness, what is the purpose of the universe? Since death is unavoidable, then what is the meaning of life? The former stems from our curiosity about nature, which gave birth to science, while the latter defines life through the bonds between us.

First, I would like to sincerely thank my doctoral supervisor, Prof. Naomichi Hatano, for his academic guidance, generous support, and kindness in my daily life. Over the past three years, he has continually encouraged me, sustained and inspired me, tolerated my stupidity and mistakes, meticulously taught me how to conduct academic research and present my findings, patiently corrected my English pronunciation, and provided me with selfless help. I am pleased and excited to be his Ph.D. student and have the chance to study with him. Through words and actions, he taught me how to become a pure person and focus on science itself. When I was frustrated by my own clumsiness, he reminded me that my strengths lie in deep thinking and continuous insight. It is my pride to be his student. Additionally, a free academic environment in Hatano lab nurtures my diverse interests and progressively helps me become an independent researcher. I also thank the Hatano lab for the ice cream and coffee. Next, I would like to thank my adviser at RIKEN, Dr. Tomotaka Kuwahara. As a young principal investigator, he is sincere and exceptionally creative in research. He guides me in finding my research path, focusing on the complexity of quantum dissipative dynamics from an information-theoretic perspective. He provides valuable insights, and I always enjoy talking and discussing with him. I am also grateful and delighted to have the opportunity to work with him as a Postdoctoral Researcher.

I would also like to thank all of the professors in my supervisory committee, Yuto Ashida,

Masahito Ueda, Mio Murao, Kiyotaka Aikawa, and Kuniaki Konishi, for their careful review, critical comments, and proofreading. Their help improved my work, and their positive feedback kept me motivated. They sincerely pointed out my shortcomings, prompting me to re-examine and improve myself. I am grateful to my young collaborators, Zhi-Guang Lu, Hongchao Li, Hayato Kinkawa, and Dr. Tomotaka Kuwahara who have made my research journey less lonely. I have learned a lot from their discussions. More importantly, we share research interests and strengthen each other's determination to pursue our studies. I am also grateful to my friends, Dr. Yuezhou Li, Zijian Cui, Ying Su, Chen Li, Jing Feng, Dr. Hongzhi Shen, Dr. Tan Van Vu, Naoko Seiji, Dr. Donghoon Kim, Dr. Yusuke Kimura, Prof. Xuexi Yi, Dr. Zongping Gong, Minako Hiejima, Dr. Ken-Ichiro Imura, Dr. Jaeha Lee, Dr. Takano Taira, Manami Yamagishi, Norihiro Makiguchi, Mahmoud Ali, Prof. Tota Nakamura, Dr. Ochi Masaki, Dr. Ishizaki Miku, Noriko Jinbo, Hiroki Nakabayashi, Shiwen Ma, Xing Wei, Prof. Chang-Pu Sun, Prof. Franco Nori, Zhilei Zhang, Junyan Sun, Zhuo-Cheng Gu, Liu Yang, Bo-Wang Zhang, Dr. Dapeng Yao, Özlem, Prof. Masatoshi Sato, Prof. Keiji Saito, Prof. Li Lu, Yimin Gu, Shengyu Zhang, Jinlei Li, Zhanqiu Gong, Dejian Li, Dr. Weijun Cheng, and Dr. Atsuki Yoshinaga, for all the help and chats with them when I felt overwhelming. I am grateful for your companionship and the wonderful experiences you all have brought me. I would also like to thank my cousin, Chu-Heng Zhou, for his encouragement.

Finally, and most importantly, I would like to thank my parents, Zhi-Li Shang and Li-Hong Cheng, as well as my beloved wife, Xuan Zhang, for their love and support throughout my Ph.D. They have provided me with a home—a warm and safe haven—giving me the courage to face anything. I am especially grateful to my wife for enduring the pain of separation to support my dreams. Her sunny and lively personality helps me dispel the gloom, and her unwavering love and encouragement are always at my back. In addition, I would also like to acknowledge the financial support from the China Scholarship Council and the Japanese Government (Monbukagakusho-MEXT) Scholarship under Grant No. 211501. I appreciate the support provided by the RIKEN Junior Research Associate Program. I am willing to be a devout follower of nature with a pure heart and to live a simple life. I am also grateful to myself and wish myself well. I would like to end with a quote from Dr. Sheldon Cooper in *The Big Bang Theory*: "In my way, I love you all." I am grateful for all the encounters; because of you, my soul has become complete and interesting. :)